Damage Detection Using Second Harmonic Generation of Low-Frequency Guided Waves

A Thesis by Publication Submitted in Partial Fulfilment of the Requirement of the Degree of Doctor of Philosophy (PhD)

Yi Yang

The University of Adelaide

School of Civil, Environmental and Mining Engineering

01/2019

CERTIFICATE OF ORIGINALITY

I, Yi Yang, certify that this work contains no material which has been accepted for the award of any other degree or diploma in my name, in any university or other tertiary institution and, to the best of my knowledge and belief, contains no material previously published or written by another person, except where due reference has been made in the text. In addition, I certify that no part of this work will, in the future, be used in a submission in my name, for any other degree or diploma in any university or other tertiary institution without the prior approval of the University of Adelaide and where applicable, any partner institution responsible for the joint-award of this degree.

I acknowledge that copyright of published works contained within this thesis resides with the copyright holder(s) of those works.

I also give permission for the digital version of my thesis to be made available on the web, via the University's digital research repository, the Library Search and also through web search engines, unless permission has been granted by the University to restrict access for a period of time.

I acknowledge the support I have received for my research through the provision of an Australian Government Research Training Program Scholarship.

_____

Yi Yang

ABSTRACT

The thesis provides physical insights into the nonlinear phenomena associated with propagation of guided waves (GW) in thin walled structures. The non-linear phenomena are investigated using experimental techniques, the three-dimensional (3D) finite element (FE) simulations as well as theoretical studies. The thesis is divided into two main parts. In the first part, the contact nonlinearities are studied, while the focus of the second part is on the intrinsic material nonlinearities. The thesis represent a compendium of published, submitted and prepared for submission papers united by the same topic and methodology. Each paper contains the background information and an extensive literature review. For this reason, the thesis does not have a separate chapter on literature review or background.

In the first part of the thesis, the generation of the second order harmonic of Lamb waves as a result of contact non-linearity associated with presence of fatigue cracks (paper 1 & 2), contact loosening in bolted joints (paper 3) and delamination in a composite material (paper 4) are investigated. A relative nonlinear parameter (NP) is introduced and utilised to quantify the rate of the growth of the second harmonic (SH). In the case of fatigue cracks, experimental studies along with the 3D FE simulations are conducted in order to maximise the amplitude of the SH and identify the directivity patterns of NP, influence of incident wave angles, and the external loading on the generation of the rate of SH. A feasibility study on detecting loosen bolts is carried out, and the results demonstrated that the generation of the SH can indicate the bolt loosening, however, there is a fluctuation of the results between different group of tests. Finally, a FE model of an aluminium plate with composite patch repaired weakened by defects i.e. delamination and fatigue crack, is developed. The outcomes of dynamic simulations reveal that when a proper GW mode is selected, then it is possible to not only detect the presences of defects, but also the type of the defects.

In the second part of the thesis, a VUMAT (material properties) subroutine is developed and implemented in a 3D FE model. It utilises the Murnaghans' strain energy function to study the intrinsic material nonlinearities and the effect of the applied stresses in an aluminium plate. The FE model with a weakly nonlinear material model is first validated with theoretical solutions describing the acousto-elastic effect and changes of the phase velocity with the applied stress (paper 5). The variation of the second order NP with the wave propagation distance is studied in paper 6. The developed 3D FE model provides a more convenient and flexible approach to study the acoustoelastic effects in prestressed waveguides with complex

geometry. Meanwhile, it also provides more options to select the material behaviour and investigate nonlinear phenomena generated by the propagation of nonlinear GW features in weakly-nonlinear material (paper 6).

LIST OF PUBLICATIONS FROM THIS RESEARCH

Journal Papers

1. Yang, Y., Ng, C., Kotousov, A., Sohn, H., & Lim, H. (2018). Second harmonic generation at fatigue cracks by low-frequency Lamb waves: Experimental and numerical studies. *Mechanical Systems and Signal Processing*, 99, 760-773.
2. Yang, Y., Ng, C., Kotousov, A. (2018). Influence of crack opening and incident wave angle on second harmonic generation of Lamb waves. *Smart Materials and Structures*. 27(5), 055013.
3. Yang, Y., Ng, C., Kotousov, A. (2019). Second harmonic generation of guided wave at crack-induced debonding in FRP strengthened metal plates. *International Journal of Structural Stability and Dynamics*, 19(1), 1940006.
4. Yang, Y., Ng, C., Kotousov, A. (2019). Bolted joint integrity monitoring using second harmonic generation of guided waves. *Structural Health Monitoring – An International Journal*. 18(1): 193-204.
5. Yang, Y., Ng, C., Mohabuth, M., Kotousov, A. (2019). Finite element prediction of acoustoelastic effect associated with Lamb wave propagation in pre-stressed plates (under preparation).
6. Yang, Y., Ng, C., Kotousov, A. (2019). Simulation of acoustoelastic effect on second harmonic generation of Lamb wave in prestressed plate using three-dimensional finite element model 3D Finite element method (under preparation).

Conference Papers

1. Yang, Y., Ng, C., (2016). Higher harmonic generation of Lamb waves at fatigue cracks: three-dimensional finite element simulation. In *Proceedings of 10th International Conference on Structural Integrity and Failure*. Adelaide.
2. Yang, Y., Ng, C., Kotousov, A., Sohn, H., Lim, H. (2017). Fatigue crack detection using nonlinear guided wave generation. In *15th Asia-Pacific Conference on Structural Engineering and Construction*. Xi'an, China.

ACKNOWLEDGEMENT

First of all, I would like to thank my principle supervisor, Associate Professor Alex Ching-Tai Ng. Without his efforts and time on helping me through the research program, I could not be able to achieve what is presented here. He is not just an excellent supervisor, but also a good friend. He has always been encouraging me to challenge myself and support me when challenges arise. At the same time, I also want to express my gratitude for my co-supervisor, Professor Andrei Kotousov, who has also helped me a lot on theoretical understandings about my research, as well as editing my papers.

I would also like to thank my families. Their love for me is beyond any words, and I have been trying my best to make them proud. Special thanks to my mum, who has inspired me to pursue happiness and be grateful. Special thanks for my wife as well, who is always curious about the world and motivates me to experience more.

Although there may be many who remain unacknowledged in this humble note of gratitude, there are none who remain unappreciated.

It is a tough yet enjoyable journey throughout the PhD program. It gave me the opportunity to challenge my limit and the opportunity to contribute my insignificant efforts in the research area. This is a colourful and memorable journey that I take proud of.

TABLE OF CONTENTS

NOMENCLATURE

Acronyms and Initialisms

3D – Three-dimensional

FE – Finite Element

FFT – Fast Fourier Transform

GW – Guided Waves

MCPD – Maximum Cumulative Propagation Distance

NDE – Non-destructive Evaluation

NDT – Non-destructive Testing

NP – Nonlinear Parameter

SH - Second Harmonic

SHG – Second Harmonic Generation

SHM – Structural Health Monitoring

STFT – Short-time Fourier Transform

Symbols

$\mathbf{A}_{0piqj}$ – Fourth Order Elasticity Tensor

C – Right Cauchy-Green Deformation Tensor

C_p – Phase Velocity

d_{31} – Piezoelectric Charge Constant

E – Green-Lagrange Strain Tensor

F – Deformation Gradient

K_3 – Relative Dielectric Constant

l, m, n – Third Order Elastic Constants

p_0 – Dielectric Permeability

R – Rotation Tensor

S – Nominal stress tensors

T – Second Piola-Kirchhoff Stress Tensor

U – Stretch Tensor

u – Displacement Vector

W – Strain Energy

β' – Relative Nonlinear Parameter

β – Second Order Nonlinear Parameter

λ, μ – Lame Constants

ν – Poisson Ratio

ξ – Wavenumber

ρ – Density

$\boldsymbol{\sigma}$ – Cauchy Stress Tensors

LIST OF FIGURES

LIST OF TABLES

Chapter 1. Introduction

1.1. Background

Material properties are eventually degrading with time causing a threat of premature fractures. Many structures, which were built in the last century, are currently close to the end of their design life. The ageing process may result in different types of material defects, for example, cracks in metallic structures, debondings or delaminations in composite laminates as well as corrosion damage in pipes. The presence of defects can significantly jeopardise the structural integrity and public safety. Catastrophic structural failures often occur due to an incipient damage causing monetary loss and loss of life.

Serious structural failures could be initiated from a local damage area even at an unperceivable level. The relevant examples include the I-35W Mississippi River Bridge collapse [1] and Eschede train disaster [2]. Both of these failures have started from a small fatigue crack initiated from a manufacturing defect. One way to control the development of fatigue cracks is safety inspections. However, safety inspections might be costly and need the structure to be taken from operation. According to Han *et al*. [3], in the aircraft industry, maintenance and repairs represent about a quarter of the commercial aircraft operating costs. Therefore, the development of efficient and cost-effective non-destructive defect evaluation systems for periodic safety inspections and control of incipient damage is critical.

During the past few decades, many non-destructive testing (NDT) techniques were developed to evaluate the condition of the structures. These NDT techniques include visual inspection, eddy current testing, ultrasonic testing and radiographic inspection, etc. A brief summary of NDT techniques and their corresponding advantages and disadvantages can be found in the book of Gros [4]. Among these developed methods, NDT for structural health monitoring (SHM) using guided ultrasonic wave techniques has proven its advantages over other inspection techniques [5]-[7] due to its ability to scan large areas and high sensitivity to damages [8]-[10].

Guided waves (GW) is defined as stress waves forced to follow a path defined by the material boundaries of the structure. GW generally contains two different wave modes, i.e., symmetric (S) mode and antisymmetric (A) mode. The S mode is dominated by in-plane displacement of particles while the A mode is dominated by out-of-plane displacement. It is worth mentioning that, for this study the ‘low-frequency’ GW typically refers to the frequency range with the existence of only fundamental symmetric (S_0) and antisymmetric (A_0) wave modes, i.e. below

the cut-off frequency. GW propagation theory was established 100 years ago by Rayleigh and Lamb. In 1961, Worlton demonstrated the advantages of using GW to inspect plate-like structures [11]. For the recent studies, the most intensively studied type of GW is Lamb waves due to its ability to propagate in a solid plate or shell as many structures nowadays are made by plate- and shell-like components. Other types of GW include Rayleigh waves, Love waves and Stoneley waves. As compared with conventional GW inspection method using linear features of GW [12]-[18], nonlinear GW method based on the observation of higher harmonics [19],[20], sidebands (frequency mixing) [21],[23] or resonant frequency shift [24]-[25], etc., is more sensitive to micro cracks and early material degradation [26]. In this PhD study, the nonlinear characteristic of GW, i.e. second harmonic generation (SHG), is observed and studied in detail.

1.2. Aims

The primary objective of the research project is to advance the NDTs utilising nonlinear GWs, and, so, these techniques can be employed in real world environment. In order to accomplish this, it is important firstly to gain a deeper understanding of the both damage induced nonlinearities, i.e., contact, friction and material nonlinearities. GW parameters such as the excitation frequency, incident wave angle as well as the boundary reflections and loading condition, which can exert impacts on the measured second harmonic on a structure in real-life applications, are all investigated in this thesis. In addition, the intrinsic material nonlinearity is studied analytically based on the nonlinear energy function as well as numerically by using the three-dimensional (3D) finite element (FE) simulations with a nonlinear material subroutine. These investigations and studies are necessary to transfer the nonlinear-based NDT to the real world environment.

1.3. Thesis Structure

The thesis consists of eight chapters. In Chapters 2 – 5, the studies of the second harmonic generation (SHG) of GW due to the contact nonlinearity are presented with consideration of different damage types. Practically important issues that need to be dealt with before pushing forward the technique to practical applications are discussed. In Chapters 6 and 7, a theoretical analysis and FE models with a nonlinear material subroutine are conducted to study the acoustoelastic effect and SHG associated with the material nonlinearity. In the last chapter,

outcomes of the current research, conclusions and recommendations for future studies are summarised. A brief summary of the contents in each chapter is outlined as below.

Chapter 2. SHG due to contact nonlinearity at figure crack in aluminium plates is studied. The effectiveness and sensitivity of SHG using S_0 and A_0 are investigated and compared. The experimentally measured values of β' at different locations of sensors in a transducer network are compared with the corresponding 3D FE simulation results in order to validate the 3D FE model. Further, this model is implemented to study the SHG due to the contact nonlinearity. A parametric study using the experimentally validated FE model is also carried out to study the variation of β' against crack length to incident wave wavelength ratio.

Chapter 3. With the optimal wave mode and frequency, which were identified in Chapter 2, the effects of the applied load and incident wave angle on the SHG due to fatigue cracks with different crack lengths are investigated, since these effects are critical for practical implementation of the nonlinear-based GW techniques. In this chapter, Short-Time Fourier Transform (STFT) is adopted to study the SHG features under different incident wave angles and crack length to incident wave wavelength ratios, as well as different crack opening corresponding different magnitudes of the applied stress.

Chapter 4. The concept of SHG due to the contact nonlinearity is extended to study the progression of loosening of a bolted connection. This study focuses mainly on the feasibility of detecting bolt loosening using SHG of GW. Two single bolted lap joints made of steel are examined in the experimental tests supported by the FE simulations. The wave mode maximising the rate of SHG is found experimentally and numerically. In addition, 3D FE models with both loosen bolt and fatigue cracks at the bolt hole are developed to determine whether it is possible to detect and distinguish the failure type with the use of different GW modes and nonlinear effects such as SHG.

Chapter 5. In this chapter, another common damage type, debonding (delamination), is analysed along with a fatigue crack in a composite patch used to repair an aluminium plate. A 3D FE model having similar set-up to the previously validated models in Chapter 2 and 3 is utilised to study the variation of the relative nonlinear parameter with the fatigue crack length and debonding area. A feasibility study on detecting and distinguishing fatigue crack and debonding types of damage is also conducted.

Chapter 6. Besides the contact nonlinearity, material nonlinearity also contributes to the generation of the second harmonic. Structures in practical situation or in operation can be

prestressed by the applied loading or temperature. On one hand, the loads can open the crack and change the contact nonlinearity, while on the other hand, the acoustoelastic effect due to stress affects the SHG. In this chapter, a VUMAT subroutine in ABAQUS is developed based on the Murnaghan's strain energy function [27] and implemented in a 3D FE model describing a prestressed aluminium plate. The model with the material subroutine is validated with theoretical solutions of the phase velocity changes due to acoustoelastic effect associated with the applied stress.

Chapter 7. This Chapter applies the material subroutine developed in Chapter 5, to further validated the FE model by conducting an extensive validation study against previous results of experimental tests. Then, the variation of NP against propagation distance in the prestressed aluminium plate is investigated with the FE model. Finally, a new model combining the contact nonlinearity due to fatigue crack (contact nonlinearity) and material nonlinearity is developed to study the variation of NP.

Chapter 8. The significances and key findings of the conducted research are outlined in this chapter, followed by recommendations for future studies.

1.4. References

[1] Hao S 2010 *J. Bridge. Eng.* **15** 608-14

[2] Esslinger V, Kieselbach R, Koller R, Weisse B 2004 *Eng. Fail. Anal.*, **11** 515-35

[3] Han S, Palazotto A, Leakeas C 2009 *J. Aero. Eng*, **22** 185-197

[4] Gros X *1996 NDT Data Fusion* (London: Arnold)

[5] Rose LJ 2002 *J. Press. Vess. Tech.* **124** 273-82

[6] Raghavan A, Cesnik C 2007 *Shock and Vibration Digest* **39** 91-114

[7] Ng CT 2015 *Earthq. Struct.* **8** 821-41

[8] Haynes C, Todd M 2015 *Mech. Syst. Signal. Process.* **54-55** 195-209

[9] He S, Ng CT 2016 *Eng. Struct.* **127** 602-14

[10] Mitra M, Gopalakrishnan S 2016 *Smart. Mater. Struct.* **25** 0530001

[11] Worlton DC 1961 *J. Appl. Phy.* **32** 967

[12] Moreau L, Velichko A, Wilcox PD 2012 *NDT&E Inter.* **45** 46-54

[13] Casadei F, Rimoli JJ, Ruzzene M 2014 *Finite Elem. Analy. Des.* **88** 1-15

[14] Ng CT 2015 *Inter. J. Struct. Stab. Dyn.* **15** 1540010

[15] Aryan P, Kotousov A, Ng CT, Cazzolato BS 2017 *Struct. Contr. Health Monit*. **24** e1894

[16] Zhang J, Drinkwater BW, Wilcox PD, Hunter AJ 2010 *NDT&E Int.* **43** 123-33

[17] He S and Ng CT 2017 *Mech. Syst. Signal Process.* **84** 324-45

[18] Clarke T, Cawley P, Wilcox PD, Croxford AJ 2009 *IEEE Trans. Ultrason. Ferroelectr. Freq. Control* **56** 2666-78

[19] Hong M, Su Z, Wang Q, Cheng L, Qing X 2014 *Ultrason.* **54** 770-78

[20] Soleimanpour R, Ng CT 2017 *Eng. Struct.* **131** 207-19

[21] Lim HJ, Sohn H, Liu P 2014 *Appl. Phys. Lett.* **104** 214103

[22] Yoder NC, Adams DE 2010 *Struct. Health Monit.* **9** 257-67

[23] Klepka A, Staszewski WJ, Jenal RB, Szwedo M, Iwaniec J, Uhl T 2011 *Struct. Health Monit.* **11** 197-211

[24] TenCate JA, Smith E, Guyer RA 2000 *Phys. Review Lett.* **85** 1020-23

[25] Chondros TG 2011 *J. Sound Vib*. **239** 57–67

[26] Bermes C, Kim JY, Qu J, Jacobs LJ 2008 *Mech. Syst. Signal Process.* **22** 638-646

[27] Murnaghan FD 1937 *Am. J. Math*. **59** 235-260

Chapter 2. Second Harmonic Generation at Fatigue Cracks by Low-Frequency Lamb Waves: Experimental and Numerical Studies

(Paper 1, Published)

Yi Yang[a], Ching-Tai Ng[a], Andrei Kotousov[b], Hoon Sohn[c], Hyung Jin Lim[c]

[a] School of Civil, Environmental and Mining Engineering, The University of Adelaide, Adelaide, SA 5005, Australia

[b] School of Mechanical Engineering, The University of Adelaide, Adelaide, SA 5005, Australia

[c] Department of Civil and Environmental Engineering, KAIST, Daejeon, 305-701, South Korea

Publication:

Yang Y, Ng CT, Kotousov A, Sohn H, Lim HJ 2018 *Mech. Syst. Signal. Process.* **99** 760-73

Statement of Authorship

Title of Paper	Second harmonic generation at fatigue cracks by low-frequency Lamb waves: Experimental and numerical studies.
Publication Status	☑ Published ☐ Accepted for Publication ☐ Submitted for Publication ☐ Unpublished and Unsubmitted work written in manuscript style
Publication Details	Yang, Y., Ng, C., Kotousov, A., Sohn, H., & Lim, H. (2018). Second harmonic generation at fatigue cracks by low-frequency Lamb waves: Experimental and numerical studies. *Mechanical Systems and Signal Processing*, *99*, 760-773

Principal Author

Name of Principal Author (Candidate)	Yi Yang
Contribution to the Paper	Undertook literature review, designed experimental tests and developed numerical models, performed data processing and prepared manuscript
Overall percentage (%)	80%
Certification:	This paper reports on original research I conducted during the period of my Higher Degree by Research candidature and is not subject to any obligations or contractual agreements with a third party that would constrain its inclusion in this thesis. I am the primary author of this paper.
Signature	Date 10/05/2018

Co-Author Contributions

By signing the Statement of Authorship, each author certifies that:

i. the candidate's stated contribution to the publication is accurate (as detailed above);

ii. permission is granted for the candidate in include the publication in the thesis; and

iii. the sum of all co-author contributions is equal to 100% less the candidate's stated contribution.

Name of Co-Author	Ching-Tai Ng
Contribution to the Paper	Helped experiments and model development, helped review manuscript and prepare for submission, and acted as corresponding author
Signature	Date 4/1/2019

Name of Co-Author	Andrei Kotousov
Contribution to the Paper	Helped evaluate and edit the manuscript.
Signature	Date 4/1/2019

Name of Co-Author	Hoon Sohn		
Contribution to the Paper	Helped evaluate and edit the manuscript.		
Signature		Date	27/6/2018

Name of Co-Author	Hyung Jin Lim		
Contribution to the Paper	Helped evaluate and edit the manuscript.		
Signature		Date	26/6/2018

Abstract

This paper presents experimental and theoretical analyses of the second harmonic generation due to non-linear interaction of Lamb waves with a fatigue crack. Three-dimensional (3D) finite element (FE) simulations and experimental studies are carried out to provide physical insight into the mechanism of second harmonic generation. The results demonstrate that the 3D FE simulations can provide a reasonable prediction on the second harmonic generated due to the contact nonlinearity at the fatigue crack. The effect of the wave modes on the second harmonic generation is also investigated in detail. It is found that the magnitude of the second harmonic induced by the interaction of the fundamental symmetric mode (S_0) of Lamb wave with the fatigue crack is much higher than that by the fundamental anti-symmetric mode (A_0) of Lamb wave. In addition, a series of parametric studies using 3D FE simulations are conducted to investigate the effect of the fatigue crack length to incident wave wavelength ratio, and the influence of the excitation frequency on the second harmonic generation. The outcomes show that the magnitude and directivity pattern of the generated second harmonic depend on the fatigue crack length to incident wave wavelength ratio as well as the ratio of S_0 to A_0 incident Lamb wave amplitude. In summary, the findings of this study can further advance the use of second harmonic generation in damage detection.

Keywords: nonlinear Lamb wave, second harmonic, fatigue crack, contact nonlinearity, finite element method, experimental study

2.1. Introduction

2.1.1. Lamb waves

Over the lifespan, engineering structures accumulate mechanical damage due to fatigue, temperature variations, effects of aggressive environment and aging. Without proper inspection and maintenance strategies to ensure the safety and integrity of the structures, the accumulation of the damage can lead to catastrophic consequences. Therefore, the development and deployment of non-destructive evaluation (NDE) and structural health monitoring (SHM) are critical to ensure the structural safety, minimize the maintenance costs, and extend the service life of the structures.

Among various NDE and SHM techniques, Lamb wave has attracted significant attention due to its outstanding properties, such as ability to propagate a long distance, able to provide rapid inspection, high sensitivity to many types of mechanical damages, and detection of damages at inaccessible at locations [1]-[4]. In the last two decades, different Lamb wave based techniques [5]-[9] have been developed for damage detection. The majority of the developments focused on linear Lamb wave that determines the presence of damage based on the change of wave speed, reflection and transmission, or mode conversion [10] of the linear wave signals, i.e. the scattered wave at the same frequency as the incident wave [11]-[13]. The linear features of Lamb wave are sensitive to damages with sizes comparable to the wavelength of the incident wave, e.g. corrosion spot [14][15] or crack [17][18]. However, they are not effective in detecting early stage of mechanical damage, e.g. micro-damage and small fatigue crack. In addition, most of the damage detection techniques based on the linear Lamb wave require baseline data [3] to extract the scattered wave signal from the damage. But the change of environmental conditions, e.g. temperature variation [19]-[21], stress level [22] could make the baseline subtraction fail in extracting the scattered waves signal from the damages. Therefore, there is a need to overcome the aforementioned deficiencies of the linear wave signals to achieve effective and practical damage detection.

2.1.2. Nonlinear Lamb waves

Nonlinear ultrasonic techniques detect the incipient damage based on nonlinear phenomena, such as higher harmonic generation [23], sub-harmonic generation [24], mixed frequency response [25],[26] and nonlinear resonance [27]. A number of studies have demonstrated that the nonlinear characteristics and phenomena are more sensitive to the presence of contact-type damage, such as fatigue crack and delamination, and have less influence by environmental change than the linear features.

Early developments of the nonlinear ultrasonic techniques focused on the nonlinearity of elastic bulk waves [28]-[30]. Recently, several studies have focused on the nonlinearity of Lamb waves [31]. Compared to the nonlinear ultrasonic techniques based on the bulk waves, nonlinear Lamb waves could provide long-range inspection for thin-wall structures. A number of studies have demonstrated that the generation of second- or third-order harmonics could be used to determine the presence and severity of incipient damage in structures [32]. The generation of higher harmonics involves various non-linear phenomena. However, recent

studies have primarily focused on the investigations of the higher harmonic generation due to nonlinear elasticity [23] and contact nonlinearity [34],[35].

The early damage accumulation usually leads to the deviation of the stress-strain behavior from the linear Hook's law. The higher harmonics are generated due to this nonlinearity in the elastic behavior of the material, and this provides a way for the measurement and quantification of the micro-damage. The material nonlinearity normally leads to distortion of propagating waveforms, and hence, it generates the higher harmonic. A number of studies focused on the material nonlinearity were performed by several researchers [23], [33], [34]-[38].

Lamb waves are dispersive and have multi-mode nature, which make accurate experimental realization of nonlinear Lamb wave become difficult. As illustrated in the aforementioned studies, the phase and group velocity matching are essential conditions to generate cumulative behavior of the second harmonic, i.e., the magnitude of second harmonic increases with wave propagation distance [23]. These conditions ensure that the second harmonic Lamb wave can propagate a reasonably long distance and can be detected. Pruell *et al.* [33] found that the plasticity-induced damage can cause the second harmonic generation. Li *et al.* [36] employed the second harmonic Lamb waves to assess thermal fatigue damage in composite laminates. Zhou *et al*. [37] carried out an experiment study to demonstrate that the higher harmonic Lamb wave can be used to evaluate the fatigue crack. They found that the nonlinearity contributed by the material itself, i.e. the nonlinear elasticity effect, is insignificant compared with that induced by the fatigue damage.

When Lamb wave interacts with contact-type of damage, e.g. fatigue crack [34] and delamination [39],[40], higher harmonics can be generated due to the contact nonlinearity. This happens due to the nonlinear interaction of the crack surfaces caused by the incident Lamb wave. When the incident wave passes through the crack, the compressive pressure of the incident wave closes the crack and the tensile pressure opens the crack. As a result, the compressive part of the incident wave penetrates the crack, while the tensile part cannot. This phenomenon is schematically illustrated in [32]. This clapping behavior at the crack surfaces causes the nonlinearity, and hence, generating the higher harmonics due to the effect of localized nonlinearity [32].

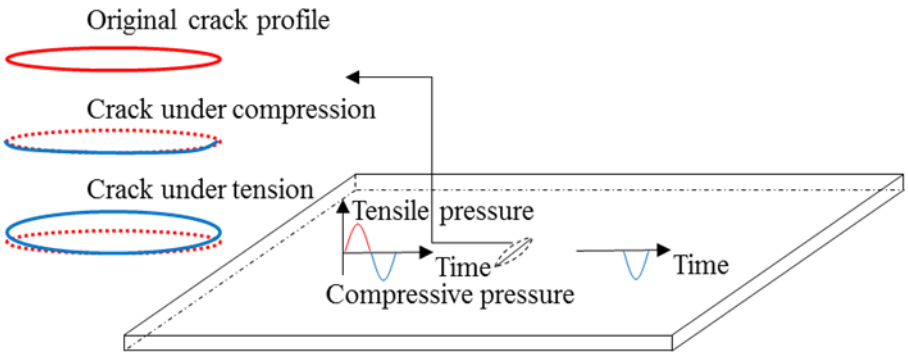

Figure 2-1: Concept of contact nonlinearity at a fatigue crack

A number of studies have investigated the generation of higher harmonics by low-frequency incident guided wave, i.e. below 500 kHz. Nucera and Lanza di Scalea [41] investigated the nonlinear guided wave in multi-wire strands. They demonstrated that the higher harmonics generated by the inter-wire contact at different axial load levels. Two- (2D) and three-dimensional (3D) finite element (FE) simulations considered the contact nonlinearity arising from the inter-wire stresses between individual wires comprising the strand were carried out to study the higher harmonic generation. Experimental study was conducted to verify this phenomenon. Shen and Giurgiutiu [34] proposed a 2D FE model to study the nonlinear guided waves generated by low-frequency incident wave interaction with a breathing crack. They considered the effect of contact nonlinearity in their model and investigated the generation of higher harmonics by the fundamental symmetric (S_0) and anti-symmetric (A_0) mode of Lamb wave. They also demonstrated that the FE model is capable to describe the nonlinear wave propagation phenomenon. Soleimanpour and Ng [39] investigated the higher harmonic generated by A_0 mode Lamb wave interaction with a delamination in laminated composite beams. A 3D FE model with the contact nonlinearity at the delamination was used to study the generation of the higher harmonics. The FE model was experimentally verified and then applied to investigate the higher harmonic generation. Yelve *et al*. [40] investigated the higher harmonics generation by the interaction of S_0 Lamb wave with a delamination. A 2D FE model with contact effect at the surfaces of the delamination was used to investigate the higher harmonic generation. In addition, experimental studies were also carried out to further validate the results. They demonstrated that the contact nonlinearity could generate higher harmonics.

The aforementioned studies with the low-frequency incident Lamb wave did not require the phase and group velocity matching for generating the cumulative higher harmonics. Therefore,

the main contribution to the higher harmonic generation was mainly due to the contact nonlinearity at the contact surfaces of the damage. In general, the use of the low-frequency incident Lamb wave to detect the damage based on the higher harmonic generation due to contact nonlinearity is easier to be experimentally achieved than that of due to material nonlinearity. This is because the contact nonlinearity does not require highly accurate experimental procedure and sophisticated equipment to satisfy the phase and group velocity matching condition. In addition, Lamb wave at low excitation frequency range only has S_0 and A_0 mode, therefore, the excitation will not induce higher-order modes of Lamb wave for both incident and higher harmonic Lamb wave. Hence, it does not require advanced signal processing and experimental techniques to extract the higher harmonic information from the measured data.

Currently there are limited studies focused on the higher harmonic generation of Lamb wave at the fatigue crack due to contact nonlinearity, especially for study using both 3D FE simulations and experimentally measured data. Moreover, the majority of the previous studies focused on the situation when fatigue crack is oriented perpendicular to the incident wave propagation direction, i.e. only forward and backward directions of the higher harmonic Lamb wave were studied. In practical applications where transducer arrays are used for damage detection, the fatigue crack can be oriented at different angles with respect to the incident wave direction. Different magnitudes of higher harmonic Lamb waves could be generated at different scattering angles. Therefore, it is important to gain a physical insight into the higher harmonics generated by contact nonlinearity at the fatigue crack. The insight can further advance the use of the higher harmonic Lamb waves for damage detection, specifically for small-scale and micro-damage.

In this study, comprehensive 3D FE simulations and experimental studies are carried out to investigate the second harmonic generation at the fatigue crack due to the contact nonlinearity using S_0 and A_0 Lamb wave. The magnitude of the higher harmonics generated by S_0 and A_0 Lamb wave is investigated in detail. In addition, this study investigates the directivity pattern of the higher harmonic generation. This provides further understanding of the higher harmonic generation phenomenon.

This study also demonstrates the feasibility of using the 3D FE simulation to predict the higher harmonics generation due to Lamb wave interaction with the fatigue crack. The FE simulation provide many benefits, such as substantial reduction of time and cost in the investigations.

Noticeably, there are other numerical simulation techniques, such as boundary element method (BEM), finite difference (FD) method and spectral finite element method (SFE) method, for solving guided wave propagation problems [42]. Apart from FE method, SFE method has also attracted attention in the last decade [43]-[45]. This method is more computational efficient compared with FE method, especially for simulating high frequency wave propagation where the required element size for ensuring the accuracy of the FE simulation becomes very small. However, FE simulation has been commonly used to simulate guided wave propagation problems [16], [34], [37] due to its ability in modelling complex geometries [42] and the availability of well-established commercial software programs. Therefore, this study employs the FE simulation to study the second harmonic generation.

The paper is organized as follows. Section 2 describes the details of the 3D explicit FE simulations, which include the actuator and sensor model, and modeling of the fatigue crack. Section 3 presents the experimental validation, which describes the details of the fatigue crack generation through cyclic tests, experimental setup for actuating and sensing the Lamb wave, and mode-tuning results for generating a specific mode of Lamb wave. Section 4 discusses the results obtained from the numerical simulations and experiments. Section 5 presents a parameter study considering different incident wave wavelength to crack length ratios. The paper also presents a comprehensive study of the magnitude and scattering directivity pattern of the second harmonic generation. Finally, conclusions are drawn in Section 6.

2.2. Three-dimensional Explicit Finite Element Simulation

The Lamb wave propagation and interaction with the fatigue crack in an aluminum plate was modeled using a 3D explicit FE method. The dimensions of the aluminum plate are 300mm×200mm×3mm. Eight piezoceramic discs with 10mm diameter and 0.5mm thickness were modeled on the surface of the aluminum plate to excite and measure the Lamb wave signals. The materials of the aluminum plate and piezoceramic discs are 5005-H34 aluminum and Pz27, which are the same as the specimen used in experiment in Section 3. The Young's modulus, Poisson's ratio and density of 5005-H34 aluminum are 69.5GPa, 0.33 and 2700kg/m^3, respectively. The material properties of the piezoceramic discs are shown in Table 2-1. The eight piezoceramic discs, which are labeled as PZT1–PZT8, form a 50mm diameter circular transducer network as shown in Figure 2-2. Based on the polar coordinate shown in the Figure 2-2, they are located at r = 50mm and θ = 0° (PZT1), 45° (PZT2), 90° (PZT3), 135° (PZT4),

180° (PZT5), 225° (PZT6), 270° (PZT7) and 315° (PZT8), respectively. The same configuration of the transducer network was also used in the experimental studies and it will be described in the next section. In this study, PZT5 was used to actuate Lamb waves while the rest of the piezoceramic discs were used for sensing.

Table 2-1: Material properties of the model piezoceramic discs

Young's modulus	Poisson's ratio	Density	Relative dielectric constant K_3	Piezoelectric charge constant d_{31}	Dielectric permeability p_0
59GPa	0.389	7700kg/m^3	1800	170×10^{-12}m/V	8.85×10^{-12}F/m

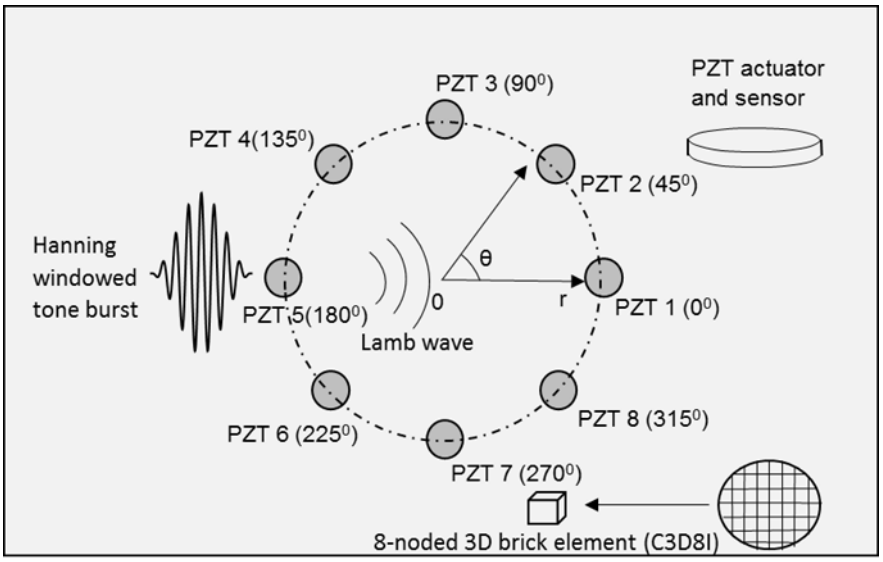

Figure 2-2: Schematic diagram of the FE simulations and experiments

Commercial FE software, ABAQUS/CAE, was used to construct the 3D FE model. Eight-noded 3D fully integrated linear brick elements, C3D8I, in which each node has three translational degrees-of-freedom (DoFs), were used to model the aluminum plate and the piezoceramic discs. The in-plane dimensions and the thickness of the elements are around 0.4mm×0.4mm and 0.375mm, respectively, so that there are at least 20 elements per wavelength for the incident and generated second harmonic Lamb wave. In the thickness direction of the aluminum plate, there are eight layers of the brick elements. The aspect ratio of the brick elements is 1.07. The simulation was solved using the explicit FE code,

ABAQUS/Explicit, which employs the explicit central different integration scheme to calculate the response of the wave propagation. The excitation signal is a sinusoidal tone burst pulse modulated by a Hanning window, which is applied to the actuator model described in next sub-section to excite the Lamb wave in the aluminum plate.

2.2.1. Actuator and sensor model

In this study, the piezoceramic discs used for excitation and measurement were modeled using 3D brick elements in the FE simulations with the consideration of the direct and converse piezoelectric effects. The bonding between the piezoceramic discs and the aluminum plate is assumed to be perfect, and hence, the strain is continuous at interface between the piezoceramic disc and the aluminum plate. The radial displacement at the circumference of the actuator has a linear relationship with the input voltage [46][47] as

$$d_r = R\frac{d_{31}}{h_{PZT}}\left[\frac{\tilde{E}(1-\nu_{PZT})}{E_{PZT}} + 1\right]V_{in} \tag{2.1}$$

where V_{in} is the applied voltage. d_{31}, R, E_{PZT}, ν_{PZT} and h_{PZT} are charge constant, radius, Young's modulus, Poisson's ratio and thickness of the piezoceramic discs, respectively. $\tilde{E}$ is a constant related to the material properties and thickness of the plate and piezoceramic disc, and it is given in [47]. The excitation signal in the form of voltage is converted to displacement based on the material properties of the piezoceramic discs using equation (2.1) and is then applied to the FE nodes of the piezoceramic disc to generate the Lamb wave.

For the sensor model, the output voltage is related to the radial and tangential strains [46][47] of piezoceramic discs as

$$V_{out} = \frac{d_{31}E_{PZT}h_{PZT}}{4\pi K_3 p_0 R^2(1-\nu_{PZT})}\iint(\varepsilon_r + \varepsilon_\theta)r_{PZT}dr_{PZT}d\theta_{PZT} \tag{2.2}$$

where r_{PZT} and θ_{PZT} are the radial and tangential direction, respectively, of the polar coordinate located at the center of each piezoceramic disc. K_3 is the dielectric constant of the piezoceramic discs, p_0 is the dielectric permeability. ε_r and ε_θ are radial and tangential strain component, respectively. Integrating equation (2.2) with respect to r_{PZT} and θ_{PZT}, we can obtain

$$V_{out} = \frac{d_{31}E_{PZT}h_{PZT}}{4K_3 p_0(1-\nu_{PZT})}(\varepsilon_r + \varepsilon_\theta) \tag{2.3}$$

Hence, the measured voltage by the sensor could be obtained from the strain of the brick elements that used to model the piezoceramic discs in the FE simulations.

2.2.2. Modelling of fatigue crack

The fatigue crack was modeled by embedding a seam crack at the fatigue crack position in the aluminum plate model. Figure 2-3 shows a schematic diagram of the fatigue crack model. The fatigue crack was modeled by duplicating and overlapping the nodes along the seam crack, and hence, it is originally closed but it could be opened when Lamb waves interacting with the fatigue crack. Hard normal contact and friction tangential contact are applied to the interfaces of the seam crack to prevent nodes penetration, and hence, simulating the breathing behavior when the Lamb wave interacts with the fatigue crack. A typical friction coefficient of aluminum [48] is used and the value is slightly increased to take into account the roughness of the actual fatigue crack surfaces. In this study, a friction coefficient of 1.5 was used to simulate the relative sliding of the fatigue crack surfaces. For the experiment validation in the next section, the fatigue crack was generated and controlled using a circular through hole with starter notches in the fatigue loading process. For validating the FE model with the experimental measurements, the circular through hole and the starter notches are also modeled by removing the elements in the FE model.

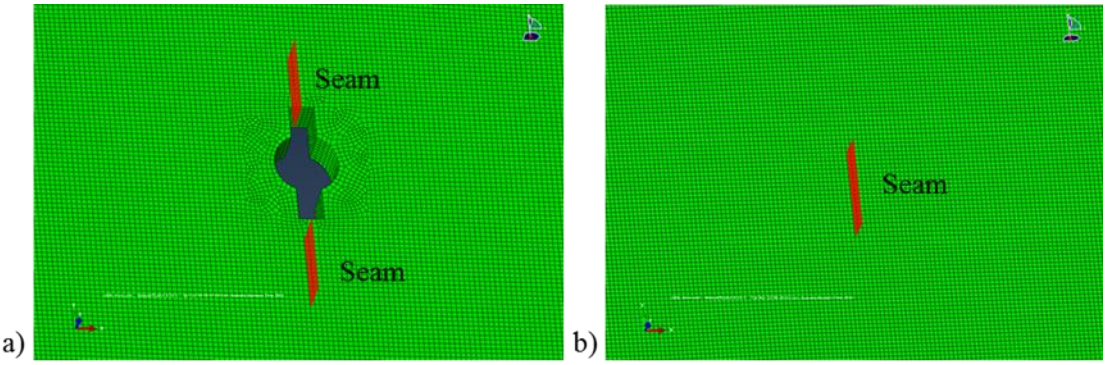

Figure 2-3: FE model of the fatigue crack for simulating the a) experimental condition, and b) numerical parametric study

2.3. Experiment

2.3.1. Fatigue test

Two 300mm×200mm×3mm 5005-H34 aluminum plates having the same material properties as the plate model in the FE simulations were used in the experiment. A 5mm diameter circular through hole was machined at the center of one of the aluminum plates and two 2mm long starter notches were cut using a 1mm thick saw blade. One of the plates was subjected to a sinusoidal tensile load in an INSTRON 1432 testing machine. The cyclic tension load was applied with a minimum of 5kN and a maximum of 40kN with a frequency of 10Hz. The plate was inspected every 5,000 cycles of loading and it took approximately 60,000 cycles to initiate the fatigue crack at the end of the starter notch. The cyclic loading process was stopped when the fatigue cracks propagate to approximately 10mm long as shown in Figure 2-4. The other aluminum plate was used as the control specimen, and hence, it is an intact aluminum plate. It is used to quantify the second harmonic induced from non-damage related effects, such as material nonlinearity, the interaction between transducers and host plate, and instrumentation chain, etc.

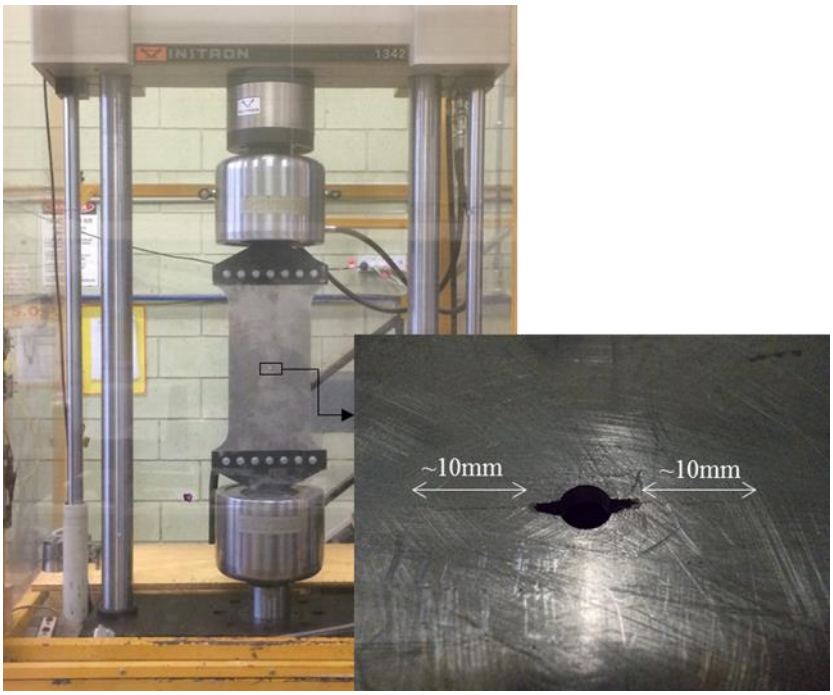

Figure 2-4: Fatigue testing using INSTRON and the fatigue crack generated at the end of the starter notches]

2.3.2. Experimental setup for actuating and sensing Lamb wave

Eight 10mm diameter and 0.5mm thick piezoceramic discs (Ferroperm Pz27) were bonded to the surface of the aluminum plates using conductive epoxy for exciting and sensing the Lamb wave. The piezoceramic discs were installed after the completion of the fatigue testing to avoid the possible degradation of the adhesive layers between the surface of the piezoceramic discs and the plate during the fatigue testing. The material properties and positions of the piezoceramic discs were the same as those in the FE simulations. A computer controlled signal generator NI PIX-5412 was used to generate a narrow-band sinusoidal tone burst pulse modulated by a Hanning window and it was applied to the PZT5 (r = 50 mm and θ = 180°) as shown in Figure 2-2 to generate the Lamb wave. The peak-to-peak voltage of the output signal is 10V. It was amplified by a factor of 5 using an amplifier (KROHN-HITE 7500) before it was sent to the PZT5. The rest of the piezoceramic discs (PZT1-PZT4 and PZT6-PZT8) were used to measure the Lamb wave. The signals measured by the piezoceramic discs were digitized by a data acquisition system (NI PXIe-5105) and then fed into the computer. The sampling rate was 6 MHz and the quality of the measurements was improved by averaging the signals in the time domain with 64 acquisitions.

2.3.3. Mode-tuning of Lamb wave

In this study, the second harmonic generation by the interaction of S_0 and A_0 Lamb waves at fatigue cracks were investigated individually. A mode-tuning experiment [49] was first carried out to determine the optimal excitation frequencies that could maximize the amplitudes of the S_0 and A_0 mode responses, respectively. A pair of piezoceramic discs with 10mm diameter and 0.5mm thickness were attached to the surface of a 1000mm×1000mm×3mm aluminum plate with the same material properties as those used in the fatigue testing. The 4-cycle narrow-band sinusoidal tone burst pulse modulated by a Hanning window swept from 10kHz to 400kHz in steps of 20kHz was applied to one of the piezoceramic discs to generate the Lamb wave and the rest of the piezoceramic discs were used for measurements. At each excitation frequency, the amplitudes of the S_0 and A_0 Lamb wave were recorded. Figure 2-5 shows the mode-tuning results. The A_0 Lamb wave is dominant at low excitation frequencies. The amplitude of the S_0 Lamb wave increases with the excitation frequency and has similar magnitude as the A_0 Lamb wave at 160kHz. The S_0 Lamb wave then becomes dominant at higher excitation frequencies. As shown in Figure 2-5, the ratios of A_0 to S_0 and S_0 to A_0 Lamb wave amplitudes are maximized at 30kHz and 240kHz, respectively. Therefore, the excitation frequency of 30kHz

and 240kHz were chosen to excite the dominated A_0 and S_0 Lamb wave in the rest of the study, respectively.

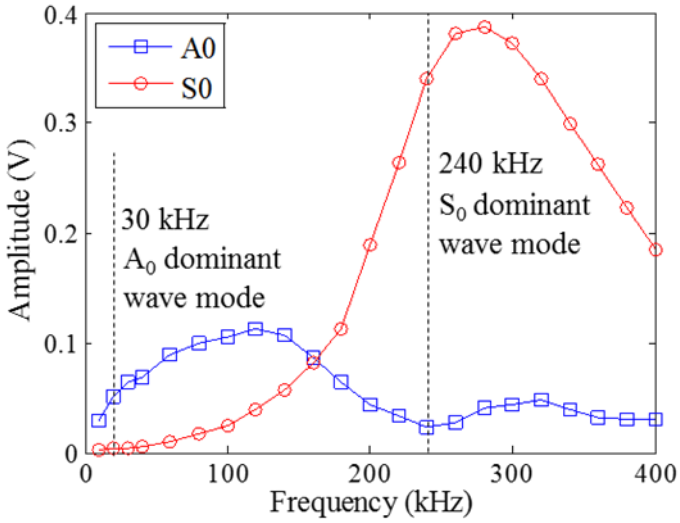

Figure 2-5: Lamb wave mode-turning curve for 3mm thickness 5005-H34 aluminum plate excited by a 10mm diameter and 5mm thick piezoceramic disc

2.3.4. A_0 and S_0 Lamb wave

In this section the FE simulated and experimentally measured A_0 and S_0 Lamb wave are compared. Based on the mode-tuning results in Section 3.3, the 30 kHz and 240kHz narrow-band sinusoidal tone burst pulse modulated by a Hanning window were applied separately to the PZT5 of the transducer network to generate Lamb wave in the intact aluminum plate. Figure 2-6 shows a comparison between the numerical simulated and experimentally measured 30kHz A_0 and 240kHz S_0 Lamb wave at PZT2 and PZT4. Both of the numerical simulated and experimentally measured Lamb wave signals are normalized with respect to their maximum values. The results show that there is good agreement between the numerically simulated and experimentally measured A_0 and S_0 Lamb wave.

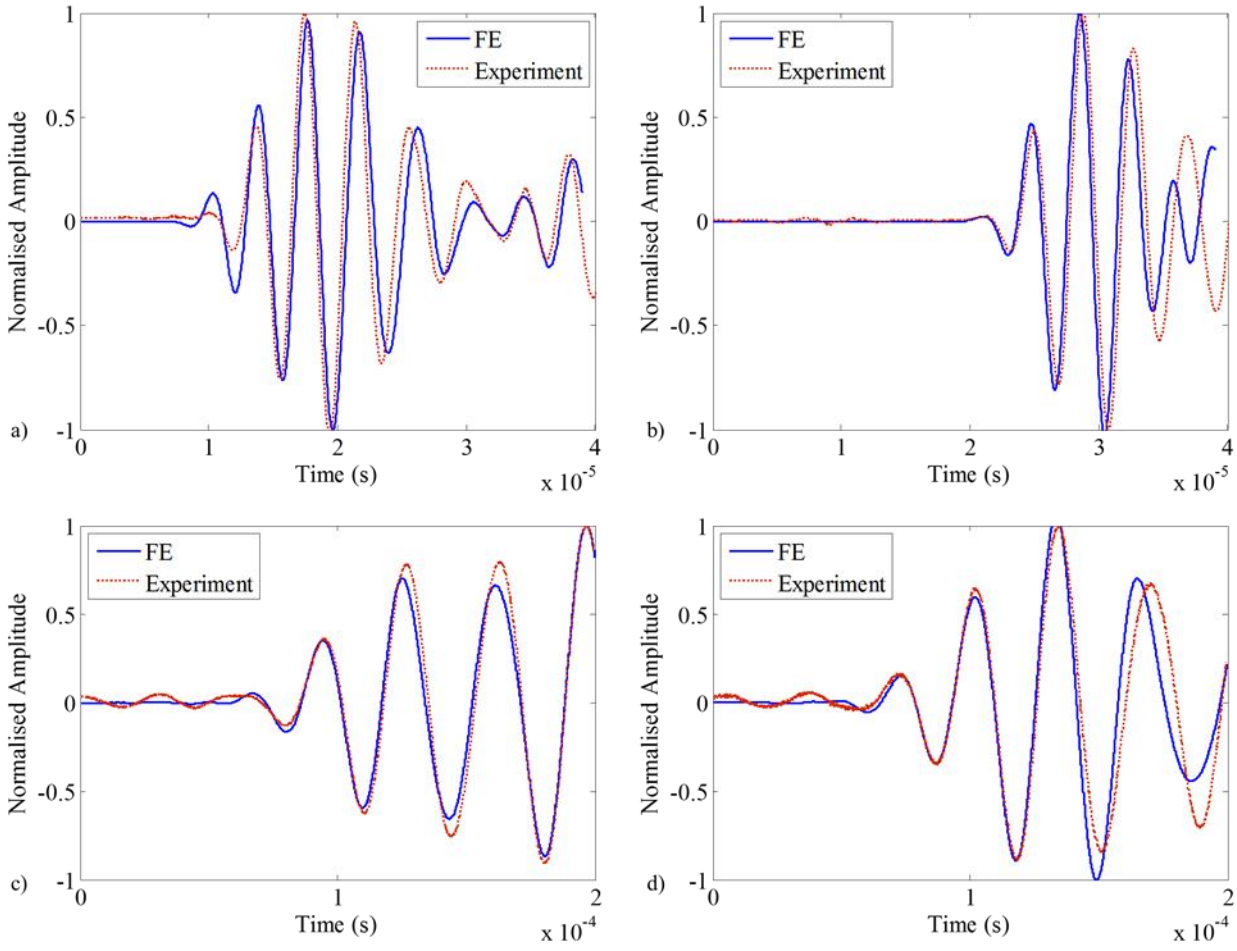

Figure 2-6: Numerical simulated and experimental measured Lamb wave signal, a): 30 kHz wave at PZT2, b): 30kHz wave at PZT4, c): 240kHz wave at PZT2, and d): 240kHz wave at PZT4

2.4. Results and Discussions

Experimental measurements of the second harmonic generation were carried out using the two aluminum plates described in Section 3.1, i.e. the intact plate and the plate with 10mm long fatigue cracks generated at the end of the starter notches of the circular hole. The number of cycles for excitation signals was increased to eight cycles to reduce the excitation frequency bandwidth in frequency domain. This ensures the generated second harmonic would not overlap with the excitation frequency components in the frequency domain. The 30kHz and 240kHz excitation signals were applied to the PZT5 to generate the A_0 and S_0 dominated Lamb wave, respectively. The rest of the piezoceramic discs in the transducer network were used for measurements.

The measured signals in both experiments and FE simulations have the same total duration, i.e. 1.6ms, which covers the incident and reflected signals from boundaries. The measured signals were then transformed to the frequency domain using Fast Fourier Transform (FFT). The spectra of the signals measured by PZT6 for the incident A_0 and S_0 Lamb wave in the intact and the plate with the fatigues cracks are shown in Figure 2-7a and b, respectively. As shown in Figure 2-7, the spectra of A_0 and S_0 incident Lamb waves have maximum values around their excitation frequencies, i.e. 30kHz and 240kHz, respectively. As described in Section 1, the second harmonic would occur at the double of the excitation frequency, i.e. 60kHz and 480kHz for the A_0 and S_0 incident Lamb wave used in this study, respectively. However, Figure 2-7a shows that only a small magnitude of second harmonic is generated by the incident A_0 Lamb wave interacting with the fatigue crack. For the results of the S_0 incident Lamb wave as shown in Figure 2-7b, the magnitude of the second harmonic at 480kHz can be clearly observed. However, the result of the intact plate still has a very small magnitude of the non-damaged related second harmonic. These non-damaged related nonlinearities were possibly caused by intrinsic material nonlinearity, connections between plate and transducers, instrumentation or background noise. Since the magnitude of the non-damaged related nonlinearities is much smaller than the second harmonic generated by the interaction of the Lamb wave with the fatigue crack, it was ignored in this study.

For the third harmonic of the Lamb waves, i.e. at 90kHz for A_0 Lamb wave and 720kHz for S_0 Lamb wave, both undamaged plate and the plate with the fatigue crack have similar amplitudes. In the literature, a spectral damage index [50] was proposed to take into account the generation of third and fourth harmonic at a breathing crack. In their study, the energy of the fundamental harmonic is transferred to higher harmonics due to intensive contact nonlinearity at the breathing crack. However, for the present study, the amplitude of the third harmonic is less than 1% of the amplitude of the second harmonic, the generated third harmonic can be neglected in this study.

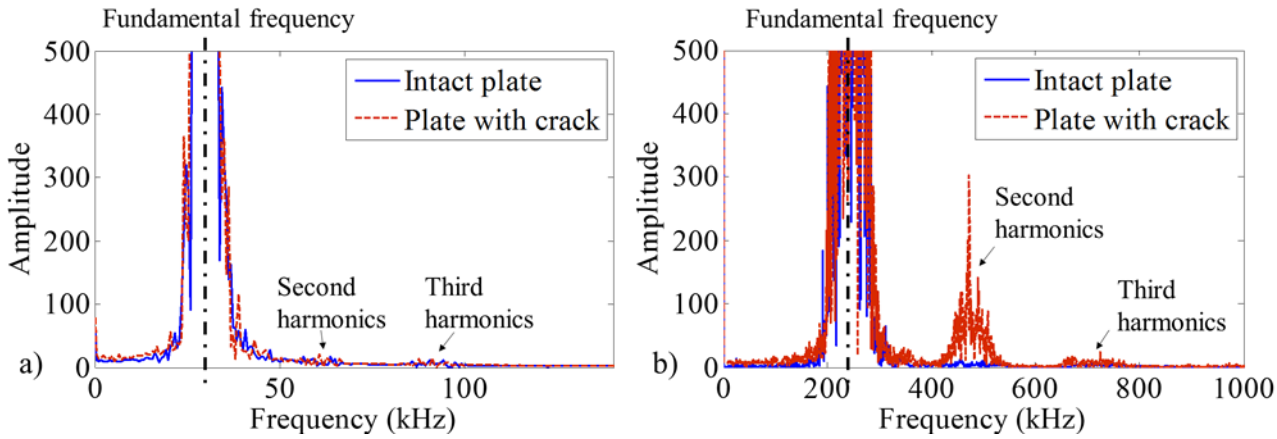

Figure 2-7: Spectra of the signals measured from PZT6 of the intact plate and the plate with the fatigue crack for the incident a) A0 (30kHz) and b) S0 Lamb wave (240kHz)

There are four possible sources of nonlinearity, (i) contact nonlinearity at the crack, (ii) nonlinear elasticity of material, (iii) inherent nonlinearity of electrical equipment, and (iv) background noise. In general, the contact nonlinearity at the crack is usually much larger than the other three possible sources of nonlinearity [51]. Therefore, the higher harmonic induced by the crack is usually dominant in the measured signal, and hence, it is assumed that the second harmonic is mainly contributed by the contact nonlinearity. In this study a relative nonlinear parameter β_C' is defined to quantify the generation of the second harmonic due to the contact nonlinearity at the fatigue crack. The relative nonlinearity parameter β_C' is defined as [51]

$$\beta_C' = \frac{A_2}{A_1^2} \tag{2.4}$$

where A_1 and A_2 are the magnitude of fundamental component and second harmonic component estimated from the Fourier transform of the measured signal at the piezoceramic disc. In both FE simulations and experimental studies, β_C' of the data measured by each piezoceramic disc is normalized by the mean of β_C' of all piezoceramic discs.

2.4.1. Effect of incident wave modes

Figure 2-8 shows the calculated values of the nonlinear parameter obtained by using 240kHz (S_0 dominated), 160kHz (S_0 and A_0 mixed) and 30kHz (A_0 dominated) incident waves. The relative nonlinear parameter of the measured signals from the sensor on the damaged plate (β_C')

is normalized to the corresponding value obtained from the intact plate (β'_{C0}). For the S_0 Lamb wave (i.e. at 240kHz), the value of the normalized relative nonlinearity parameter is much larger than 1 at all transducers, which indicates the presence of fatigue cracks in the plate.

At 160kHz as shown in the mode-tuning curve (Figure 2-5), the incident wave contains similar magnitudes of A_0 and S_0 incident Lamb wave. According to Figure 2-8, the values of normalized relative nonlinear parameter are all larger than 1. Although the value is much smaller than the case when S_0 dominated incident Lamb wave is used, it can still be used to indicate the fatigue crack.

For the results at 30kHz, i.e. A_0 dominated incident wave, the value of the normalized relative nonlinear parameter is less than 1 at most of the sensors. This demonstrates that there is not much second harmonic generated due to the contact nonlinearity at the fatigue crack when A_0 dominated incident Lamb wave is used. Overall, the results indicate that the S_0 dominated incident Lamb wave could generate relative large magnitude of second harmonic compared to A_0 dominated, and S_0 and A_0 mixed incident Lamb wave.

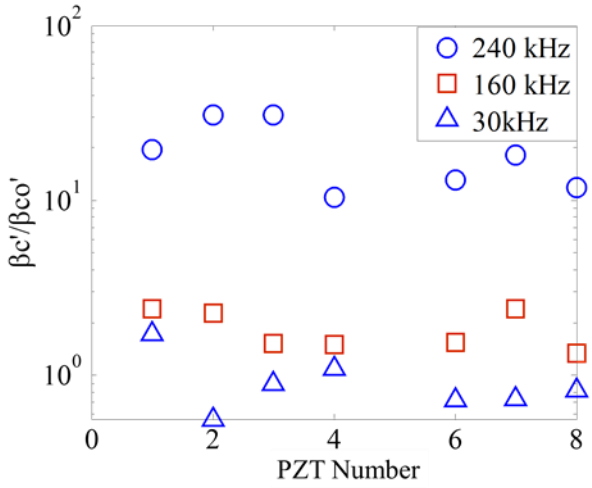

Figure 2-8: Normalized relative nonlinear parameter obtained at all transducers on damaged plate using 240kHz (S0) and 160kHz and 30kHz (A0) Lamb waves

2.4.2. Comparison of results between finite element simulations and experiments

As discussed in the previous section, using the A_0 dominated incident Lamb wave (30kHz) does not generate much second harmonic as compared to the results of using either S_0 (240kHz) dominated or S_0 and A_0 mixed (160kHz) incident Lamb wave. Therefore, the comparison between the experimental and FE results only focuses on the S_0 dominated and S_0 and A_0 mixed

incident Lamb wave at 240kHz and 160kHz, respectively. There are some discrepancies between the experimentally and numerically obtained normalized relative nonlinear parameter due to the facts that:

i. The fatigue crack in experiment could be initially open or partially closed, and hence, a certain amount of wave energy is used to close and re-open the crack. While in FEM, the crack surfaces are initially closed.
ii. The crack is modeled as two straight lines in the FE model with an assumed value of friction factor between crack contact surfaces. While the actual shape of fatigue crack is not perfectly straight, and the friction factor and interaction behavior might vary along the fatigue crack in the experiment.
iii. The nonlinearities as discussed at the beginning of Section 4, were not fully modelled. Though these nonlinearities are small compared with the contact nonlinearity, they may also contribute to the discrepancy between the experimental and numerical results.

It is difficult to perfectly predict the actual values of β_C' considering the aforementioned factors. Instead, the directivity patterns of the β_C' at different sensors are studied, which provide useful information about the scattering feature of the nonlinear Lamb wave at the fatigue crack. In the rest of this section, the β_C' value measured at each piezoceramic disc is normalized to the averaged β_C' values of all piezoceramic discs for the FE and experimental results. As shown in Figure 2-9, there is good agreement between FE simulated and experimentally measured second harmonic directivity patterns when S_0 (240kHz) and S_0 and A_0 mixed (160kHz) incident Lamb wave are used. It can be seen that the normalized relative nonlinear parameters of PZT2, PZT3 and PZT4 have very similar magnitudes to the PZT8, PZT7, PZT6, respectively, as they are located symmetrically about the incident wave propagation direction (perpendicular to the fatigue crack) in the FE simulations. Figure 2-9 shows that the experimentally obtained values of the relative nonlinear parameters for the aforementioned piezoceramic transducers are not distributed as symmetric as the FE results. This is because the generated fatigue cracks at both ends of the starter notches are perfectly the same in the FE simulation but they are different in the experiment. Figure 2-9 also shows that there is a small level of asymmetric distribution of the relative nonlinear parameter in the FE results. It is mainly due to the fact that the size and shape of the elements in this region of the FE model are similar but they are not perfectly the same.

While loading the specimen to initiate the fatigue crack in cyclic test, the specimen undergoes material degradation, e.g., loss of stiffness and dislocation of grains [33],[52]. This can induce the material nonlinearity and cause a slight difference between the FE calculated and the experimentally measured directivity patterns as the FE simulations do not take into account the material nonlinearity. As this study does not follow the phase and group velocity requirement, the higher harmonics generated by the material nonlinearity are not accumulated, i.e. decay with the wave propagation distance. Hence, the higher harmonics generated by the material nonlinearity is minimized in this study. Overall, the comparison between the FE simulation and experimental results show that the FE simulation is able to provide a reasonable prediction of the higher harmonic generation at the fatigue crack by the low frequency Lamb wave.

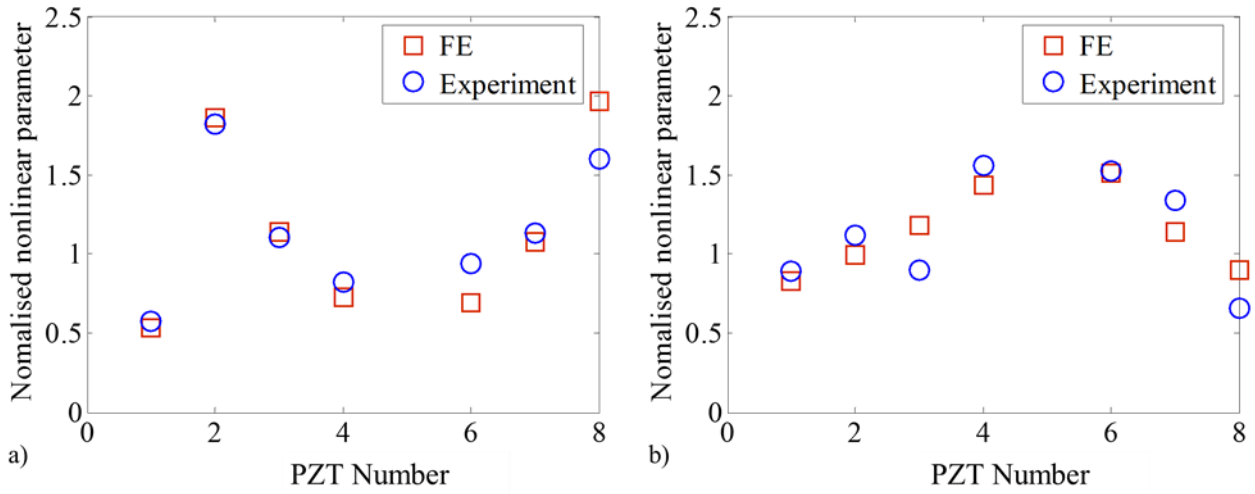

Figure 2-9: FE simulated and experimentally measured normalized relative nonlinear parameter at a) 240kHz (S0 Lamb wave); and b) 160kHz (S0 and A0 mixed Lamb wave)

2.5. Parametric study

2.5.1. Effect of varying crack length

In this section, the experimentally verified FE model is used to study the second harmonic generation measured at different sensors for different crack lengths using 240kHz S_0 incident Lamb wave. In addition to the eight transducers, i.e. PZT1-PZT8, as shown in Figure 2-2, an additional transducer is added at r = 80mm and θ = 180° to act as the actuator. As shown in Figure 2-3b, only the fatigue crack was modeled in the FE simulation, i.e. without the through hole and the starter notches. The simulation duration is 5.2μs, which only covers the incident

Lamb wave propagates from the actuator to the fatigue crack, and then, the generated second harmonic Lamb wave propagates from the fatigue crack to the sensors. In this section the relative nonlinear parameter β_C' is normalized to the value obtained from the corresponding sensors at intact state (β_{C0}').

As shown in Figure 2-10, only the normalized relative nonlinear parameter obtained at PZT1 (0°) grows linearly with fatigue crack length to incident wave wavelength ratio. For other sensors, the increase of the magnitude of the normalized relative nonlinear parameters is slower than the results of PZT1, especially for PZT3 (90°) and PZT7 (270°). At PZT2 (45°), PZT4 (135°), PZT6 (225°) and PZT8 (315°), the normalized relative nonlinear parameter decreases when the fatigue crack length to incident wave wavelength ratio increases beyond 0.3. The results demonstrate the importance of designing the transducer network, as the damage information might be misinterpreted or overlooked for sensors at some particular locations.

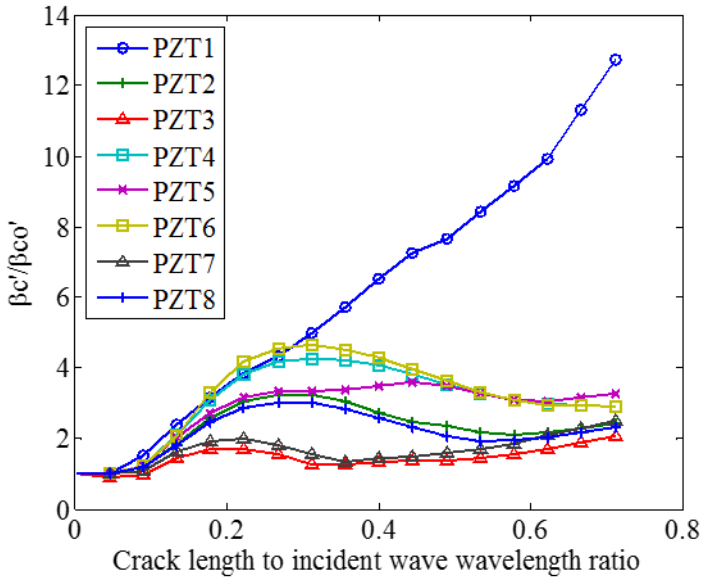

Figure 2-10: Normalized relative nonlinear parameter as a function of fatigue crack length to incident wave wavelength ratio

The directivity patterns of the normalized relative nonlinear parameters for cracks with length equals to 4mm, 8mm, 12mm and 16mm are shown in Figure 2-11. The directivity patterns indicate that the magnitude of the normalized relative nonlinear parameter mainly concentrates in forward and backward scattering directions of the second harmonic Lamb wave. Meanwhile,

as the crack length increases, the magnitude of the second harmonic Lamb wave is dominated in the direction at θ = 0° and 180°.

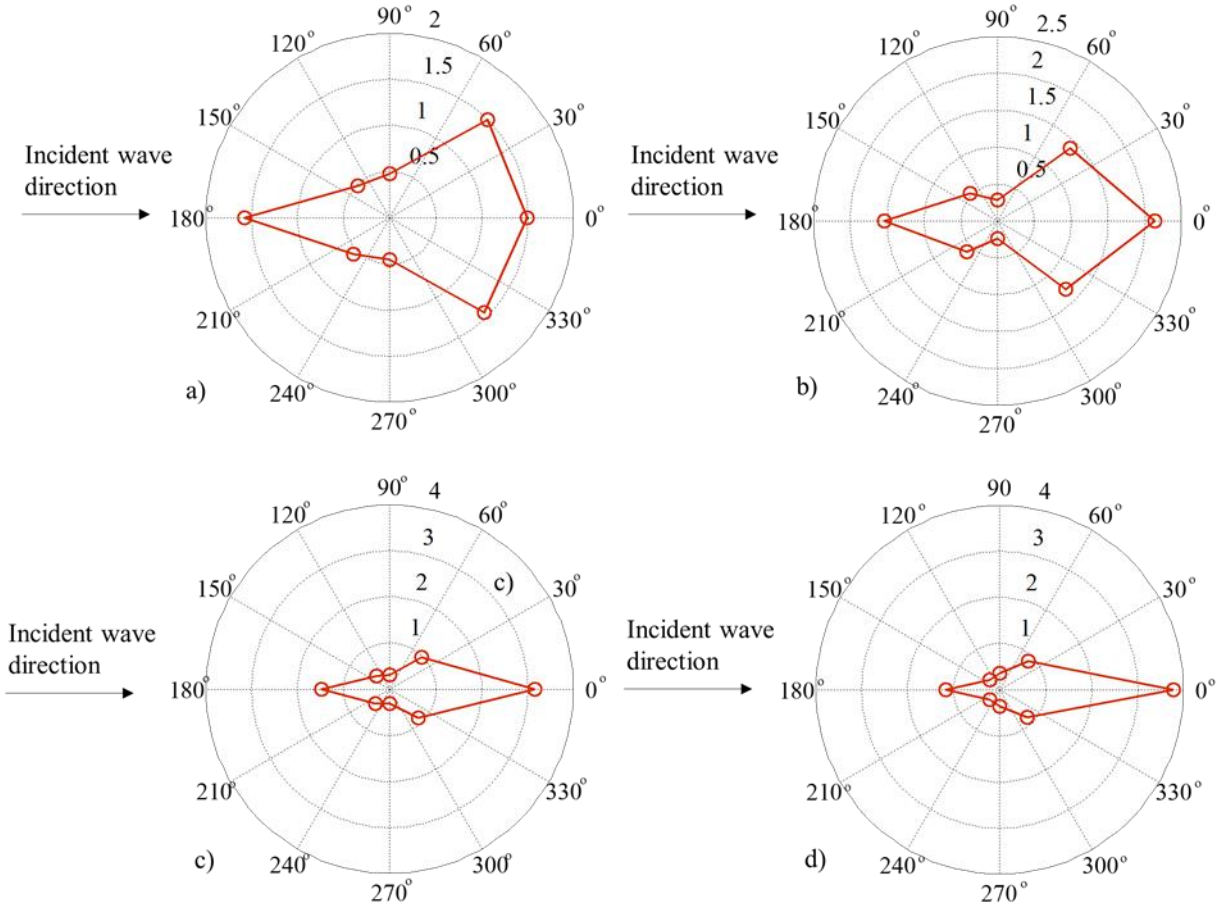

Figure 2-11: Directivity pattern of normalized relative nonlinear parameters for a) 4mm; b) 8mm; c) 12mm; and d) 16mm long fatigue crack

2.5.2. Effect of varying excitation frequency

The other parametric study was carried out by varying excitation frequency and the results are shown in Figure 2-12. The frequency is varied from 200kHz to 400kHz, in which the amplitude of S_0 incident Lamb wave is higher than that of the A_0 incident Lamb wave based on the mode-tuning curve as shown in Figure 2-5. The crack length is fixed at 8mm. Without loss of generality, the results are presented in terms of fatigue crack length to incident wave wavelength ratio. It is found that the variation of β_C' has a similar trend to the variation of the ratio of S_0 to A_0 incident Lamb wave amplitude. For most of the transducers, except transducers at 45° (PZT2) and 315° (PZT8), the value of β_C' reaches the maximum when fatigue crack length to incident wave wavelength ratio equals to 0.371, which is corresponding to the

excitation frequency of 250 kHz. At this frequency, the ratio of S_0 to A_0 incident Lamb wave amplitude becomes about maximum as shown in Figure 2-5. For the transducers at 45° and 315°, β_C' reach its maximum value when the fatigue crack length to incident wave wavelength ratio equals to 0.447 (300kHz), and this frequency is close to the frequency, 280kHz, at which the S_0 incident Lamb wave becomes maximum at this frequency as shown in Figure 2-5. The results again illustrate that larger magnitude of the S_0 incident wave tends to generate larger magnitude of second harmonic at the fatigue crack. The directivity pattern of β_C' is also investigated and they are shown in Figure 2-13. In general, the directivity patterns show that the amplitude of β_C' in the forward scattering direction has relative larger magnitude compared to other directions.

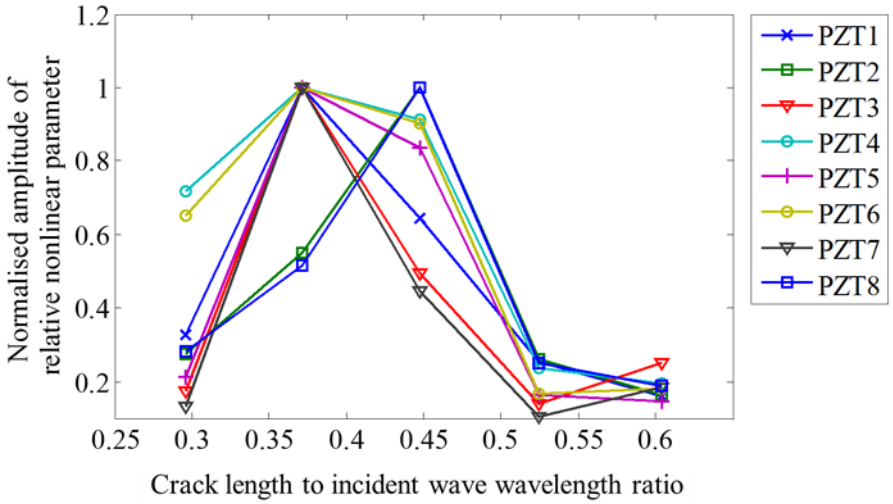

Figure 2-12: Variation of normalized relative nonlinear parameter against the crack length to incident wave wavelength ratio

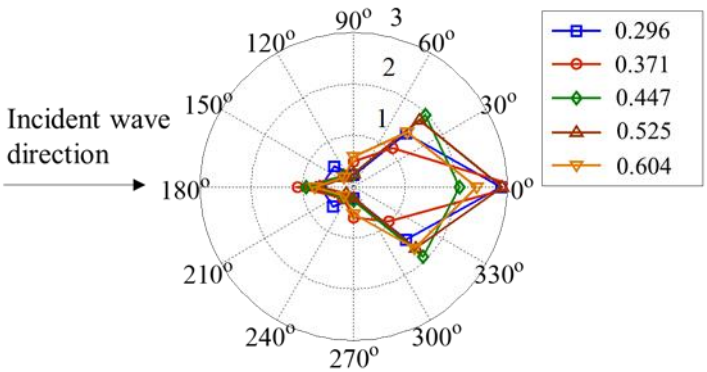

Figure 2-13: Directivity patterns of normalized relative nonlinear parameters at different crack length to incident wave wavelength ratios

2.6. Conclusions

The study has investigated the second harmonic generation due to S_0 dominated, A_0 dominated, and S_0 and A_0 mixed incident Lamb wave interaction with the fatigue crack. In the experimental study, the results have shown that the S_0 dominated incident wave is more sensitive to the fatigue crack compared to the A_0 dominated, S_0 and A_0 mixed incident Lamb wave. In the numerical study, the piezoceramic actuator and sensor model have been implemented in the 3D FE simulations and there has been good agreement between the numerical and experimental results for the linear Lamb wave signal and the directivity pattern of the second harmonic generation. This has proved that the FE is not only capable of modeling the linear Lamb wave propagation, but also the directivity pattern of the second harmonic generation due to the contact nonlinearity at the fatigue crack.

The results of the parametric study have shown that the magnitude of the second harmonic Lamb wave induced at the fatigue crack is dominant in the forward and backward scattering direction. In addition, the magnitude of the second harmonic Lamb wave in the forward scattering direction increases with the crack length to incident wave wavelength ratio at a higher rate compared to other directions. It is also found that S_0 Lamb wave has the dominant effect on second harmonic generation at the fatigue crack. Overall, this study has gained physical insights into the generation of the second harmonic due to the contact nonlinearity at a fatigue crack. The findings of this study help to further advance the use of the second harmonic Lamb wave for damage detection.

Acknowledgement

This work was supported by the Australian Research Council (ARC) under Grant Numbers DP160102233 and DE130100261. The supports are greatly appreciated.

References

[1] Rose LJ 2002 *J. Press. Vess. Tech.* **124** 273-282.

[2] Giurgiutiu V, Bao J 2004 *Struct. Health Monitor.* **3** 121-140.

[3] Aryan P, Kotousov A, Ng CT, Cazzolato B 2017 *Struct. Cont. Health Monitor.* **24** 1-13.

[4] Diamanti K, Soutis C 2010 Progress in Aerospace Sci. **46** 342-352.

[5] Giridhara G, Rathod VT, Naik S, Mahapatra DR, Gopalakrishnan S 2010 Mech. Syst. Sig. Process. **24** 2929-2946.

[6] An YK, Sohn H 2012 *Mech. Syst. Sig. Process.* **30** 157-167.

[7] Ng CT 2014 *Eng. Struct.* **67** 50-60

[8] Wandowski T, Malinowski PH, Ostachowicz WM 2016 *Mech. Syst. Sig. Process.* **66-67** 248-267.

[9] He S, Ng CT 2016 *Eng. Struct.* **127** 602-614.

[10] He S, Ng CT 2015 *Elec. J. Stuct. Eng.* **14** 20-32.

[11] Moreau L, Velichko A, Wilcox PD 2012 *NDT&E Inter.* **45** 46-54.

[12] Casadei F, Rimoli JJ, Ruzzene M 2014 *Finite Elem. Analy Design* **88** 1-15.

[13] Ng CT 2015 *Inter. J. Struct. Stab. Dyn.* **15** 1540010.

[14] Ng CT 2015 *Earthquake & Struct.* **8** 821-841.

[15] Carandente R, Lovstad A, Cawley P 2012 *NDT&E Inter.* **52** 57-68.

[16] Soleimanpour R, Ng CT 2016 *J. Civil Struct. Health Monitor.* **6** 447-459.

[17] He S, Ng CT 2017 *Mech. Syst. Sig. Process.* **84** 324-345.

[18] Zhu X, Rizzo P, Marzani A, Bruck J 2010 *Meas. Sci. Technol.* **21** 045701.

[19] An YK, Sohn H 2010 *Struct. Health Monitor.* **17** 730-741.

[20] Marzani A, Salamone S 2012 *Mech. Syst. Sig. Process*. **30** 204-217.

[21] Aryan P, Kotousov A, Ng C.T, Wildy S 2016 *Smart Mater. Struct.* **25** 035018.

[22] Mohabuth M, Kotousov A, Ng CT 2016 *Inter. J. Non-linear Mech.* **86** 104-111.

[23] Bermes C, Kim JY, Qu J, Jacobs LJ 2008 *Mech. Syst. Sig. Process.* **22** 638-646.

[24] Solodov I, Wacker J, Pfleiderer K, Busse G 2004 Appl. Phys. Lett. **84** 5386-5388.

[25] Aymerich F, Staszewski WJ 2010 *Struct. Health Monitor.* **9** 541-553.

[26] Lim HJ, Sohn H 2015 *J. App. Phy.* **118** 244902.

[27] Van Den Abeele KEA, Carmeliet J, Ten Cate JA, Johnson PA 2000 *J Res. Nondestruct. Eval.* **12** 31-42.

[28] Cantrell JH, Yost WT 2001 *Int. J. Fatigue* **23** 487-490.

[29] Barnard DJ, Dace GE, Buck O 1997 *J. Nondestr Eval.* **16** 67-75.

[30] Biwa S, Hiraiwa S, Matsumoto E 2006 *Ultrasonics* **44** e1319-e1322.

[31] Matlack KH, Kim JY, Jacobs LJ, Qu J 2015 *J. Nondestr Eval.* **273** 1-23.

[32] Jhang, KY 2009 *Inter. J. Precision Eng. Manu.* **10** 123-135.

[33] Pruell C, Kim JY, Qu J, Jacobs LJ 2009 *NDT&E Inter.* **42** 199-203.

[34] Shen Y, Giurgiutiu V 2014 *J. Intel. Mater. Syst. Struct.* **25** 506-520.

[35] Soleimanpour R, Ng CT 2017 *Eng. Struct.* **131** 207-219.

[36] Li W, Cho Y, Achenbach JD 2012 *Smart Mater. Struct.* **21** 085019.

[37] Zhou C, Hong M, Su Z, Wang Q, Cheng L 2013 *Smart Mater. Struct.* **22** 015018.

[38] Chillara VK, Lissenden CJ 2016 *Optical Eng.* **55** 011002.

[39] Soleimanpour R, Ng CT 2016 *Struct. Health. Monitor.* doi:10.1177/1475921716673021.

[40] Yelve NP, Mitra M, Mujumdar PM 2017 *Comp. Struct.* **159** 257-266.

[41] Nucera C, Lanza di Scalea F 2011 *Struct. Health Monitor.* **10** 617-629.

[42] Lee B, Staszewski W 2003 *Smart Mater. Struct.* **12** 804-814.

[43] Gopalakrishnan S, Chakraborty A, Mahapatra D 2007 *Spectral finite element method, wave propagation, diagnostics and control in anisotropic and inhomogeneous Structures* (London: Springer Science & Business media).

[44] Ostachowicz W, Kudela P, Krawczuk M, Zak A 2011 *Guided waves in structures for SHM: the time-domain spectral element method* (Chichester: John Wiley & Sons).

[45] Kudela P, Ostachowicz W 2009 J. Phys.: Conference series **181** 012091.

[46] Lin X, Yuan FG 2001 *Smart Mater. Struct.* **10** 907-913.

[47] Su Z, Ye L 2005 *J. Intel. Mater. Syst. Struct.* **16** 97-111.

[48] Blau PJ 2009 *Friction Science and Technology* (Boca Raton: CRC Press).

[49] Sohn H, Lee SJ 2010 *Smart Mater. Struc.* **19** 015007.

[50] Yelve N, Mitra M, Mujumdar P 2014 *Struct. Control Health Monit.* **21** 833-846.

[51] Lee TH, Jhang KY 2009 *NDT&E Inter*. **42** 757-764.

[52] Codrington J, Kotousov A 2007 *Inter J. Fracture.* **144** 285-295.

Chapter 3. Influence of Crack Opening and Incident Wave Angle on Second Harmonic Generation of Lamb Waves

(Paper 2, Published)

Yi Yang[a], Ching-Tai Ng[a], Andrei Kotousov[b]

[a] School of Civil, Environmental and Mining Engineering, The University of Adelaide, Adelaide, SA 5005, Australia

[b] School of Mechanical Engineering, The University of Adelaide, Adelaide, SA 5005, Australia

Publication:

Yang Y, Ng CT, Kotousov A 2018 *Smart Mater & Struct* **27**(5) 055013

Statement of Authorship

Title of Paper	Influence of crack opening and incident wave angle on second harmonic generation of Lamb waves
Publication Status	☑ Published ☐ Accepted for Publication ☐ Submitted for Publication ☐ Unpublished and Unsubmitted work written in manuscript style
Publication Details	Yang, Y., Ng, C., & Kotousov, A. (2018). Influence of crack opening and incident wave angle on second harmonic generation of Lamb waves. *Smart Materials and Structures*, 27(5) 055013

Principal Author

Name of Principal Author (Candidate)	Yi Yang
Contribution to the Paper	Undertook literature review, designed experimental tests and developed numerical models, performed data processing and prepared manuscript
Overall percentage (%)	80%
Certification:	This paper reports on original research I conducted during the period of my Higher Degree by Research candidature and is not subject to any obligations or contractual agreements with a third party that would constrain its inclusion in this thesis. I am the primary author of this paper.
Signature	Date 11/01/2019

Co-Author Contributions

By signing the Statement of Authorship, each author certifies that:

i. the candidate's stated contribution to the publication is accurate (as detailed above);

ii. permission is granted for the candidate in include the publication in the thesis; and

iii. the sum of all co-author contributions is equal to 100% less the candidate's stated contribution.

Name of Co-Author	Ching-Tai Ng
Contribution to the Paper	Helped experiments and model development, helped review manuscript and prepare for submission, and acted as corresponding author
Signature	Date 11/1/2019

Name of Co-Author	Andrei Kotousov
Contribution to the Paper	Helped evaluate and edit the manuscript.
Signature	Date 4/1/2019

Please cut and paste additional co-author panels here as required.

Abstract

Techniques utilising second harmonic generation (SHG) have proven its great potential in detecting contact-type damage. However, the gap between the practical applications and laboratory studies is still quite large. The current work is aimed to bridge this gap by investigating the effects of the applied load and incident wave angle on the detectability of fatigue cracks of various lengths. Both effects are critical for practical implementations of these techniques. The present experimental study supported by three-dimensional (3D) finite element (FE) modelling has demonstrated that the applied load, which changes the crack opening and, subsequently, the contact nonlinearity, significantly affects the amplitude of the second harmonic generated by the symmetric mode (S_0) of Lamb waves. This amplitude is also dependent on the length of the fatigue crack as well as the incident wave angle. The experimental and FE results correlate very well, so the modelling approach can be implemented for practical design of damage monitoring systems as well as for the evaluation of the severity of the fatigue cracks.

Keywords: second harmonic, nonlinear Lamb wave, contact nonlinearity, applied load, incident wave angle, fatigue crack, crack opening

3.1. Introduction

3.1.1. Lamb waves for damage detection

In the last few decades, damage detection techniques utilising guided waves [1], [2] have attracted significant attention due to its advantages over the conventional non-destructive inspection methods [3], [4]. These advantages include the ability to monitor large areas, including inaccessible locations, with a small number of inexpensive piezoelectric sensors, which can be permanently attached to the structure for continuous measurements [5], [6]. Several damage detection methods utilising either linear or nonlinear characteristics of Lamb wave propagation have been proposed in the past [7]. Most of these methods, however, are based on the linear features of Lamb waves e.g. methods utilising analysis of reflection and transmission signals [8], [9] and time-of-flight [10], [11] as well as the mode conversion phenomena [12], [13]. However, these linear methods are only capable to detect mechanical damage (e.g. fatigue cracks, delaminations and corrosion spots) with the characteristic sizes of the same order of the magnitude as the wavelength of the incident wave. However, the

wavelength of the incident wave cannot be too small in practical applications as the high frequency (corresponding to short wavelengths) normally generates multiple propagating wave modes, which can make the signal acquisition and analysis very challenging. In addition, the damage detection methods, which rely on the linear characteristics or phenomena of Lamb wave propagation, usually require reference or baseline data in order to extract the residual signal, which correspond to the material damage. However, it has been shown in the literature that the baseline signal can be strongly affected by the change of environmental and loading conditions leading to a significant degradation in damage sensitivity of linear methods [9, 14]. The latter is the main reason why the methods, which perfectly work in laboratory conditions, fail to deliver the similar performance in the real-world environment.

In contrast, nonlinear features of Lamb wave are much more sensitive to incipient damage to the early state of material degradation [15]. In addition, the damage detection techniques utilising nonlinear features of Lamb wave propagation do not require the reference or baseline data (signal) to detect damage [16]. Therefore, the nonlinear methods could have a better performance and fewer limitations than their linear counterparts in the real-world environment. Recently, a number of studies attempted to apply various nonlinear features of Lamb wave propagation for damage detection, for example, higher harmonic generation phenomenon [16], [17], sidebands generation [18]-[20], and nonlinear resonance effects [21], [22]. The present paper is focused on the second harmonic generation (SHG) phenomenon for the contact-type damage detection, which will be briefly discussed next.

3.1.2. Second harmonic generation (SHG)

A distortion of the excitation wave by the clapping mechanism, which will be described below, leads to the generation of higher harmonics. During this process the wave energy from the frequency of the incident wave pumps into the second or even higher order harmonics. The process can be governed by the global material nonlinearity [15], [17], [23], or local damage-induced nonlinearity [24]-[26]. One of the local nonlinearity effects, contact nonlinearity [27], has recently gained an increasing attention. It is associated with contact-type damages, such as a fatigue crack, delamination or debonding. The present study is concerned with the contact nonlinearity due to fatigue cracks. It manifests itself when an incident wave of sufficiently large enough amplitude interacts with a so-called “breathing crack”, which behaves like a “mechanical diode”. The compressional part of the wave closes the crack (or a section of the

crack) while the tensile part tends to open the crack or its section (as fatigue cracks are normally closed due to plasticity effects near the crack tip and the wake of plasticity due to crack fatigue growth). This nonlinear phenomenon leads to the generation of a number of higher harmonics and sub-harmonics as a result of parametric modulation, which can be used for the detection and characterisation of the fatigue crack. Below we also provide a brief overview of the selected studies related to the contact nonlinearity and SHG.

Most of the simple and popular analytical approaches to model the contact nonlinearity and clapping mechanism are based on bi-linear stiffness approximation. When the crack is open, the global stiffness is reduced; when the crack is closed, the stiffness has its nominal value. Many studies in the past have utilised this approach and were able to reproduce the generation of the second and higher order harmonics.

There were many studies in the past on SHG caused by contact nonlinearity [28]-[30], however, most of them were focused on bulk waves. For example, Biwa *et al*. [31] investigated the SHG of a longitudinal wave at the contact interface of two aluminium blocks. It was demonstrated that an increase of the contact pressure at the interface leads to the reduction of the magnitude of the second harmonic. It means that the SHG depends on the magnitude of the contact pressure, therefore, justifies the objectives of the current study. Lee and Jhang [32] investigated the SHG due to presence of fatigue cracks in an aluminium sample, using an ultrasonic wave scanning technique. A relative nonlinear parameter was utilised for the evaluation of the contact nonlinearity and avoid the effect of other nonlinearities associated with the equipment and material behaviour.

Hong *et al*. [17] examined the synchronising characteristics of high frequency Lamb wave interactions with a fatigue crack. However, investigations of the nonlinear phenomena at high frequencies need quite sophisticated equipment, instrumentation and signal processing due to the dispersive nature of Lamb waves at high frequencies. Recently, Yang *et al*. [33] investigated the SHG due to the presence of fatigue cracks using low frequency symmetric and anti-symmetric modes of Lamb waves. It appears that the fundamental symmetric mode (S_0) is more promising for monitoring and evaluation of fatigue damage. Subsequently, the present study is focused on relatively low frequencies, which generate only the fundamental modes of Lamb waves, and, in particular, on the S_0, which is much less dispersive than the fundamental anti-symmetric fundamental mode (A_0) of Lamb wave.

Most previous experimental and numerical studies simply ignored the effect of the applied load on the SHG. However, in many practical applications the applied loading cannot be avoided and it can change the crack opening, and hence, alter the contact conditions (contact nonlinearity) at the crack surfaces. For example, Lim *et al*. [34] demonstrated that the crack opening has a large effect on the magnitude of the SHG. Therefore, for practical applications the evaluation of the effect of the applied load on the magnitude of the SHG is essential. For this reason, it is also included as one of the objectives in the current study. Along with the mechanical phenomena, this work is also focused on the development of numerical approach for the evaluation of SHG and modelling the wave interactions and the effect of the applied loading. This is motivated by the practical considerations, where a pure experimental approach is unrealistic for the design of a fatigue crack monitoring and evaluation system. It is believed that numerical approaches will play a leading role in the development and design of damage monitoring systems, and provide much more efficient solutions to practical challenges.

The primary objective of this study is to improve the understanding of the SHG of Lamb waves due to presence of fatigue cracks under realistic conditions with a focus on the practical implementation of this technique for in-situ monitoring. The current study investigates the influence of the crack opening due to the applied loading and the incident wave angle on the SHG induced by the nonlinear interaction of fatigue cracks of various lengths with the S_0 Lamb waves.

The article is arranged as follows. A detailed description of the experimental set-up is presented in Section 2, which includes the details of the specimen preparation procedures, signal generation methods, data acquisition system. Section 3 describes the finite element (FE) modelling approach, which is used to support the experimental studies. In Section 4, the frequency selection criteria based on the mode tuning studies are outlined. The experimental results and validation of the FE model are provided in Section 5. This section also presents the results of a parametric study utilising the experimentally verified three-dimensional (3D) FE modelling approach. Finally, main conclusions of the research outcomes are presented in Section 6.

3.2. Experimental setup

This section first outlines the details of the specimen fabrication procedures, specifically the generation of fatigue cracks. The experimental setup for the excitation and sensing the Lamb waves is also described in this section.

3.2.1. Experiment specimen

A 5005-H34 aluminium plate was cut into a dog-bone shape specimen as shown in Figure 3.1a. The in-plane dimensions of the specimen are 400mm×300mm and the thickness is 3mm. The material properties of the plate are given in Table 3.1. Piezoceramic discs (Ferroperm Pz27) with 10mm diameter and 0.5mm thickness were permanently bonded to the surface of the plate specimen by a conductive epoxy. The material properties of the piezoceramic discs are also listed in Table 3.2. The piezoceramic discs were used to form a circular transducer network with radius R = 40mm as shown in Figure 3.1a. A polar coordinate system is set at the centre of the plate. Based on this reference system, all eight piezoceramic discs were located at r = 40mm and $0^o \pounds q \pounds 315^o$ with 45^o interval. In this study, one of the piezoceramic discs was used to actuate the Lamb waves while the rest of the piezoceramic discs were used to sense the Lamb wave signals.

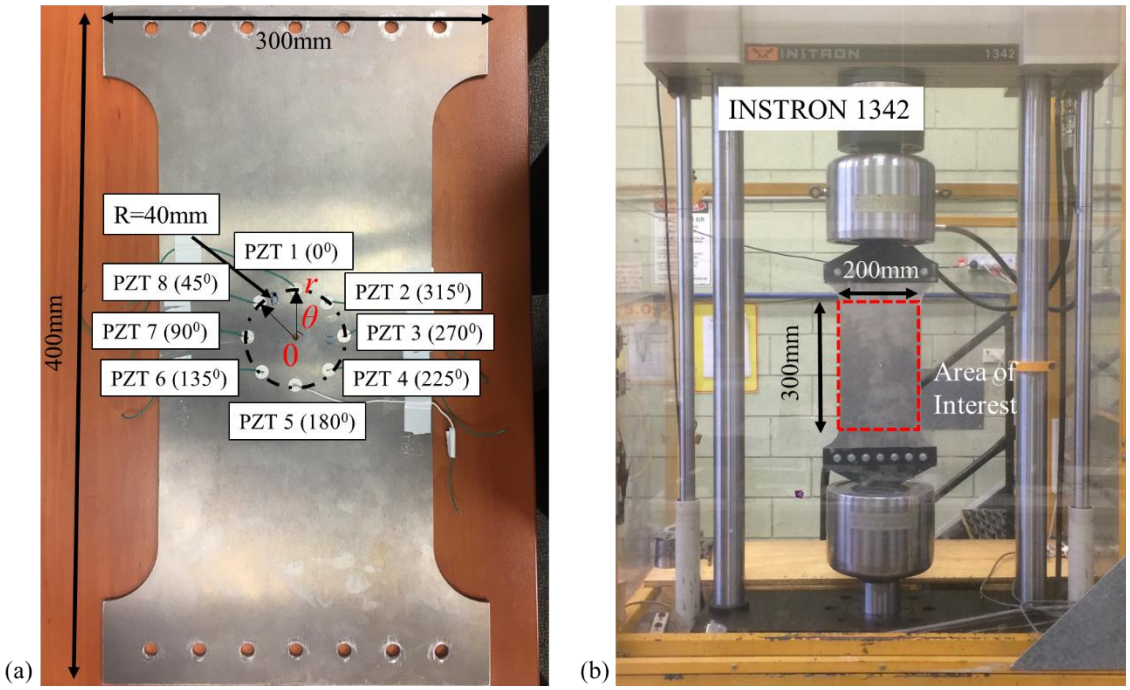

Figure 3-1: (a) Aluminium plate with installed piezoceramic discs and (b) cyclic loading equipment and area of interest in the specimen.

Table 3-1: Material properties of the 5005-H34 aluminium plate

Young's Modulus (GPa)	69.5
Poisson Ratio	0.33
Density (kg/m^3)	2700

Table 3-2: Material properties of the Ferroperm Pz27 Piezoceramic discs

Young's Modulus (GPa)	59
Poisson Ratio	0.389
Density (kg/m^3)	7700
Relative Dielectric Constant	1800
Piezoelectric Charge Constant (m/V)	170×10^{-12}
Permeability (F/M)	8.854×10^{-12}

3.2.2. Fatigue crack generation

Fatigue cracks in the aluminium sample were generated as follow. A 5mm circular through hole was first drilled at the centre of the aluminium plate to facilitate the fatigue crack initiation. Two 1mm long starter notches were cut using a 0.5mm thick saw blade in the directions $q = 90°$ and 270° referring to the polar coordinate system as shown in Figure 3.1a. The plate was then loaded cyclically under a 10Hz sinusoidal tensile load with a minimum force of 5kN and a maximum force of 30kN, as shown in Figure 3.1b. A fatigue crack was initiated and observed at each starter notch after 250,000 cycles. The SHG tests were performed after every 100,000 cycles. Both cracks grew to about 8mm after 800,000 cycles, which corresponds to, so called, Paris fatigue crack growth regime.

3.2.3. Actuating and sensing Lamb waves

A computer controlled signal generator (NI PIX-5412) was used to generate the excitation signals. The excitation signal is a narrow-band eight-cycle sinusoidal tone burst pulse modulated by a Hanning window. A typical excitation signal has a peak-to-peak output voltage of 10V. The signal was amplified by 5 times using an amplifier (KROHN-HITE 7500) before

it was sent to one of the transducers bonded on the plate sample, while the rest of the transducers were used to receive and measure the wave signal. The signals were digitized by a data acquisition system (NI PXIe-5105) and then fed into a computer. The quality and repeatability of the measurements were improved by averaging the signals with 64 acquisitions.

In this study, the measured time duration was limited to 50μs. This ensured that the recorded signals cover only the Lamb waves travelling within the area as highlighted in Figure 3.1(b), and hence, it (the time duration) avoids the effect of the plate clamps on SHG. In practice, there are always presence of non-damage related nonlinearities, e.g. material nonlinearity of the plate, inherent nonlinearity of electrical equipment, the material coupling between transducers and surface of the plate, and background noise, etc. To avoid the contribution of these nonlinearities into the observed SHG, the wave signals were generated and measured for the intact plate (before cycling loading); and these data were used as a benchmark to ensure that the measured (during the fatigue tests) nonlinearity represents the contact nonlinearity and not the non-damage related nonlinearities.

3.3. Three-dimensional finite element model

A 3D FE model was created using commercial FE software, ABAQUS, to support the numerical study. Figure 3.2 shows schematic diagrams of the FE model including the through hole, starter notches, fatigue cracks and transducer models. The dimension of the aluminium model is 300mm×200mm, which is the same as the area of interest for the plate sample in the experiment as shown in Figure 3.2b. The thickness of the aluminium plate model is 3mm, which also replicates the specimen. The piezoceramic discs were modelled based on the piezoelectric theory [35], [36]. According to the theory, the radial displacement on the circumference of the actuator in FE model is linearly related to the voltage applied in the experiment, and thus in FE model the excitation can be modelled by applying a radial displacement on the circumference of the PZT model. For the sensor model, the strain at the centre of the PZT is linearly related to the received voltage, so the output from the FE model can be obtained as the strain from the middle of the PZT model. In the FE model, it is assumed that the piezoceramic discs are perfectly bonded to the aluminium plate. The material properties of the plate and piezoceramic disc model are the same as the specimen in the experiment.

Eight-noded brick elements, C3D8I, in which each node has three translational degrees-of-freedom (DoFs), were used to model both the aluminium plate and the piezoceramic discs. The

in-plane dimension and the thickness of the elements are around 0.4mm×0.4mm and 0.375mm, and hence, there at least 20 elements per wavelength for the incident Lamb wave and the induced second harmonic wave. There are eight layers of elements in the thickness direction of the aluminium plate. The aspect ratio of the solid elements is 1.07. An intact plate is also modelled to ensure that the second harmonic obtained from the FE model with the damage is generated from fatigue crack. To model the experimental condition of the specimens, a 5mm diameter circular through-hole and two 1mm×1mm starter notches were modelled by removing elements for both intact and damaged plates. For the damaged plate, the fatigue crack was simulated by inserting a seam at both end of each starter notch. The crack was arranged in vertical direction as shown in Figure 3.2b. It is worth noticing that the model is meshed automatically in ABAQUS, the meshes around the through hole and notch are not perfectly symmetric about the centre of the model, and the meshes of PZT models are also not perfectly the same. As a result, the wave signal obtained at the symmetric PZT pairs about the incident wave propagation direction is not exactly the same, though the differences are subtle as will be shown in the *Results and Discussions* section.

The hard normal contact and frictional tangential contact were applied to the interfaces of the seam crack to prevent nodes penetration, and hence, simulating the clapping of the crack interfaces when the Lamb waves propagate through the fatigue cracks. An increased value of the friction coefficient of 1.5 [37] was used to account for the increased friction due to the roughness of the actual crack surfaces, crack tip plasticity and plasticity–induced crack closure effects associated with fatigue crack propagation. This value was found empirically as the best fit to the experimental data. The transient problem was solved using the explicit FE code, ABAQUS/Explicit, which employs the explicit central different integration scheme to calculate the response of the wave propagation.

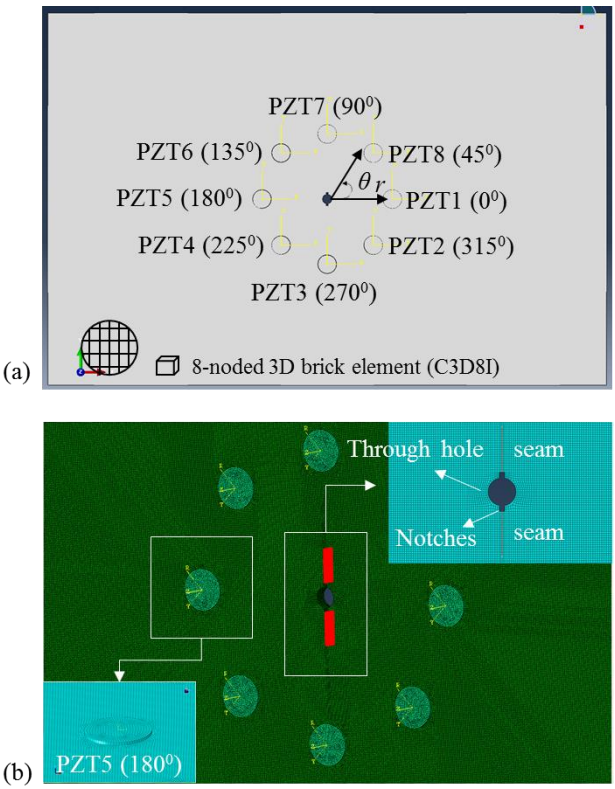

Figure 3-2: Schematic diagram of (a) the finite element model, and (b) the model of the fatigue cracks and piezoceramic transducer.

3.4. Lamb wave mode tuning procedure

In the beginning of the experimental study, mode tuning experiments [38], [39] were carried out to determine the excitation frequency that could generate S_0 dominated signal. The S_0 Lamb wave is selected as the incident wave in this study as this mode is more sensitive to the fatigue crack than the A_0 Lamb wave [33]. This was briefly discussed in the Introduction section. In the low frequency region, both S_0 and A_0 Lamb wave are normally excited simultaneously. Thus, a pair of the piezoceramic discs were attached to the surface of a larger aluminium plate (1m×1m) with the same material properties and thickness as the plate used in the fatigue test. The narrow-band sinusoidal tone burst pulse modulated by a Hanning window was applied to one of the piezoceramic discs to generate the dominant S_0 Lamb wave mode. The excitation frequency was swept from 10kHz to 400kHz. At the same time, the other piezoceramic discs were used to measure the Lamb wave signals. At each excitation frequency, the amplitude ratio of S_0 to A_0 Lamb wave were recorded. Figure 3.3 shows the Lamb wave mode tuning results. According to the results, the maximum amplitude ratio of the S_0 to A_0 Lamb waves is at 240kHz. Therefore, the excitation frequency of 240kHz was chosen to excite the S_0 dominated Lamb

wave in the experimental studies. From the current results, the maximum amplitude ratio of the S_0 to A_0 Lamb waves is at 240kHz. Although the thickness and material properties of the specimen are slightly different, the optimal frequency obtained in the current study is comparable to the results from the previous study [38], where it was found to be between 230kHz and 330kHz.

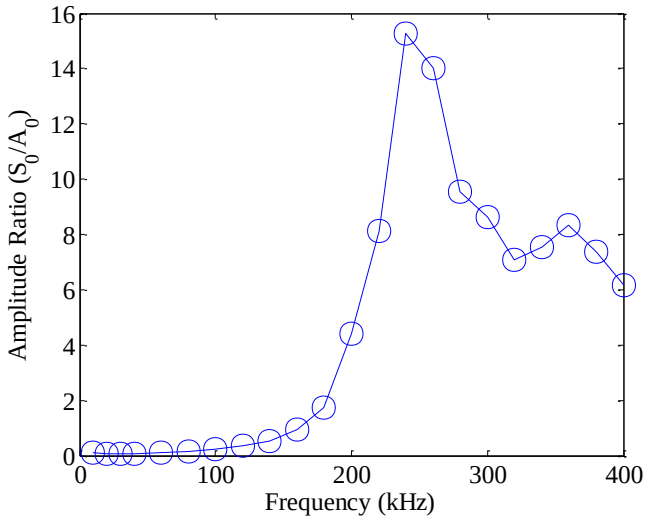

Figure 3-3: Ratio of S_0 to A_0 Lamb wave amplitude excited on the aluminium plate using a 10mm diameter and 0.5mm thick Ferroperm Pz27 piezoceramic disc.

3.5. Results and discussion

The influence of the incident wave angle and crack opening due to the applied load on the SHG due to presence of fatigue cracks was investigated using experimental and the 3D FE modelling approaches. The accuracy of the FE model in predicting the SHG was validated by comparing the simulation results with the experimental data. The experimentally validated 3D FE model is then used to obtain directivity patterns of the SHG with the consideration of different incident wave angles and crack openings due to the applied load.

For the current study, the focus is on revealing the potential influence of the incident wave angle and external loads on the features of SHG, so only one sample specimen is used. To practically apply the method in damage detection, it is recommended to verify the repeatability of the measured signal with some calibration to compensate the variation of nonlinear parameter because of the possible differences in crack profile different from every set of fatigue loading test, and the differences in the bonding conditions of transducers.

3.5.1. Second harmonic generation (SHG) at the fatigue crack

Short Time Fourier Transform (STFT) was used to transform all of the acquired time series data to the time-frequency domain because it is easier to distinguish the first arrival wave signals from the boundary reflections. The spectrogram parameters in the STFT were carefully selected by a series of trials to ensure the balance between time and frequency resolution.

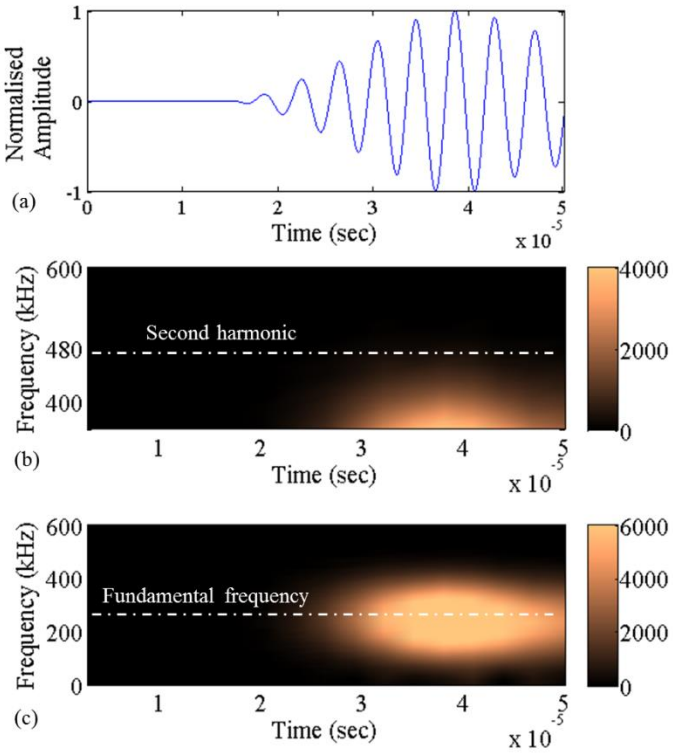

Figure 3-4: Spectrogram of the FE results for PZT1 with 240kHz excitation frequency for an intact model, (a) time domain signal, (b) second harmonic frequency range, and (c) incident wave frequency range.

Figure 3.4 shows the spectrogram of the Lamb wave signal captured at PZT1 in the FE simulation for an intact model. An incident wave with a large displacement magnitude (100μm) is used to provide a better illustration of the wave distortion due to contact nonlinearity at the fatigue cracks. As shown in Figure 3.4b, there is no visible energy at the second harmonic frequency (double of the excitation frequency). While for the damaged plate, i.e. a model with an 8mm fatigue crack at each of the starter notch (hole), the time-domain signal as shown in Figure 3.5a is distorted as compared with the intact plate (Figure 3.4a), especially for the tensile part of the wave. As shown in the spectrogram in Figures 3.5b and 3.5c, it is clear that the wave energy is transmitted from the fundamental frequency to second harmonic frequency when the

fatigue crack presents in the model. For the intact plate (Figure 3.4b), the second harmonic is negligible as compared with the result of the damaged plate as shown in Figure 3.5b. In contrast, in experimental studies, the second harmonic might be not negligible for the intact plate as it can also be generated from the coupling between the transducers and host plate, signal generator and data acquisition system.

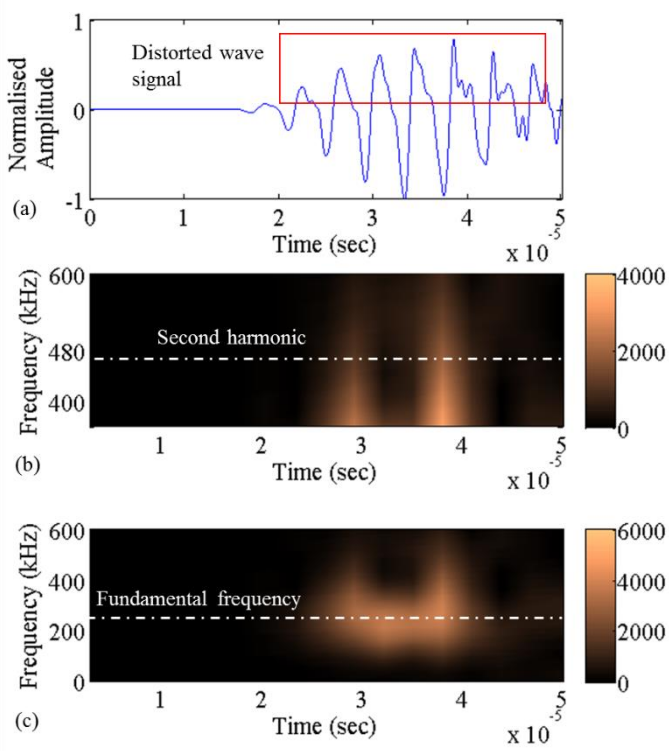

Figure 3-5: Spectrogram of FE results for PZT1 240kHz excitation frequency for the model with fatigue cracks, (a) time domain signal, (b) second harmonic frequency range, and (c) incident wave frequency range.

The experimental amplitude profile of the spectrogram at 240kHz and 480kHz were extracted for the intact and damaged plate. The results are normalized by the maximum value of the wave signal at the fundamental frequency. The group velocities of the S_0 Lamb wave at these two frequencies are almost the same. Figures 3.6 and 3.7 show the amplitude profile of the signal at the excitation frequency and second harmonic frequency for intact and damaged plate, respectively. In these figures, the arrival time of the wave signal is marked using a vertical dashed line. The arrival time of the wave pulse at the excitation frequency is the incident wave propagates directly from the actuator to the sensor. In practice, the second harmonic wave also exists in the intact specimen due to different factors, such as nonlinearity of the equipment and

material nonlinearity of the specimens in the experiment. The second harmonic wave due to the aforementioned non-damage related nonlinearities should arrive at the same time as the wave pulse at the excitation frequency and this agrees with the results as shown in Figure 3.6.

Figure 3.7 displays that the magnitude of the second harmonic is higher than that in Figure 3.6 (intact sample). Figure 3.7 also shows that the second harmonic wave due to the contact nonlinearity in the damaged sample arrives after the incident wave at the excitation frequency for PZT2, PZT3 and PZT4. This is due to the fact that the arrival time of the second harmonic wave is the time of the incident wave propagates from the actuator to the fatigue crack, and then the induced second harmonic wave propagates from the fatigue crack to the sensor. Since this wave path is longer than the direct wave path between the actuator and sensor of the incident wave at the excitation frequency, there is a time delay between the arrival times of the wave at the excitation frequency and second harmonic frequency. For PZT1, as the crack is on the direct wave path of the wave propagation direction, the second harmonic and excited wave arrive almost at the same time.

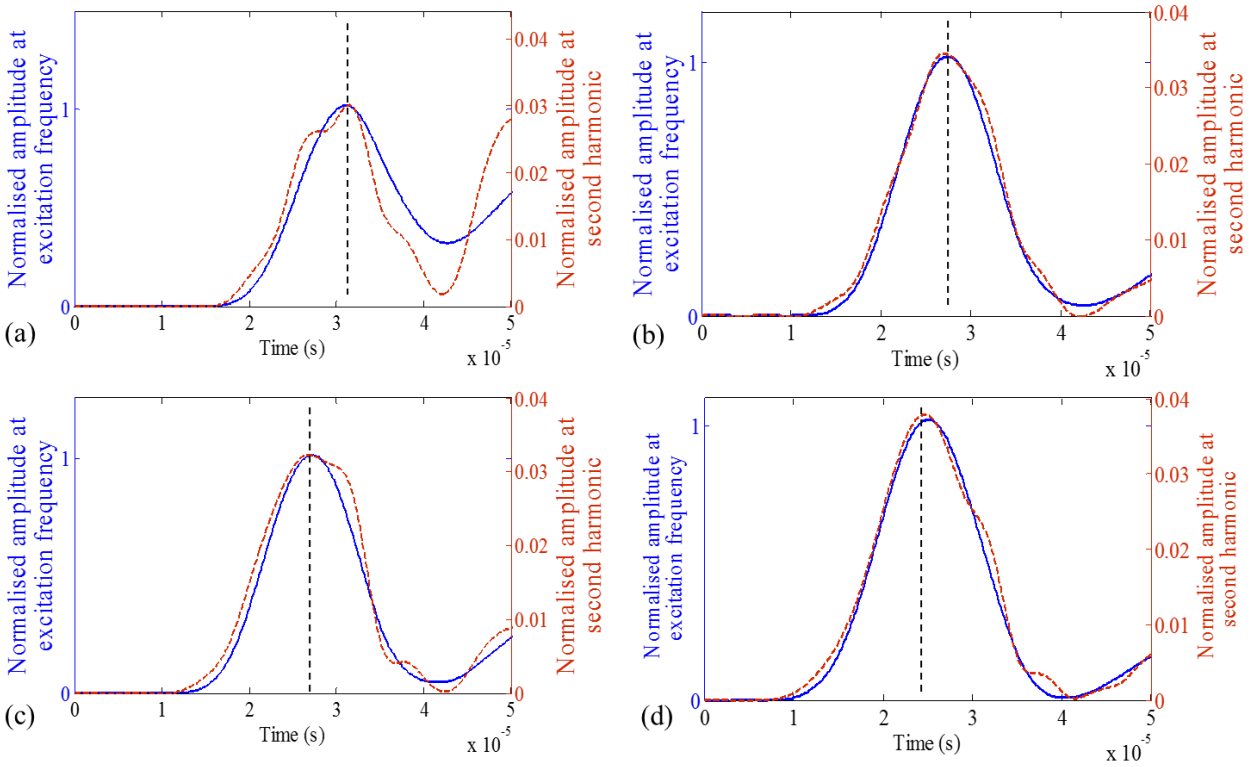

Figure 3-6: Experimentally measured amplitude profile at excitation frequency (blue solid lines) and second harmonic frequency (red dashed lines) for the intact plate, data measured by (a) PZT1, (b) PZT2, (c) PZT3 and (d) PZT4.

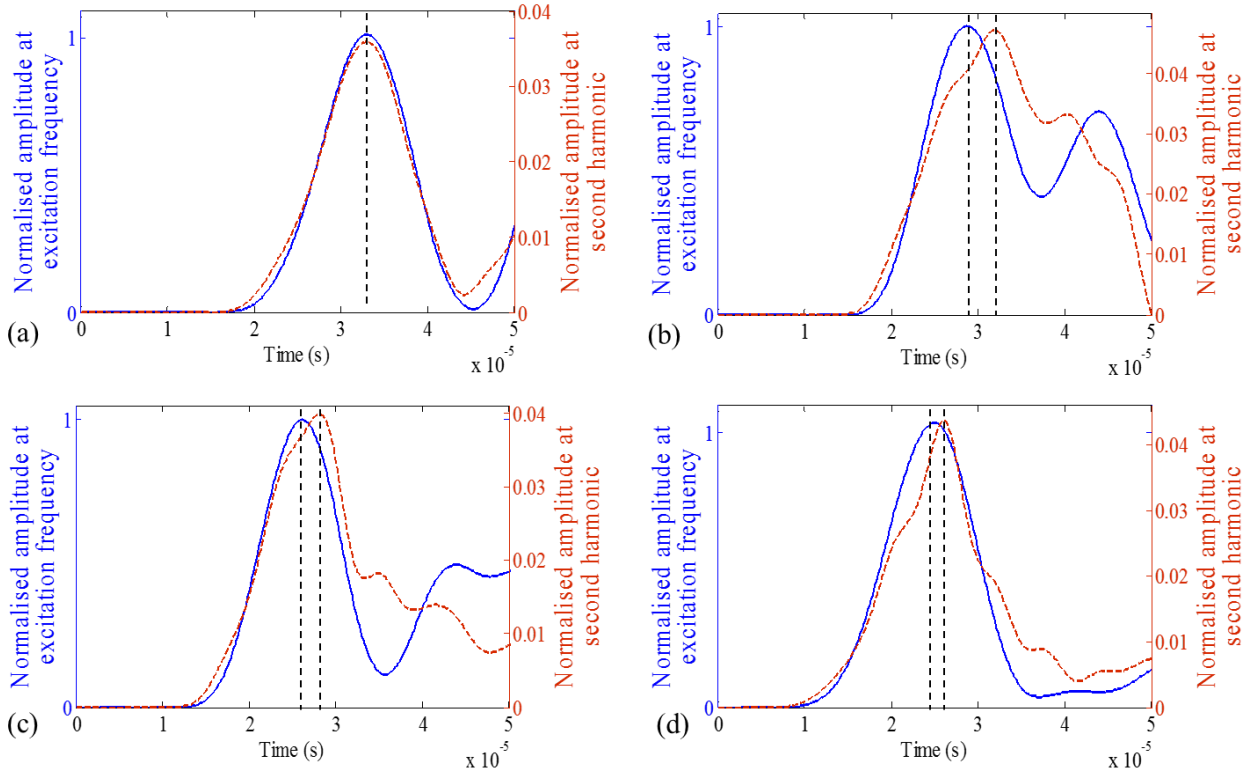

Figure 3-7: Experimentally measured amplitude profile at excitation frequency (blue solid lines) and second harmonic (red dashed lines) after 800,000 cycles of loading, data measured by (a) PZT1, (b) PZT2, (c) PZT3 and (d) PZT4.

3.5.2. Relative second order nonlinear parameter

In this study, the results are presented using the normalized relative second order parameter $\overline{\beta}'$, [32, 33] which is defined as β' normalized by the mean of β' obtained from all the cases considered in each study. Thus, β' is defined as

$$\beta' = \frac{A_2}{A_1^2} \tag{3.1}$$

where A_2 is the amplitude of the first peak of the amplitude profile at the second harmonic frequency (red dashed lines in Figures 3.6 and 3.7) obtained by STFT in Section 5.1, and A_1 is the first peak of the amplitude profile at the excitation frequency (solid lines in Figures 3.6 and 3.7).

3.5.3. Effects of the incident wave angle on the second harmonic generation (SHG)

In practical situation, the crack orientation may be different with respect to the incident wave, thus, leading to different types of the wave-crack interaction, such as opening-closing, tearing and sliding motions [20]. In the first part of this section, the variations of $\overline{\beta}'$ against crack lengths with three different incident angles are discussed together with the outcomes of the FE simulations and experimental results.

The incident wave angles considered in this study are 90°, 45° and 0° corresponding to the incident waves generated by PZT3, PZT4 and PZT5, respectively. The experimentally measured and numerically calculated $\overline{\beta}'$ for the above incident wave angles are shown in Figures 3.8, 3.9, and 3.10, respectively. To ensure the consistency of the obtained $\overline{\beta}'$, the results of each pair of transducers, which are located symmetrically about the incident wave angle and crack orientation, are both shown in Figures 3.8, 3.9 and 3.10. For 90^o incident wave angle (Figure 3.8), the transducer pairs are PZT2 and PZT4, PZT1 and PZT5, and PZT6 and PZT8. For 0^o incident wave angle (Figure 3.10), the transducer pairs are PZT4 and PZT6, PZT3 and PZT7, and PZT2 and PZT8.

As shown in Figures 3.8 and 3.10, i.e. the results of incident wave angle 90^o and 0^o, respectively, the variation of $\overline{\beta}'$ for the results of each transducer pair is very similar to each other. This is because the crack profile, i.e., the size and shape, at both sides of the through hole are also symmetric about the incident wave angle. Also, the magnitudes of the stresses induced by the applied cyclic load at both sides of the through hole are similar given the symmetric configuration of the plate and through hole with starter notches. Although these aforementioned conditions were used in the FE simulations, a very small discrepancy is observed between the results of the two transducers in each transducer pair as illustrated in Figures 3.8 and 3.10. This is because the meshing of the FE model is not perfectly symmetric about the incident wave angle and crack orientation.

The experimental results represented by the solid lines in Figures 3.8 and 3.10 also demonstrate a good agreement between the symmetric transducer pairs. However, as expected, it (the agreement) is not as good as that in the numerical simulations. This is because the fatigue cracks at both sides of the through hole are not initiated simultaneously and, generally speaking, do not propagate symmetrically. Also, the unavoidable eccentricity of the applied load in the experiment may also cause the non-symmetric stress distribution in the plate. All these factors

were the contributors to the discrepancies between the experimental studies with symmetric transducer pairs and differences between the experimental and FE results.

For 45^o incident wave angle (Figure 3.9), although the transducer pairs of PZT3 and PZT5, PZT2 and PZT6, and PZT1 and PZT7 are located symmetrically about the incident wave angle, they are not located symmetrically about the crack orientation. The results between the transducers of each transducer pair behave quite differently due to the violation of the symmetric condition.

Overall, for the experimental and numerical results shown in Figures 3.8, 3.9 and 3.10 are in a good agreement in terms of the variation pattern of parameter $\overline{\beta}'$. The results for 90^o incident wave angle show a better agreement with the FE results than the results of the other two incident wave angles. For the incident wave angle is 0^o (Figure 3.10), the value of $\overline{\beta}'$ has a clear growing trend at all transducers; and the growth is more significant at PZT1, PZT2 and PZT8, i.e. the forward scattering directions. This means that under this condition, sensors in any direction are able to provide a warning signal for the presence of fatigue crack. However, for the cases of incident wave angle 90^o (Figure 3.8) and 45^o (Figure 3.9), $\overline{\beta}'$ only increases slightly with crack length to incident wave wavelength ratio and then stays about the same magnitude at most of the sensors. While noticeably for PZT2, 4 of the 90^o case and PZT3, 5 of the 45^o case, the nonlinear parameter even shows decreasing trend when the crack length to incident wavelength ratio increases. The results show that the incident wave angle plays a vital role in SHG and thus it is important to use a transducer network in a damage detection system and conduct measurements considering all the incident wave angle cases to precisely predict the health condition of the structure.

Based on the results presented in Figures 3.8, 3.9 and 3.10, $\overline{\beta}'$ has different characteristics for different crack length to incident wave wavelength ratios. This means that these characteristics can be potentially used for quantitative damage identification. However, the variations of $\overline{\beta}'$ under different incident angle conditions are very different to each other. This means that the wave-crack interaction characteristic highly depends on incident wave angle. Therefore, it is essential to take into account the incident wave angle if it is used for quantitative damage identification.

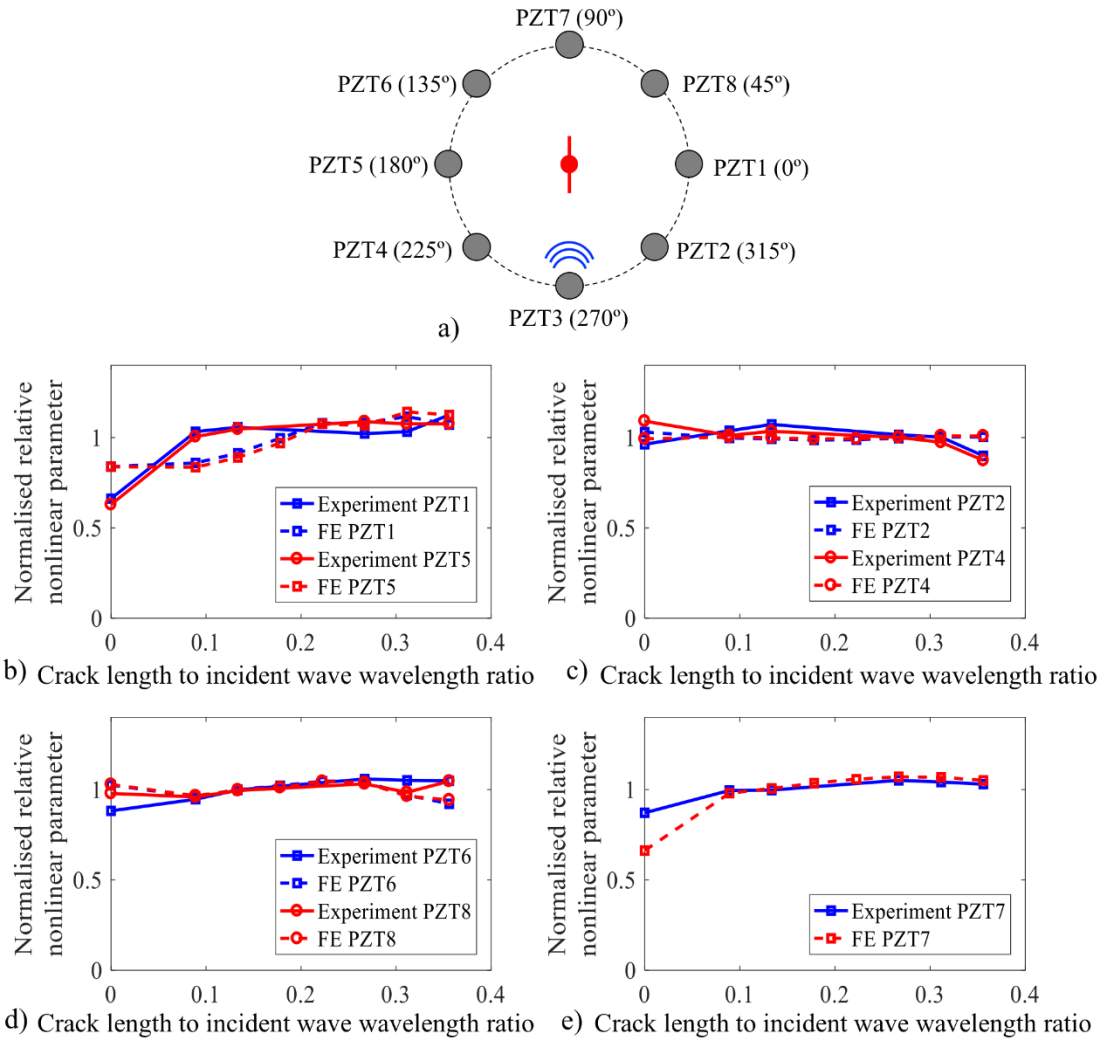

Figure 3-8: a) Schematical diagram of the transducer arrangement for incident wave angle 90° case, b)-e) normalized relative second order nonlinear parameter $\overline{\beta}'$ as a function of crack length to incident wave wavelength ratio at different PZTs

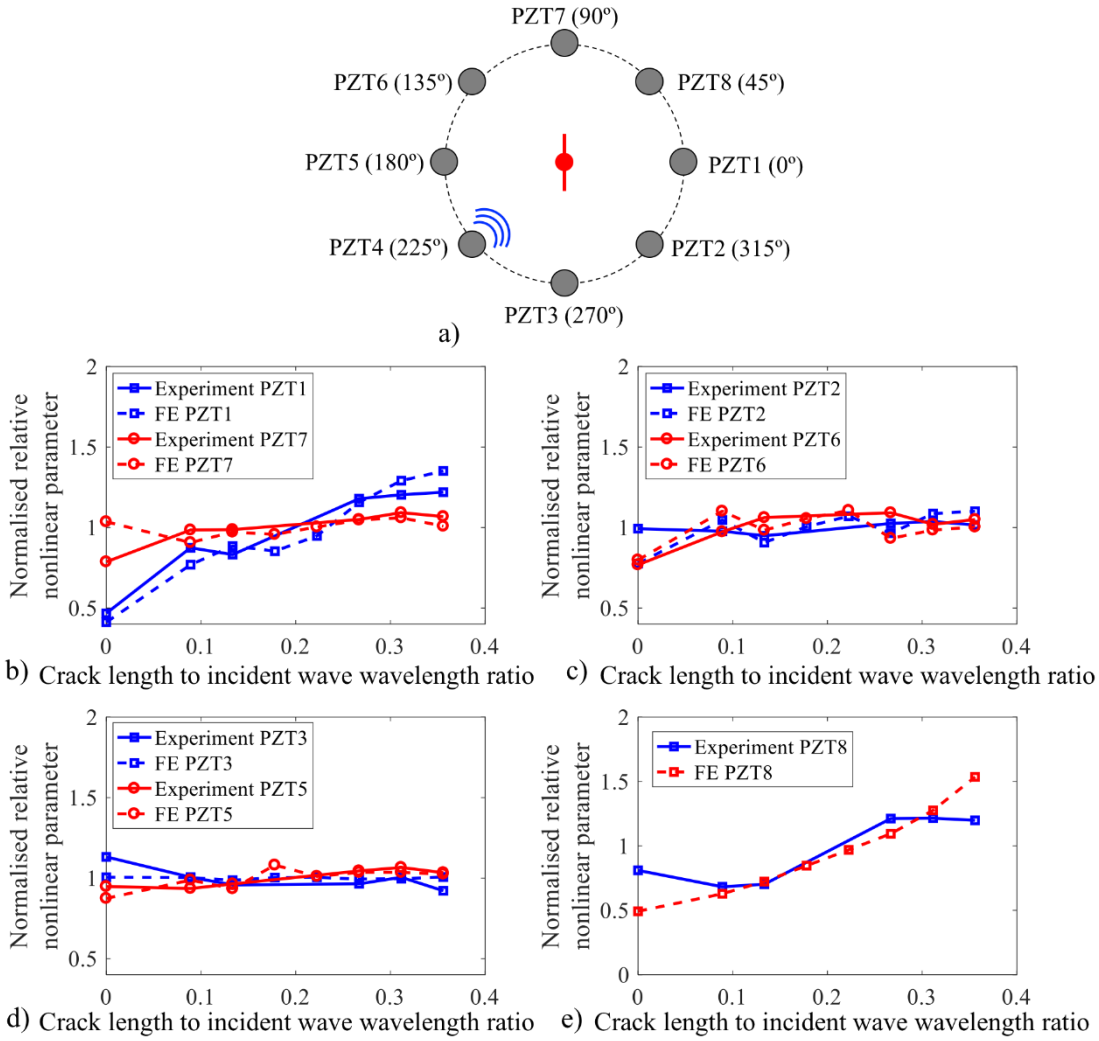

Figure 3-9: a) Schematical diagram of the transducer arrangement for incident wave angle 45° case, b)-e) normalized relative second order nonlinear parameter $\overline{\beta}'$ as a function of crack length to incident wave wavelength ratio at different PZTs

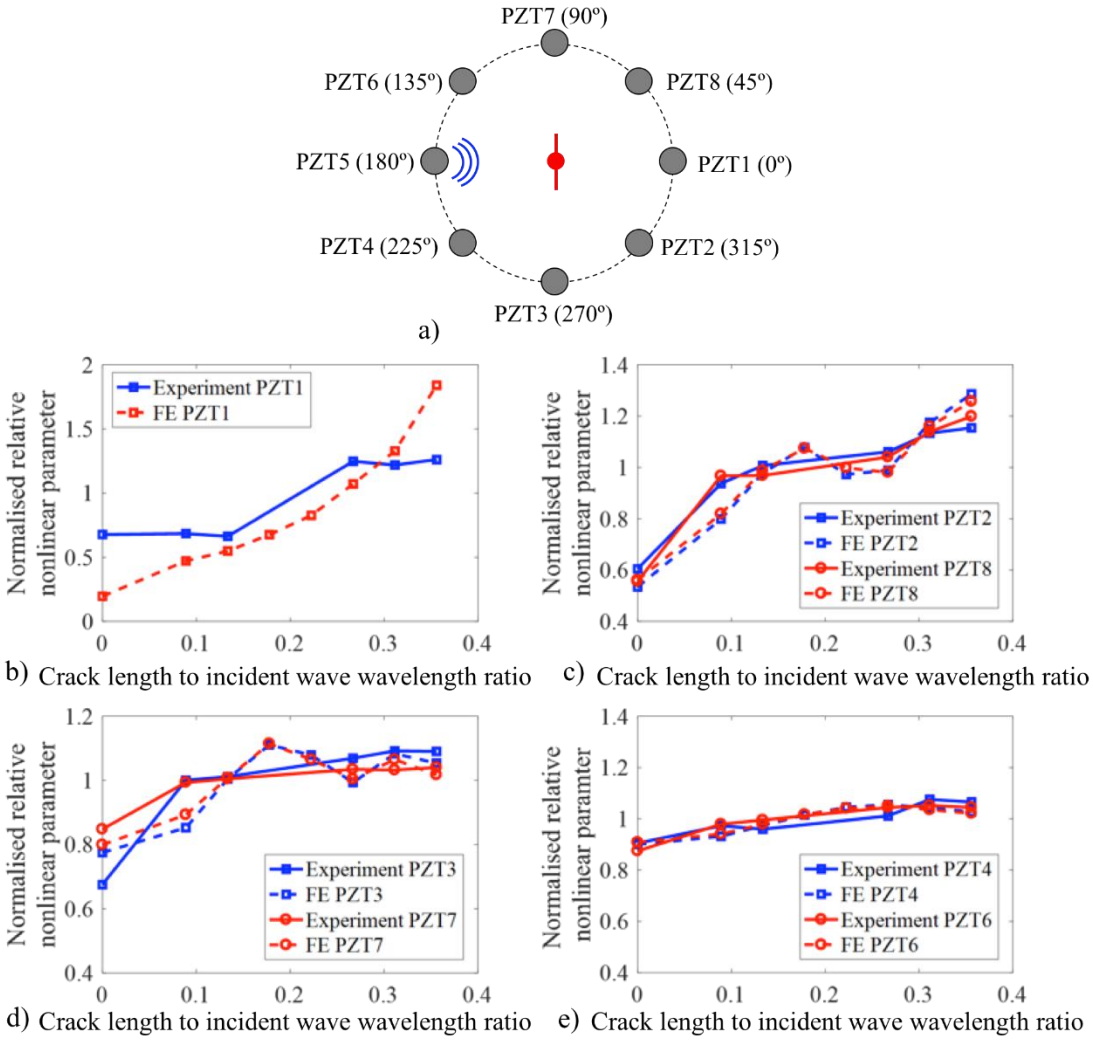

Figure 3-10: a) Schematical diagram of the transducer arrangement for incident wave angle 0° case, b)-e) normalized relative second order nonlinear parameter $\overline{\beta}'$ as a function of crack length to incident wave wavelength ratio at different PZTs

3.5.4. Second harmonic generation (SHG) at fatigue crack with different crack openings

The other issue that needs to be considered for practical application of the nonlinear Lamb wave method is that, the structure is usually subjected to changing loading conditions. These conditions can change the crack opening or the gap between the surfaces of the fatigue cracks as shown in Figure 3.11, and hence, it changes the properties of the contact nonlinearity. In this section, the influence of the crack opening due to the applied loading is studied experimentally. The FE model is also adopted to support the experimental study and analyse the trends of $\overline{\beta}'$ as a function of the applied tensile stress.

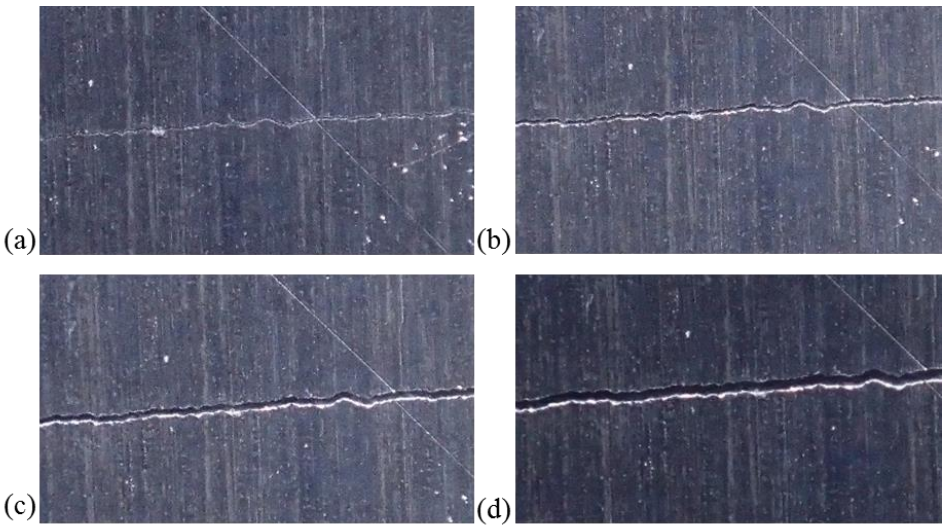

Figure 3-11: Crack opening under (a) 25MPa, (b) 50MPa, (c) 75MPa and (d) 100MPa tensile stress in experiments

3.5.5. Experimental observations.

The tensile load is raised from 25MPa to 100MPa to gradually increase the opening of the fatigue cracks. There are several reasons that can cause the variation of $\overline{\beta}'$ when the crack is opened due to the tensile load.

i. When the applied tensile loading increases, the distance between the crack surfaces could grow beyond the maximum in-plane displacement of the wave. The wave cannot pass through the crack, and there is no contact the crack surfaces. Thus, only small amplitude of second harmonic can be generated at the tips of the fatigue crack [34].

ii. As the crack opens, it behaves like a notch when there is no contact nonlinearity. The value of $\overline{\beta}'$ can be dominated by the value of A_1 as only a small nonlinearity is generated at the crack tips due to plasticity. The value of A_1 is significantly affected by the scattering feature of linear Lamb waves at notch [40].

iii. The tensile load applied on the plate would change the phase and group velocity of the propagating wave [41]. As the linear wave scattering feature at notch is relevant to the wavelength [40], variation of phase velocity will change the wavelength of the Lamb waves, and hence, change the magnitude of A_1 measured at different

transducers. However, the variation of the phase velocity is usually very small and this will only cause a minor change of the magnitude of A_1.

iv. For the plate used in the experiment, the ratio between the diameter of the notch and width of the plate is 0.025. According to the equation for calculating the stress concentration factor on a finite-width plate under uniaxial loading [41], the stress concentration factor at the notch in this study is around 3. When the stress applied on the plate is greater than 75MPa, the stress at the notch is around 225MPa. Considering the yielding stress of the 5005 H34 aluminium is around 145MPa – 185MPa, the area around the notch can undergo plastic deformation, and thus, increases the plasticity driven nonlinearity [23].

Figure 3.12 shows the experimentally measured results at PZT1 to PZT4 on the plate with the open crack after 800,000 cycles of loading in the cyclic test. The results indicate that different crack openings caused by different magnitude of applied tensile loads on a damaged structure can change the magnitude of $\overline{\beta}'$. According to Figure 3.12, $\overline{\beta}'$ at PZT2 and PZT3 decreases with the magnitude of the tensile load, though the variation is comparably small. At PZT4, the value of $\overline{\beta}'$ decreases when the stress is increased from 25MPa to 50MPa. Then the value increases from 50MPa to 75MPa before it drops slightly when the load is increased to 100MPa. As compared, $\overline{\beta}'$ increases at PZT1 when the stress increases from 25MPa to 75MPa, followed by a slight fall when the load reaches 100MPa.

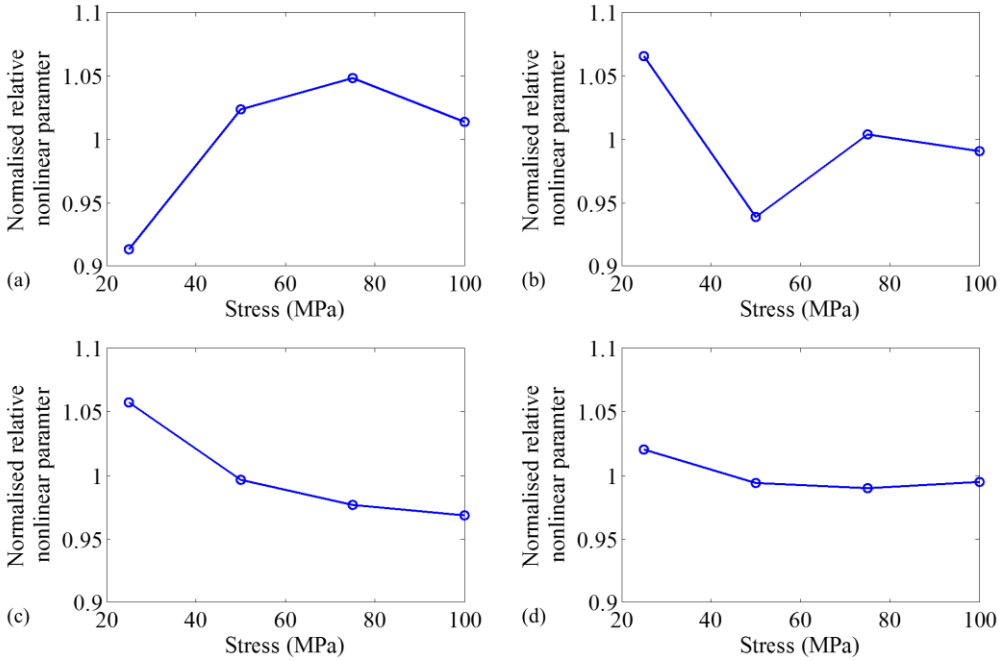

Figure 3-12: Experimentally measured normalized relative second order nonlinear parameter $\overline{\beta}'$ at (a) PZT1, (b) PZT2, (c) PZT3 and (d) PZT4 under different magnitudes of tensile stresses.

3.5.6. Effect of crack opening on contact nonlinearity due to presence of fatigue crack.

The experimentally verified FE model was used to study the effect of the crack opening on the contact nonlinearity. In this study, only the effect of crack opening variation was considered, which takes into account the first two reasons described in the Section 5.4.1 in causing the variation of $\overline{\beta}'$.

The fatigue crack in the FE simulations was opened by the applied tensile force at both ends of the plate. An example of the FE simulation snapshot of the stress distribution is shown in Figure 3.13. The results correspond to an 8mm long fatigue crack at the end of each starter notch and a 25MPa tensile stress is applied to the one end of the plate. The tensile stress with magnitudes of 8MPa, 16MPa, 25MPa, 50MPa, 75MPa and 100MPa were applied to the model. For the 25MPa stress, the maximum opening near the hole was around 9μm. When the magnitude of the tensile stress is increased to 100MPa, the opening increases to about 30μm.

The outcomes of the pre-loading steps as described above were then used to simulate the wave propagation with ABAQUS/Explicit. The maximum magnitude of the displacement applied to the actuator model was carefully controlled to ensure that the in-plane displacements of the incident wave were smaller than the smallest opening.

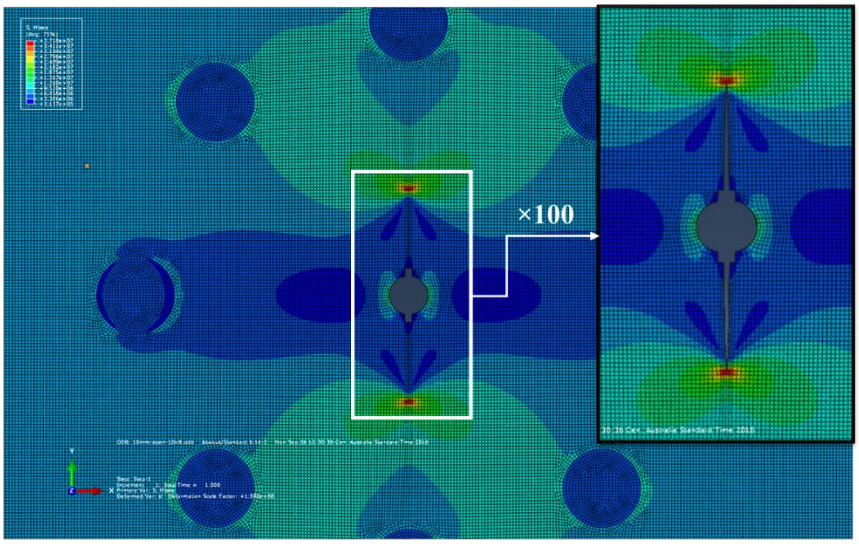

Figure 3-13: Fatigue cracks at both end of the FE plate model opened by 25MPa tensile stress and the stress distribution in the plate

As shown in Figure 3.14, for PZT1 and PZT2 there is a clear drop of the value of $\overline{\beta}'$ when the stress is increased from 8MPa to 25MPa. When the load keeps increasing, there is no clear change of the value as there is little interaction between the crack surfaces. When zooming into the variation of $\overline{\beta}'$ from 25MPa to 100MPa, a slight increase of the value is observed at PZT1, while the value at PZT2 decreases. The very small variation of $\overline{\beta}'$ can be caused by the change of scattering feature of linear Lamb waves and thus change the amplitude of A_1. In comparison, at PZT3 and PZT4, there is no distinctive variation of $\overline{\beta}'$ despite the increase of the applied tensile load.

Similar to the experimental observation, there is a distinctive cut-off point in the results of the FE simulations, beyond which there is a very small variation of $\overline{\beta}'$. In the experiments, the fatigue crack was initially open, and thus there was no sharp drop of the contact nonlinearity when the fatigue crack was pulled to reach a larger opening. For the fully opened cracks, the variation of $\overline{\beta}'$ at different PZTs was relatively larger in experimental results than in the numerical simulations. The outcomes in these two sections indicate that when the fatigue crack

is progressively opened by the applied stress (load), the variation of $\overline{\beta}'$ is mainly due to the decrease of the contact nonlinearity.

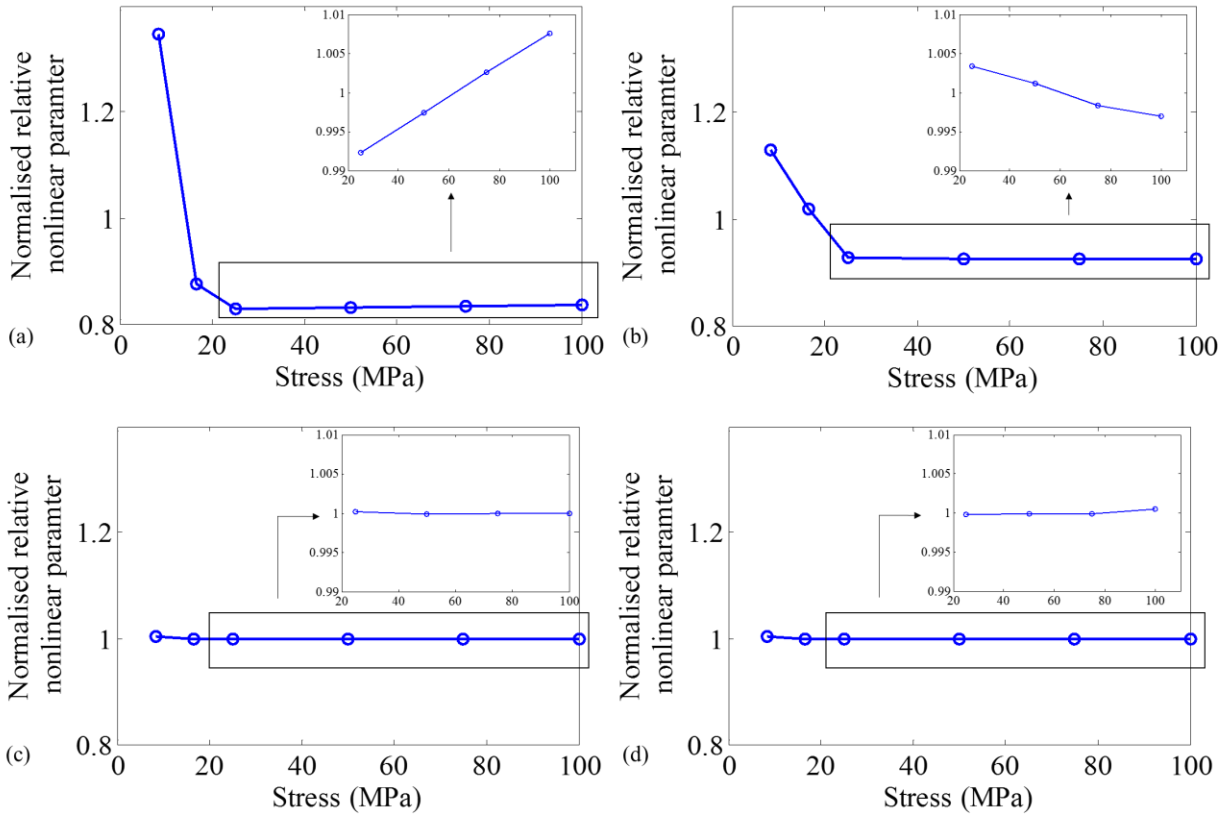

Figure 3-14: Numerically prediction of normalized relative second order nonlinear parameter $\overline{\beta}'$ at a) PZT1; b) PZT2; c) PZT3 and d) PZT4 on the plate model with different crack opening.

5.4.3 Directivity pattern of normalized relative second order nonlinear parameter predicted by FE simulations

It is of a great interest to investigate the directivity patterns of $\overline{\beta}'$ around a fatigue crack with different incident angles and crack openings, because these two factors directly related to the potential practical implementation of the SHG techniques. The experimental studies of the combined effect are costly and time-consuming. Consequently, the FE approach, which has been partially validated experimentally, was used to study the directivity pattern of $\overline{\beta}'$ at fatigue crack with different crack openings and incident wave angles. It should be noted that the

material and plasticity-driven nonlinearity were not modelled as the focus of this study is mainly on the loss of contact nonlinearity as a result of the applied loading.

In the parametric study, three additional transducers were added at θ = 180°, 135°, and 90° in the FE model and each of which is used as an actuator to generate incident wave at 0°, 315° (equivalent to 45°) and 270° (equivalent to 90°), respectively. The actuators were 70mm away from the crack, which is outside the circular transducer network. Only the fatigue crack is modelled at the centre of the plate, i.e. without the through-holes and starter notches. The maximum displacement applied to the circumference of the actuator model for generating the Lamb wave signal was 30μm.

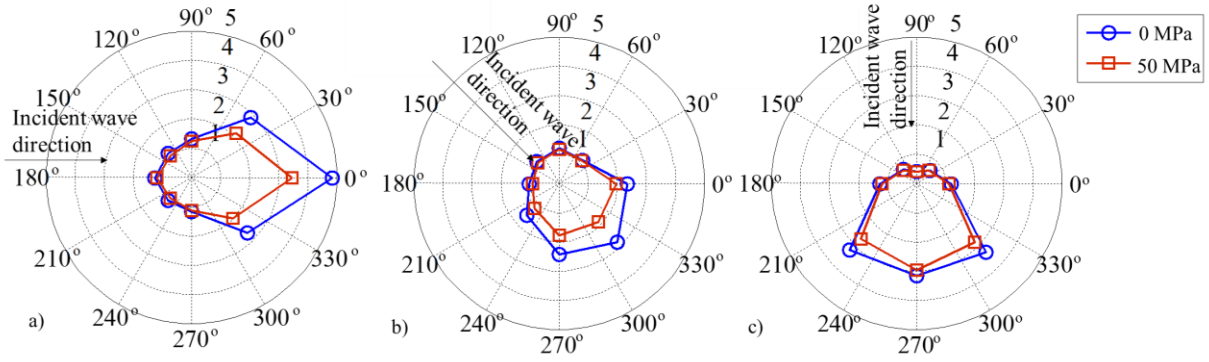

Figure 3-15: Directivity pattern of the normalized relative second order nonlinear parameter $\overline{\beta}'$ calculated by the FE simulation with a 16mm long fatigue crack opened by different applied tensile stresses, a) 0°, b) 315° (equivalent to 45°) and c) 270° (equivalent to 90°) incident wave angle.

Different to the aforementioned studies, the value of the normalized relative second order nonlinear parameter $\overline{\beta}'$ at each transducer is defined as β' normalized by the β' of this transducer obtained from the intact plate in this section. The outcomes of the simulations are shown in Figure 3.15. It can be seen that for all incident wave angles, the value of the $\overline{\beta}'$ generally shows a forward scattering pattern. However, it should be noted that for the 315° and 270° incident wave angles, the directivity patterns are slightly different to the case of 0° incident wave. The differences of the $\overline{\beta}'$ value between different angles are not as obvious as

for case of 0° incident wave angle. In all these three cases, the value of $\overline{\beta}'$ is generally smaller when the crack is opened, though the directivity patterns for each case under different loads are about the same. The results indicate that clapping contact of the fatigue crack surfaces generates a relative large magnitude of second harmonic. As $\overline{\beta}'$ is generally smaller for the 315° and 270° incident wave angles, this means that the contact nonlinearity is weaker for these two cases. Overall the results show that the tensile load reduces the interaction between the crack surfaces as compared with the fully closed crack. This conclusion is also supported by previous studies, which have been briefly reviewed in the Introduction section.

3.6. Conclusions

This paper is devoted to the SHG due to the interactions of S_0 incident Lamb wave with fatigue cracks. The study has focused on two practical aspects relevant to in-situ damage detection, i) the effect of crack opening due to applied load and ii) different incident wave angles. It was demonstrated experimentally that the 3D FE simulation is capable to predict the main tendencies of SHG due to the contact nonlinearity in the presence of fatigue cracks with different crack openings and incident wave angles.

The conducted study found that the magnitude of $\overline{\beta}'$ varies significantly with the incident wave angles even for the measured data obtained from the same transducer. The variation is caused by the change in contact nonlinearity, linear wave scattering and plasticity driven nonlinearity when the cracked sample is subjected to tensile loading. The observations from the experimental and FE results indicate that when the crack is progressively loaded, the variation of $\overline{\beta}'$ is mainly due to the loss of the contact nonlinearity. When the loading grows further, the increase of the nonlinearity can be associated with the plasticity mechanisms. From the present results, it is also found that the variation of $\overline{\beta}'$ was mainly dominated by the contact nonlinearity due to the increase of the fatigue crack length under the same applied load.

A number of case studies have been conducted using the validated FE approach to investigate the directivity patterns of $\overline{\beta}'$ under different incident wave angles and crack openings. The results show that the incident wave angles and applied loads on the plate could significantly change the SHG behaviour. It is important that these two important factors need to be taken

into consideration in the potential applications of the techniques based on SHG for in-situ damage detection of fatigue cracks.

Acknowledgements

This work was supported by the Australian Research Council (ARC) under Grant Numbers DP160102233 and DE130100261. The supports are greatly appreciated.

References

[1] Haynes C, Todd M 2015 *Mech. Syst. Sig. Process.* **54-55** 195-209

[2] He S, Ng CT 2016 *Eng. Struct.* **127** 602-14

[3] Rose JL 2002 *J. Press. Vessel. Technol.* **124** 273-82

[4] Raghavan A, Cesnik C 2007 *Shock and Vibration Digest* **39** 91-114

[5] Farrar CR, Worden K 2007 *Phil. Trans. R. Soc. A* **365** 303-15

[6] Giurgiutiu V 2015 *Structural Health Monitoring of Aerospace Composite* (Academic Press)

[7] Mitra M, Gopalakrishnan S 2016 *Smart. Mater. Struct.* **25** 053001

[8] Ng CT 2015 *Int. J. Struct. Stab. Dyn.* **15** 1540010

[9] Aryan P, Kotousov A, Ng CT, Cazzolato BS 2017 *Struct. Contr. Health Monitor.* **24** e1894

[10] Clarke T, Cawley P, Wilcox PD, Croxford AJ 2009 *IEEE Trans. Ultrason. Ferroelectr. Freq. Control* **56** 2666-78

[11] Sikdar S, Banerjee S 2016 *Compos. Struct.* **152** 568-78

[12] Zhang J, Drinkwater BW, Wilcox PD, Hunter AJ 2010 *NDT&E Int.* **43** 123-33

[13] He S and Ng CT 2017 *Mech. Syst. Sig. Process.* **84** 324-45

[14] Aryan P, Kotousov A, Ng CT, Wildy S 2016 *Smart Mater. Struct.* **25** 035018

[15] Bermes C, Kim JY, Qu J, Jacobs LJ 2008 *Mech. Syst. Sig. Process.* **22** 638-646

[16] Soleimanpour R, Ng CT 2017 *Eng. Struct.* **131** 207-19

[17] Hong M, Su Z, Wang Q, Cheng L, Qing X 2014 *Ultrasonics.* **54** 770-78

[18] Zagrai A, Donskoy D, Chudnovsky A, Golovin E 2008 *Res. Nondstruct. Eval.* **19** 104-28

[19] Yoder NC, Adams DE 2010 *Struct. Health Monitor.* **9** 257-67

[20] Klepka A, Staszewski WJ, Jenal RB, Szwedo M, Iwaniec J, Uhl T 2011 *Struct. Health Monitor.* **11** 197-211

[21] TenCate JA, Smith E, Guyer RA 2000 *Phys. Review Letter.* **85** 1020-23

[22] Chondros TG, Dimarogonas AD, Yao J 2011 *J. Sound Vib.* **239** 57–67

[23] Pruell C, Kim JY, Qu J, Jacobs LJ 2009 *NDT&E Int.* **42** 199-203

[24] Jhang KY 2009 *Int. J. Precis. Eng. Man.* **10** 123-35

[25] He S, Ng CT 2017 *Smart Mater. Struct.* **26** 085002

[26] Soleimanpour R, Ng CT, Wang CH 2017 *Struct. Health Monit.* **16** 400-17

[27] Solodov I, Krohn N, Busse G 2002 *Ultrasonics.* **40** 621-25

[28] Scarselli G, Ciampa F, Ginzburg D, Meo M 2015 *SPIE Proc. 9437* **943706**

[29] Amerini F, Meo M 2011 *Struct. Health Monitor.* **10** 659-72

[30] Kawashima K, Omote R, Ito T, Fujita H, Shima T 2002 *Ultrasonics.* **40** 611-15

[31] Biwa S, Hiraiwa S, Matsumoto E 2006 *Ultrasonics.* **44** 1319-22

[32] Lee TH, Jhang KY 2009 *NDT&E Int.* **42** 757-64

[33] Yang Y, Ng CT, Kotousov A, Sohn H, Lim HJ 2018 *Mech. Syst. Sig. Process.* **99** 760-73

[34] Lim HJ, Song B, Park B, Sohn H 2015 *NDT&E Int.* **73** 8-14

[35] Lin X, Yuan FG 2001 *Smart Mater. Struct.* **10** 907-13

[36] Su Z, Ye L 2005 *J. Intel Mater. Syst. Struct.* **16** 97-111

[37] Blau PJ 2009 *Friction Science and Technology* (Boca Raton: CRC Press).

[38] Sohn H, Lee SJ 2009 *Smart Mater. Struct.* **19** 015007

[39] Giurgiutiu V 2005 *J. Intel. Mater. Syst. Struct* **16** 291-305

[40] Lu Y, Ye L, Su Z, Yang C 2008 *NDT&E Int.* **41** 59-68

[41] Mohabuth M, Kotousov A, Ng CT 2016 *Int. J. Non-Linear Mech.* **86** 104-1

Chapter 4. Bolted Joint Integrity Monitoring Using Second Harmonic Generation of Guided Waves

(Paper 3, Published)

Yi Yang[a], Ching-Tai Ng[a], Andrei Kotousov[b]

[a] School of Civil, Environmental and Mining Engineering, The University of Adelaide, Adelaide, SA 5005, Australia

[b] School of Mechanical Engineering, The University of Adelaide, Adelaide, SA 5005, Australia

Publication:

Yang Y, Ng C, Kotousov A, 2019 *Struct. Health Monit.* **18**(1) 198-204

Statement of Authorship

Title of Paper	Second harmonic generation of guided wave at crack-induced debonding in FRP strengthened metal plates
Publication Status	☑ Published ☐ Accepted for Publication ☐ Submitted for Publication ☐ Unpublished and Unsubmitted work written in manuscript style
Publication Details	Yang, Y., Ng, C., & Kotousov, A. (2018). Second harmonic generation of guided wave at crack-induced debonding in FRP strengthened metal plates. *International Journal of Structural Stability and Dynamics*. 19(1), 1940006

Principal Author

Name of Principal Author (Candidate)	Yi Yang
Contribution to the Paper	Undertook literature review, developed numerical models, performed data processing and prepared manuscript
Overall percentage (%)	80%
Certification:	This paper reports on original research I conducted during the period of my Higher Degree by Research candidature and is not subject to any obligations or contractual agreements with a third party that would constrain its inclusion in this thesis. I am the primary author of this paper.
Signature	Date 11/01/2019

Co-Author Contributions

By signing the Statement of Authorship, each author certifies that:

i. the candidate's stated contribution to the publication is accurate (as detailed above);
ii. permission is granted for the candidate in include the publication in the thesis; and
iii. the sum of all co-author contributions is equal to 100% less the candidate's stated contribution.

Name of Co-Author	Ching-Tai Ng
Contribution to the Paper	Helped numerical model development, helped review manuscript and prepare for submission, and acted as corresponding author
Signature	Date 11/1/2019

Name of Co-Author	Andrei Kotousov
Contribution to the Paper	Helped evaluate and edit the manuscript.
Signature	Date 4/1/2019

Please cut and paste additional co-author panels here as required.

Abstract

In this study, the second harmonic generation (SHG) due to the contact nonlinearity caused by bolt loosening is studied experimentally and numerically using three-dimensional (3D) explicit finite element (FE) simulations. In particular, it is demonstrated that the magnitude of the SHG normally increases with the loosening of the bolted joint, and there is a reasonable agreement between the numerical simulations and experimental results. The FE model, which was validated against experimentally measured data, is further utilised to investigate an important practical situation when a loosened bolt is weakened by fatigue cracks located at the edge of the hole. The numerical case studies show that the contact nonlinearity and the change of the behaviour of the SHG with the tightening level are very different to the corresponding results with the fatigue cracks. This identified difference in the SHG behaviour can serve as an indicator of the bolted joint integrity, and thus to provide early warning for engineers to make decision on necessity of carrying out further safety inspections. Overall, the findings of this study provide improved physical insights into SHG for bolt loosening, which can be used to further advance damage detection techniques using nonlinear guided waves.

Keywords: Bolt loosening, guided waves, second harmonic generation, contact nonlinearity, fatigue crack, torque loss, structural health monitoring, bolted joint

4.1. Introduction

In last two decades, different non-destructive evaluation (NDE) techniques and damage detection methods **Error! Reference source not found.** have been developed and applied to etect damages, e.g., visual inspection [2], eddy current [3], thermography [4], conventional ultrasonic [5], vibration techniques [6]-[8] and guided wave technique [9],[10], etc. Among these methods, guided wave inspection has proven its advantages over the conventional NDE techniques and damage detection methods[11], such as its ability to inspect large area, capability of evaluating inaccessible structural components in structures, high sensitivity to small damages, and potential to develop online structural health monitoring (SHM) system through transducer network.

4.1.1. Guided waves for damage detection

Guided waves have attracted significant research interest due to its ability to propagate in different types of structures, such as beam [12], rod [13], plate [14]-[16] and pipe [17],[18]. In recent years, many studies using linear or nonlinear guided waves have been carried out and they focused on different damage types and materials [19],[20]. For linear guided wave, Sohn [38] used mode conversion technique to detect a notch on an aluminium plate. A reference-free damage detection method was introduced. Santos *et al*. [22] employed guided waves to characterize the interface texture of two-layer concrete slabs. Numerical simulation studies were carried out to investigate the feasibility and performance of the proposed method.

As compared with linear features of guided waves, the nonlinear features have attracted increasing attention due to its ability to detect both contact nonlinearity of cracks [23] and plasticity driven damages [24],[25] at impercipient level. In general, the linear features of guided waves usually require reference data to extract the damage related information for damage detection. But the varying operational [26],[27] and environmental condition [28],[29] can significantly affect the accuracy of extracting the damage related information using the reference data. Different to linear features of guided waves, the nonlinear features are potential to be developed as a reference free damage detection technique [30].

Pruell *et al*. [31] studied the plasticity driven nonlinearity using the second harmonic generation (SHG) due to phase and group velocity matching of the first and second symmetric modes of Lamb wave. They found that with larger plastic deformation, the acoustic nonlinearity induces larger magnitude of higher harmonic. Soleimanpour *et al*. [26] numerically and experimentally investigated the SHG due to contact nonlinearity at delamination in laminated composite beam. Various damage scenarios about different delamination layers and sizes were considered in their study. Lim *et al*. [33] investigated the binding conditions for nonlinear guided wave generation. Their study considered both propagating wave and stationary vibration. An aluminium plate specimen with a fatigue crack was used in their experimental studies. The binding conditions to generate modulated guided wave signals and sidebands were studied using both high and low frequency excitations. Yang *et al*. [34] investigated the SHG of the Lamb waves at fatigue crack in aluminium plate. 3D FE simulations and experiments were carried out to gain physical insights into the SHG phenomenon at fatigue crack. They also extended the work to investigate the SHG under practical situations, such as effect of the crack opening under applied loading condition and incident wave angle on the SHG [35].

4.1.2. Detection of damage for bolted joints

Research on detection of contact-type damage with nonlinear guided waves has attracted significant attention in recent years. The contact-type defects such as fatigue crack or delamination, are sources of contact nonlinearity phenomena contributing the generation of the second order harmonics. Another common type of structural deficiency related to the contact nonlinearity is the loosening of a bolted joint. The bolted joint is an essential component in many structures, e.g., wind turbines, bridges and framed buildings. Bolt loosening is one of the major concerns for engineers [36].

The loss of torque in one or more bolts can significantly decrease fatigue life of bolted joints [37], [38]. When bolt loosening occurs, the friction between the lapped areas of the joint reduces due to the decrease of the clamping force contributed by the bolts. In this situation, the applied load is directly transferred from one plate to the other through the contact area between the bolt and plates and this causes a stress concentration at the edge of the bolt hole [39]. When the structure is subjected to alternating loading, fatigue cracks can be developed at the edge of the bolt hole. Therefore, reliable and cost efficient non-destructive techniques capable to detect the bolt loosening and fatigue crack of bolted joint at critical load bearing structural components are essential for safety and integrity of a wide range of engineering structures.

4.1.3. Linear guided wave for detecting bolt loosening

There were a number of studies focused on detection of bolt loosening using linear guided waves. Wang et al. [40] investigated the relationship between the signal energy and applied torque levels at bolted connections. It was found that the wave energy propagated through the connection increases with the applied torque. In another paper, Wang et al. [41] proposed a time reversal method using the linear guided wave signals to monitor the bolted joints. Experimental study was carried out to investigate the relationship between the peak amplitudes of the time reversal focused signal and the bolt preload. However, the linear guided waves have some issues that need to be addressed before it can be applied in practical situations. For examples, as mentioned before, the linear features of guided waves are sensitive to the temperature change [19],[21]. Moreover, the boundary reflection of the linear guided waves within the lapped areas at the bolted connection would affect the linear features utilised in the detection algorithms of bolt loosening [44].

4.1.4. Nonlinear guided wave for detecting bolt loosening

Different to linear features, the nonlinear features of guided waves are more robust for structures with complex geometry [45] and under varying temperature condition. One of the most commonly used nonlinear features of guided waves is SHG due to the contact nonlinearity. This phenomenon can be described by Contact Acoustic Nonlinearity (CAN) [46]. When guided wave interacts with a contact-type of damage, such as fatigue crack and loosen bolt, repetitive collisions between contact surfaces occurs. During the collisions, the compressive and tensile pressure of the wave closes and opens the contact surfaces, respectively. However, only the compressive pressure of the wave can transmit through the closed contact surfaces. Therefore, after the incident wave interacting with the contact surfaces, the wave shape is rectified nearly half-wave. The higher harmonics are generated due to this nonlinear waveform distortion. This phenomenon is schematically illustrated in Figure 4-1.[25]

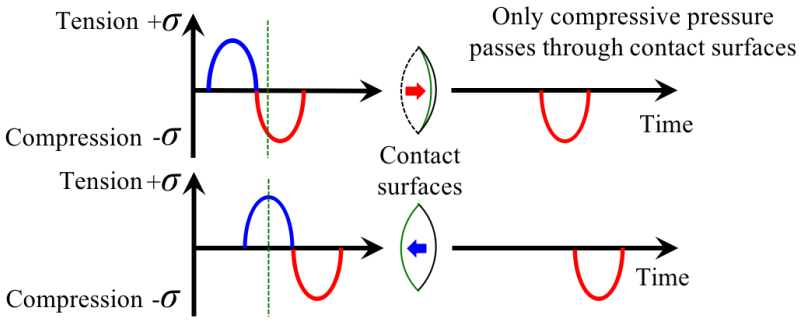

Figure 4-1: Schematic diagram of contact nonlinearity at contact surfaces

Biwa et al. [47] used bulk waves to study the SHG due to the variation of contact pressure between two separate aluminium blocks at the contact interface. They found that the amplitude of the second order nonlinear parameters decreases with the contact pressure. The study suggests that the SHG of the bulk wave is sensitive to the change of contact pressure between two contact surfaces. The bolt loosening causes a loss of contact pressure at the interface of a bolted joint so the nonlinear features can be used to detect bolt loosening at the bolted connections. In the study carried out by Lee and Jhang [48], although it focused on detecting the fatigue crack in an aluminium block using the SHG of ultrasonic bulk wave, they also experimentally investigated the closing effect of the fatigue crack. They found that the magnitude of the applied pressure is inversely proportional to the magnitude of the SHG. This

means that the contact nonlinearity reduces with the increasing torque contributed by the bolt, and vice versa. However, the safety inspection using bulk wave is only able to provide a localised assessment for structures. In practical situation, most of the structures have inaccessible areas. It is difficult to inspect these inaccessible areas using the bulk wave. Different to bulk wave, guided wave propagates along the structure, which can cover a large inspection area and can be used to inspect inaccessible locations.

In the literature, there were several studies investigated the feasibility of using the SHG of guided waves to detect the bolt loosening. For example, Amerini and Meo [20] studied the effect of bolt loosening and tightening at the bolted connection using nonlinear guided waves. They showed that the spectral amplitude difference between the carrier frequency (A_1) and the second harmonic frequency (A_2) at bolt loosening condition is much lower than that at tightening condition. They proposed a hyperbolic tangent function to predict the spectral amplitude difference for different magnitudes of the torque applied at the bolt. However, defining the damage index related to A_1 may involve some problems, as the wave reflection and contact pressure would significantly affect the amplitude of the linear wave [44]. They also suggested that there is no clear change of damage index when the magnitude of the applied torque increases beyond around 6 Nm, which means the proposed damage index may not be able to provide early detection of bolt loosening.

This study is different from the previous research efforts published in the literature. It deals with the characteristics of SHG when a loosened bolt connection is weakened by fatigue cracks. The latter represents a typical practical situation, which is of a main concern for engineers as discussed above. The current study provides a comprehensive numerical and experimental insights into the complex contact nonlinearity caused by combination of bolt loosening and fatigue cracks. These insights could further advance the non-destructive techniques for integrity monitoring of the bolted joints using nonlinear guided wave.

The paper is organized as follows. Sections 2 and 3 describe the setup of experiment and three-dimensional (3D) finite element (FE) model of bolted connections, respectively. Then, the experimental and FE simulation results are discussed in detailed in Section 4. This section employs the experimentally verified 3D FE model to investigate the SHG when a loosened bolt is weakened by fatigue crack located at the edge of the bolt hole. Different levels of bolt loosening are investigated using the experimentally verified 3D FE model. Finally, conclusions are drawn in Section 5.

4.2. Experiment

4.2.1. Experimental specimens

The experimental study considered a single-lap connection and T-joint connection as shown in Figure 4-2a and b, respectively. The lengths of the specimens are relatively short so that it can also demonstrate the proposed nonlinear guided wave approach is applicable to the situation having wave reflections from the boundaries, which has been demonstrated that it is hard to be handled using linear guided wave approach in Section 1.2.1. The first specimen is a single-lap connection as shown in Figure 4-2a. The specimen consists of two 5 mm thick plates with in-plane dimension of 50 mm × 24 mm. The second specimen is a T-joint connection (Figure 4-2b), which consists two 5mm thick plates with in-plane dimensions of 70 mm × 24 mm and 24 mm × 24 mm, respectively. Both specimens are made of G250 mild steel and the material properties are shown in Table 4-1. A M10 steel bolt was used to connect the two steel plates of each specimen. A torque wrench with electronic readings was used to tighten the bolt and measure the magnitude of the applied torque. The minimal torque that can be measured by the torque meter is 6.8 Nm and the sensitive of the measurement is ±2%.

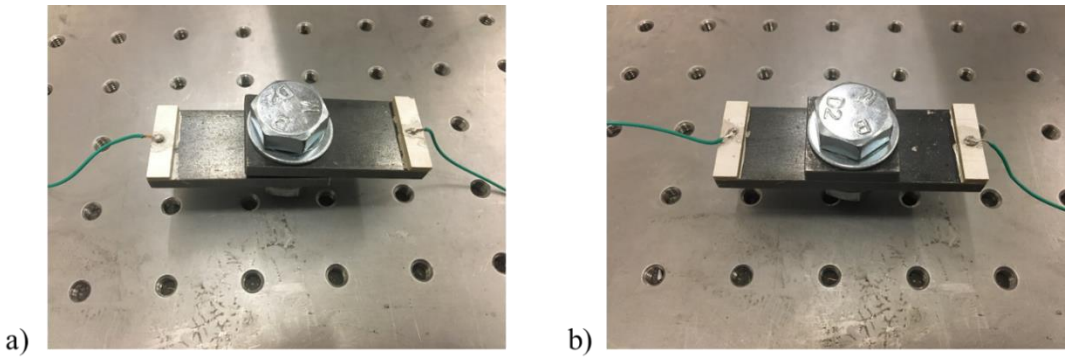

Figure 4-2: a) Single-lap joint and b) T-joint specimen used in experiment

Table 4-1: Material properties of the G250 mild steel plate

Young's Modulus (*GPa*)	205
Poisson Ratio	0.29
Density (kg/m^3)	7870

Table 4-2: Material properties of the Ferroperm Pz27 Piezoceramic disc

Young's Modulus (*GPa*)	59
Poisson Ratio	0.389
Density (kg/m^3)	7700

4.2.2. Actuating and sensing guided wave

Rectangular piezoceramic transducers (Ferroperm Pz27) with 6 mm × 12 mm in-plane dimension and 2 mm thickness were bonded to the surface of the plate by conductive epoxy. These piezoceramic transducers were used to excite and receive the wave signals. The material properties of the transducers are listed in Table 4-2. Figure 4-3 shows a schematic diagram of the experimental setup. A computer controlled signal generator (NI PIX-5412) was used to generate the excitation signal, which was a narrow-band 10-cycle sinusoidal tone burst pulse modulated by a Hanning window. 50 kHz and 200 kHz excitation frequencies were considered in this study. The excitation signal has a peak-to-peak output voltage of 10 V and was amplified by a factor of four using an amplifier (KROHN-HITE 7500) before it was sent to one of the transducers. The other transducer was used to measure the wave signals on the specimen. The measured signals were then digitized by a data acquisition system (NI PXIe-5105). The quality of the measurements was improved by averaging the signals with 64 acquisitions.

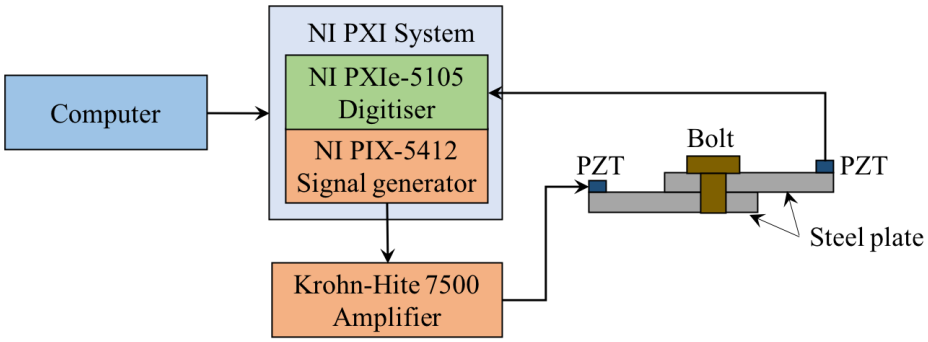

Figure 4-3: Schematic diagram of experimental setup

4.2.3. Experimental observation of SHG due to bolt loosening

The torque level was increased stepwise from 8 Nm to 20 Nm in steps of 2 Nm. The experimental process was repeated independently 10 times for each specimen and the

excitation frequency, respectively. The measured 200 kHz wave signal at the single-lap joint specimen with torque equals to 8 Nm is shown in Figure 4-4. Figure 4-4a and b show the measured time-domain signal and the frequency-domain signal processed using fast Fourier transform, respectively. As shown in Figure 4-4b, besides the SHG at frequency 2f, there are also other higher order harmonics, e.g., third (3f) and fourth (4f) harmonics. But the focus of the current study is to investigate the feasibility of using SHG to detect bolt loosening.

The extracted SHG amplitude, A_2, against the magnitude of applied torque for all 10 tests are summarised in Figures 5 and 6. Figures 5 and 6 show the averaged results for the single-lap joint and T-joint, respectively. The error bars are calculated at different applied torque magnitudes (levels).

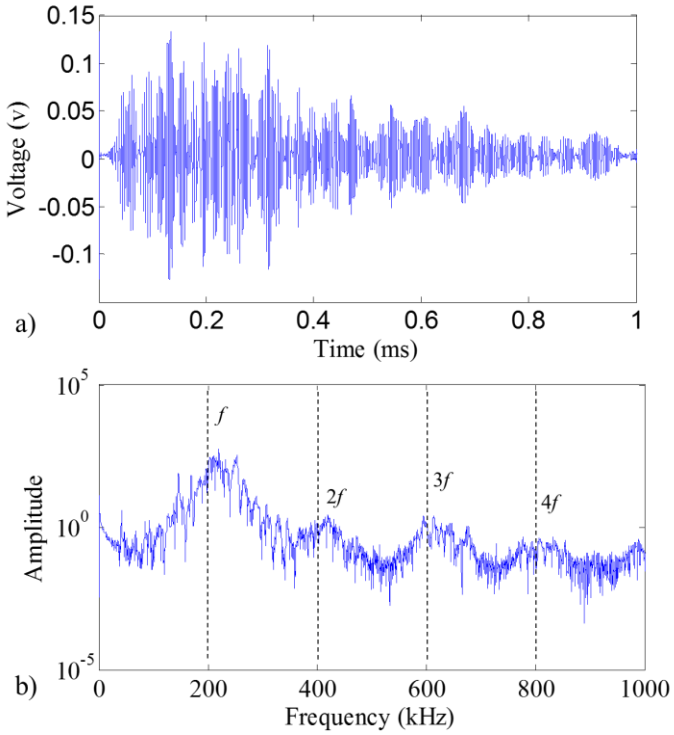

Figure 4-4: Measured a) time-domain and b) frequency-domain signals from single-lap joint specimen for 200 kHz excitation frequency and 8 Nm torque

The results indicate that the averaged SHG amplitude generally decreases with the increasing applied torque. For cases considering single-lap joint and T-joint with 50 kHz excitation frequency (Figure 4-5a and Figure 4-6a), comparing to loosened bolt, the SHG amplitude decreases by more than 60% when the bolt is tightened. When the 200 kHz excitation is used, the SHG amplitude of the tightened bolt is only reduced by about 10% at the bolt loosening

condition (Figure 4-5b and Figure 4-6b). The results also demonstrate that the magnitude of SHG for the single-lap joint at bolt loosening condition are larger than that for the T-joint, especially for the case when 50 kHz incident wave is used.

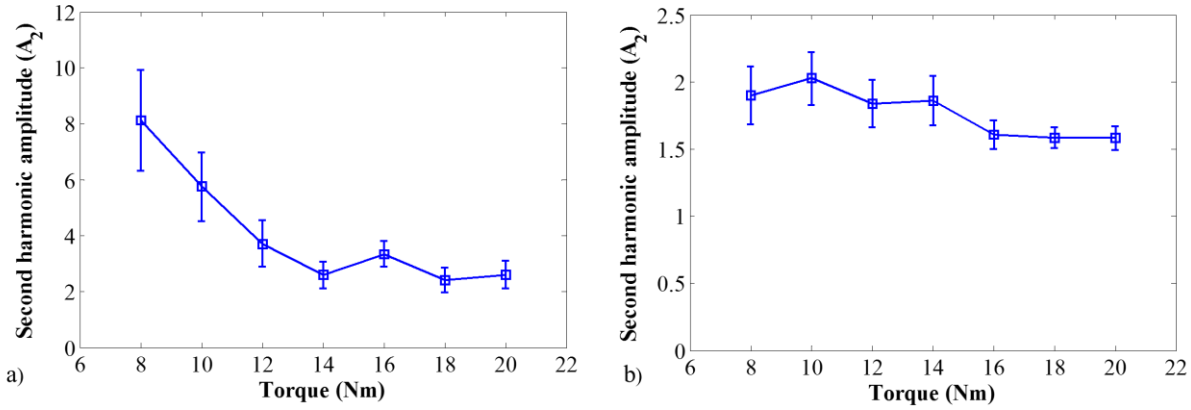

Figure 4-5: Averaged SHG amplitude against applied torque for the single-lap joint specimen with error bars for a) 50 kHz, and b) 200 kHz excitation frequency

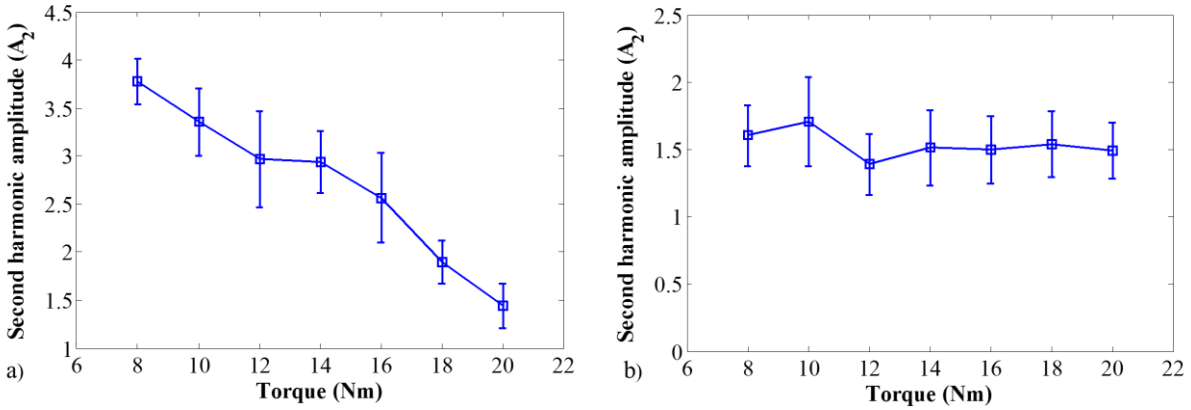

Figure 4-6: Averaged SHG amplitude against applied torque for the T-joint specimen with error bars for a) 50 kHz, and b) 200 kHz excitation frequency

Below are possible reasons that contribute to the observed features of the SHG behaviour with the change of the torque level, as well as the variation of the results.

1) The wave in the single-lap joint is transmitted through the bolted area and interacts with the two plates. The contact behaviour at the interface has a significant impact on the wave signals. Between each individual test, the contact characteristic at the interface can be quite different, especially when the bolt is loosened. Thus, the amplitude of the

SHG has larger fluctuation at the bolt loosening condition. For the T-joint specimen, the wave energy can pass through the bolted area without any interaction at the interface, therefore, the amplitude of the SHG is smaller than that in the single-lap joint specimen at the bolt loosening condition. Also, the variation of the SHG for the single-lap joint is larger than that for the T-joint.

2) The actual contact pressure at the bolted joint does not vary linearly with the applied torque. In each time of the torque is applied in the experiment, there may be a small slip between the washer and plate, the top plate and base plate, and the bolt and washer. Therefore, this changes the effective contact area and would result in different clapping behaviours and magnitudes of friction force.
3) As the bolt hole is normally designed to be slightly larger than the diameter of the thread, the gap and the contact area between the bolt thread and the plates can vary in different tests. Obviously, this can affect the measured amplitude of the SHG induced by contact nonlinearity.
4) The measurement error of the torque meter and rounding error of data acquisition process could influence the variation of the SHG in the measured data.

4.3. Three-dimensional Explicit Finite Element Simulations

4.3.1. FE modelling of bolt loosening

The configurations utilized in the experimental study were modelled using 3D explicit FE method. ABAQUS/CAE was used to model the specimen geometry and loading/contact conditions as shown in Figure 4-1. In the FE model, only the plates and washer of the specimens were modelled and the effect of the bolt tightening was modelled by applying pressure on the washer. The schematic diagrams of the FE models are shown in Figure 4-7. The dimensions of the FE models are exactly the same as those specimens used in the experiment. The specimens were modelled using 8-node linear brick elements with reduced integration (C3D8R). Hourglass control was used to ensure the stability of the simulations. The in-plane dimension of the element is 0.4 mm × 0.4 mm. This ensures that there are at least 20 elements in the wavelength of the incident wave and second harmonic wave. The thickness of the element is 0.5 mm so there are ten elements in the thickness direction of the plates.

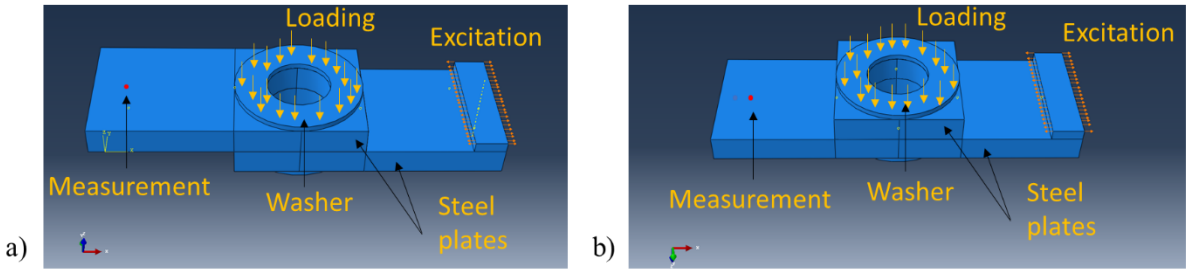

Figure 4-7: Schematic diagram of the FE model for the a) single-lap joint and b) T-joint

The interaction between the plates at the joint location was modelled by 'hard' normal interaction and frictional tangential interaction with friction factor equals to 0.5 **Error! eference source not found.**. The excitation signal and excitation frequencies are the same as those used in the experiment, which are narrow-band 10-cycle sinusoidal tone burst pulse modulated by a Hanning window, and at 50 kHz and 200 kHz. The guided wave was generated by applying nodal displacement at the top edge of the piezoceramic transducer, and the propagating waves were measured using the strain of an element. The bolt tightening condition was modelled by applying evenly distributed pressure on the washers. The magnitude of the pressure is determined by [36]:

$$P = \frac{T}{kdA} \qquad (1)$$

where P is the pressure, T is torque applied on the bolt, k is the torque coefficient, d is the nominal diameter of the bolt, and A is the area of washer. k = 0.2 is usually used for steel bolts[36]. In this study, the pressure on the washer is applied through a quasi-static loading using 'smooth step' in ABAQUS to avoid inducing any shock wave on the specimens due to sudden loading condition. The FE simulation of the bolt loosening includes two steps, 1) the washers are loaded using dynamic explicit procedure with smooth loading to avoid the transient effect in applying the pressure, and then 2) guided waves are excited and SHG is induced due to the interaction between the incident wave and the joint with bolt loosening.

4.4. Results and Discussions

4.4.1. FE calculated and experimentally measured SHG due to bolt loosening

Figure 4-8 shows the FE calculated and experimentally measured amplitude of SHG, which is normalized by the averaged value of A_2 at different torque levels of the corresponding case. The averaged experimental results of the 10 individual tests are also shown in Figure 4-6. It is evident that, for both excitation frequencies, the amplitudes of the SHG decrease with the increasing torque. Meanwhile, the variation and trend of the experimental and FE calculated results are very similar. The results indicate that the FE model is capable to provide a reasonable prediction of the SHG for the bolt with different levels of the applied torque.

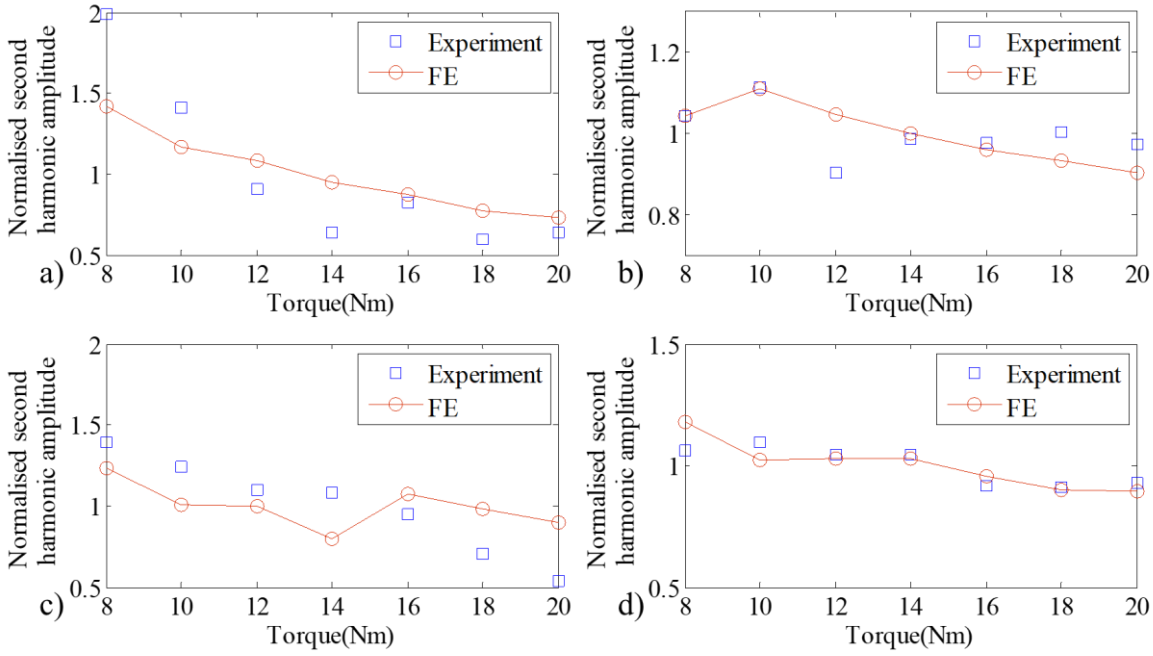

Figure 4-8: FE calculated and experimentally measured normalised second harmonic amplitude for single lap joint using a) 50 kHz and b) 200 kHz excitation frequency; and T-joint using c) 50 kHz and d) 200k Hz excitation

4.4.2. Effect of excitation frequency

As shown in the experimental and FE results, the selection of excitation frequency plays an important role in detecting the bolt loosening level. Also, the wave modes of the guided wave generated by the piezoceramic transducer highly depend on the excitation frequency. In this section, the wave motion of the excited guided wave is investigated to determine the efficiency of different wave modes in SHG due to bolt loosening.

In the literature, it has been shown that the 3D FE simulation can accurately predict the linear wave propagation in both isotropic and composite materials [52],[53]. This study employs the 3D FE model to investigate the 50 kHz and 200 kHz linear wave propagation to reveal the dominant wave mode at each excitation frequency. The model has the same thickness, width, material properties and distances between actuator and measurement points as the FE models described in Section 3.1, except that the length of the model is extended to 1 m to avoid the wave reflected from the boundaries. The model is shown in Figure 4-9. Since the guided wave propagation is a local phenomenon, the only difference between the extended length model and the model shown in Figure 4-7 is the wave reflected from the boundaries.

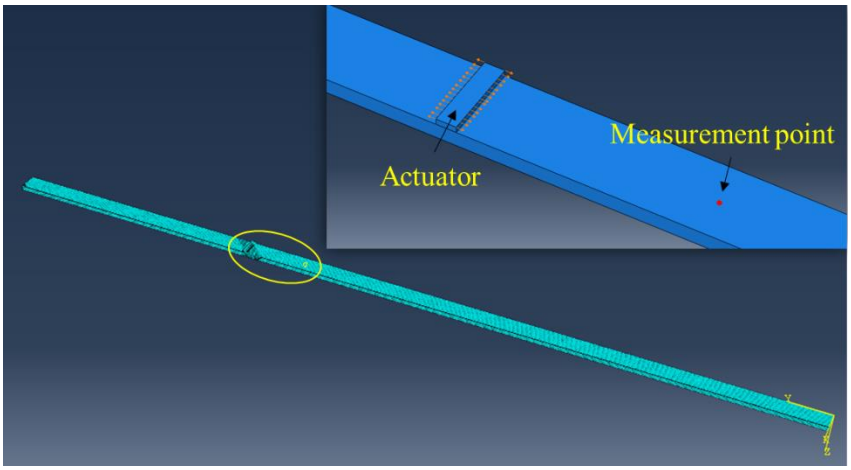

Figure 4-9: 3D FE model for studying the in-plane and out-of-plane deformation of the guided wave propagation

Both the in-plane and out-of-plane displacements are measured at the measurement point as shown in Figure 4-10. Figure 4-10 shows that the out-of-plane displacement of the 50 kHz guided wave is at least two times larger than that of 200 kHz guided wave. This is because the dominated wave mode is the fundamental anti-symmetric mode (A_0) at 50 kHz. However, both 50 kHz and 200 kHz guided waves have very similar magnitude of in-plane displacement.

Based on the results presented in Section 4.1, the A_0 guided wave, which has dominant out-of-plane motion, is more sensitive to the SHG due to changes of the contact pressure at the bolted joint. This is consistent with the findings in the previous research [49]. This explains that when 200 kHz is chosen as the excitation frequency, the amplitude reduction of the SHG with the increasing torque is less significant than that of 50 kHz guided wave.

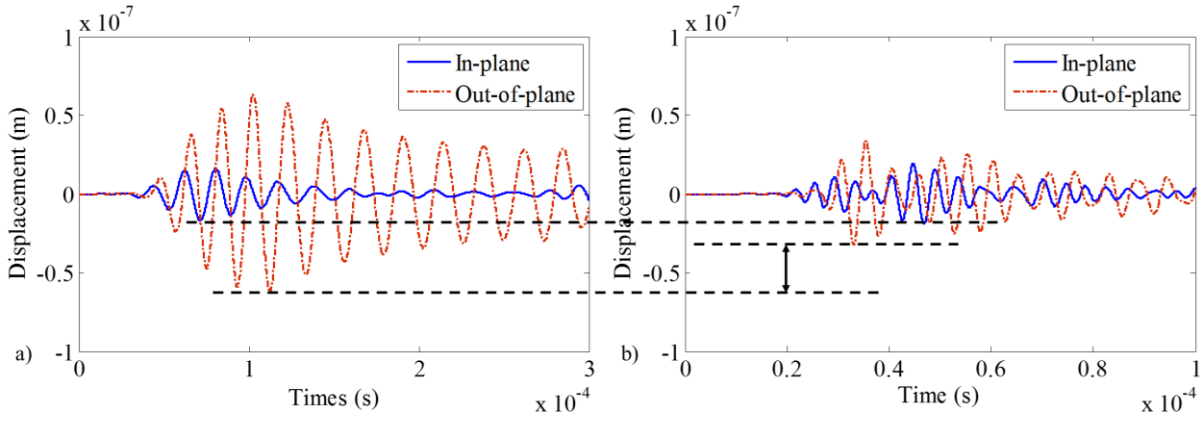

Figure 4-10: FE calculated in-plane and out-of-plane displacement at: a) 50 kHz and b) 200 kHz excitation frequency

4.4.3. Effect of fatigue cracks at loosened bolts

As discussed in Section 1, fatigue cracks are very common in bolted joints due to cyclic loading of the structure or due to the change of environmental condition. The fatigue crack would enhance the complexity of the contact nonlinearity and guided wave interaction with the overlapped area at the bolted joints, and hence, affecting the behaviour of SHG. It has been demonstrated that the 3D FE model is capable of predicting the SHG features due to the interaction of low-frequency guided wave and fatigue crack0. The similar methodology will be utilized in the current numerical study.

A 3D FE model containing two 3 mm long fatigue cracks at two sides of the bolt hole is considered in this section. The fatigue cracks are modelled by duplicating the FE nodes at the crack surface areas and the locations are shown in Figure 4-11. The measurement is also taken at the same location as the FE model shown in Figure 4-7 in Section 3.1. 'Hard' contact is defined between the crack surfaces and a friction factor of 1 is used to model the frictional interaction between the crack surfaces, which also takes into account the rough fatigue crack surfaces in real situation [34]. The features of the SHG at the bolted joint with fatigue cracks are observed at different torque levels.

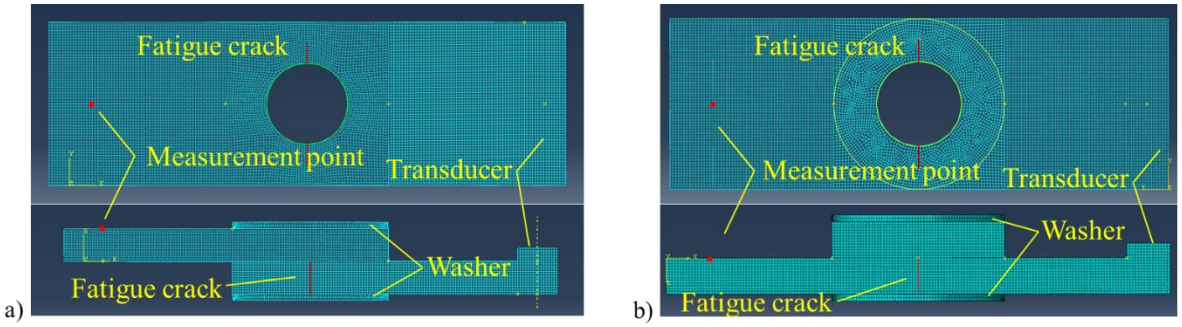

Figure 4-11: 3D FE model of a) single lap joint and b) T-joint with fatigue cracks at the bolt hole

Figure 4-12 shows the ratio of the second harmonic amplitude obtained from the FE model with the fatigue cracks to the second harmonic amplitude obtained from the FE model of the tightened bolt (intact specimen and the value of the torque for intact bolted joint is 20 Nm), and it is defined as

$$r = \frac{A_2}{A_{2,T=20\,Nm}} \quad (2)$$

where A_2 is the second harmonic amplitude of the FE model with the fatigue cracks, and A_2, T=20Nm is the second harmonic amplitude of the intact bolted joint (tightened bolt) when the torque is 20 Nm.

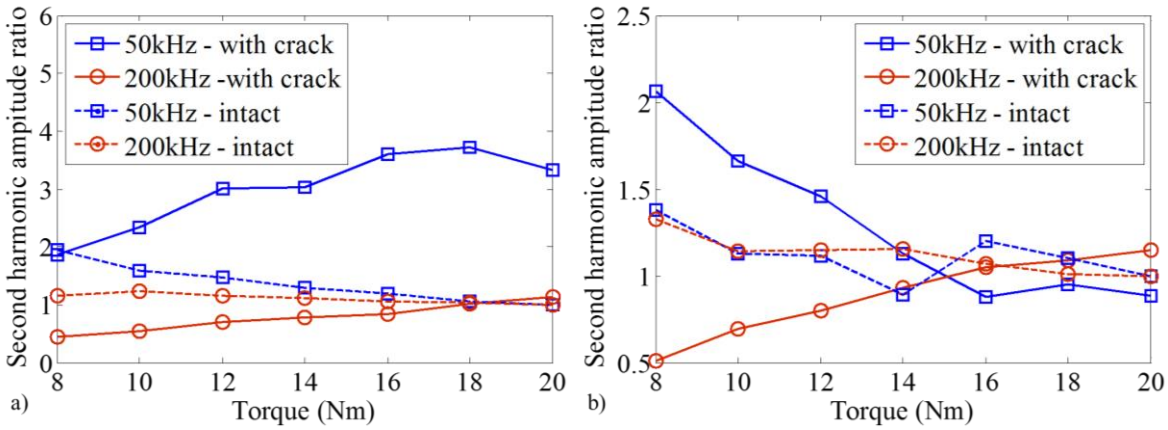

Figure 4-12: Second harmonic amplitude ratio of a) single-lap joint and b) T-joint

The results of the single-lap joint with fatigue cracks are shown in Figure 4-10a. The second harmonic amplitude ratio increases with the applied torque. When the bolt is loosened, part of

the wave energy is transferred from the fundamental frequency to second harmonic frequency due to “the breathing phenomenon” of the wave-crack interaction. But the second harmonic wave generated at the fatigue cracks cannot propagate through the joint with the loosened bolt. While the bolt is tightened, second harmonic wave due to the fatigue cracks can travel through the bolted joint, and most of the wave energy is transferred from the fundamental frequency to the second harmonic frequency due to contact nonlinearity at the fatigue cracks. However, as described in Sections 4.1, at the bolted joint, the amplitude of SHG decreases when the applied torque increases. So, in this case, the increase of A_2 due to the fatigue cracks is more significant than the decrease of A_2 due to tightened bolt.

For the T-joint (Figure 4-10b), when 200 kHz guided wave is used, the variation of the amplitude ratio is similar to that of single-lap joint. In contrast, when 50 kHz guided wave is used, the second harmonic amplitude ratio decreases when the torque increases. The reason may be that, for the T-joint, the fatigue cracks is located at the same plate of the actuator and measurement point, so the generated second harmonic wave due to fatigue crack is still able to propagate through the bolted joint even the bolt is loosened. For the 50 kHz guided wave, when the magnitude of the applied torque increases, the variation of the second harmonic amplitude ratio is dominated by the contact nonlinearity at the overlapped area of the two plates.

For the results in Figure 4-8 and Figure 4-12, when 200 kHz guided wave is used, the variation of second harmonic amplitude due to increasing torque shows an opposite trend when the fatigue cracks are modelled as compared with the results of the FE model without the fatigue cracks. Meanwhile, when 50 kHz guided wave is used as the incident wave, the variations of the second harmonic amplitude ratio for the single-lap joint with and without the fatigue cracks also show an opposite trend. As compared, for the T-joint, the trend and variation of the second harmonic ratio for the FE models with and without the fatigue cracks are similar to each other. It is possible to use 200 kHz guided wave to detect the damage and distinguish the damage type at the bolted joint by continuous monitoring the second harmonic amplitude. When incident wave is generated at 50 kHz, it is only possible to detect damages and distinguish the damage type at the single-lap joint.

4.5. Conclusions

In this study, SHG induced by the contact nonlinearity due to the bolt loosening in single-lap joint and T-joint has been studied in detail. It has been demonstrated that the FE and

experimental results have the same tendency that the value of the second harmonic amplitude for the tightened bolts is smaller than that for the loosened bolts. The study has shown that the use of the guided wave mode with dominated out-of-plane displacements (e.g. A0 guided wave) can result in much more distinctive reduction in the second harmonic amplitude and also less variation as compared to the case when the in-plane displacements dominated guided wave mode is used (e.g. the fundamental symmetric mode (S0) guided wave).

The numerical case study using 3D explicit FE simulations has been carried out to investigate the combined effect of bolt loosening and fatigue crack at bolt hole. Different trends and variations of the second harmonic amplitude against the applied torque and different excitation frequencies have been observed. The results have been compared with the corresponding cases without fatigue cracks. The results have indicated that it is possible to distinguish the situation when the joint with loosened bolt is weakened by the fatigue cracks.

The current study focuses on the bolted joint with a single bolt. But in the practical condition, the structure component can contain a group of bolts. Future studies can be carried out on full-scale structural components and bolted joint within a group of bolted connections. This will further justify the feasibility of using the SHG in detecting and distinguishing the bolt loosening with and without the fatigue cracks in practical situation.

Acknowledgement

This work was supported by the Australian Research Council (ARC) under Grant Number DP160102233. The supports are greatly appreciated.

References

[1] Gros X *1996 NDT Data Fusion* (London: Arnold)

[2] Komorowski JP, Forsyth DS 2000 *Aircr Eng Aerosp Technol*; **71** 5-13

[3] Lepine BA, Giguere JSR, Forsyth DS, Chahbaz A, Dubois JMS 2002 *AIP Conf Proc*; **615** 415–422

[4] Hiasa S, Birgul R, Catbas FN. 2016 *J Civil Structl Health Monit* **6** 619-636

[5] Schmerr LW, Song JS. 2007 *Ultrasonic nondestructive evaluation systems* (Springer)

[6] Carden EP, Fanning P. 2004 *Struct Health Monit* **3** 355–377

[7] Khoo LM, Mantena PR, Jadhav P 2004 *Struct Health Monit* **3** 177–194

[8] Hamey CS, Lestari W, Qiao P, et al 2004 *Struct Health Monit* **3** 333–353

[9] Giurgiutiu V and Bao J 2004 *Struct Health Monit* **3** 121-140

[10] He S, Ng CT 2016 *Eng Struct* **127** 602-614

[11] Rose LJ 2002 *J Press Vess Tech* **124** 273-282

[12] He S, Ng CT 2017 *Mech Syst Sig Process* **84** 324-345

[13] Raisutis R, Kazys R, Zukauskas E, Mazeika L, Vladisauskas A 2010 *NDT E Int* **43** 416–24

[14] Ng CT 2015 *Earthqu Struct* **8** 821–41.

[15] Cho H, Lissenden C 2012 *Struct Health Monit* **11** 393–404

[16] Haynes C, Todd M 2015 *Mech Syst Signal Process* **54–55** 195–209

[17] Lowe MJS, Alleyne DN, Cawley P 1998 *Ultrasonics* **36** 147–154

[18] Lovstad A, Cawley P 2012 *NDT&E Int* **46** 83–93.

[19] Aryan P, Kotousov A, Ng CT, Cazzolato BS 2017 *Struct Contr Health Monitor* **24** e1894

[20] Mohseni H, Ng CT 2018 *Struct Health Monit* https://doi.org/10.1177/1475921718754371

[21] Sohn H 2011 *KSCE J Civil Eng* **15** 1395-1404

[22] Santos P, Julio E, Santos J 2010 *Eng Struct* **32** 207-217

[23] He S, Ng CT 2017 *Smart Mater Struct* **26** 085002

[24] Bermes C, Kim JY, Qu J, Jacobs LJ 2008 *Mech. Syst. Sig. Process* **22** 638-646

[25] Jhang KY 2009 *Intern J Precision Eng Manu* **10** 123-135

[26] Mohabuth M, Kotousov A, Ng CT 2016 *Intern J of Nonlinear Mech* **86** 104-11

[27] Mohabuth M, Kotousov A, Ng CT 2018 *Smart Mater Struct* **27** 025003

[28] Konstantinidis G, Drinkwater BW, Wilcox PD 2006 *Smart Mater Struct* **15** 967–976

[29] Aryan P, Kotousov A, Ng CT, Wildy S 2016 *Smart Mater Struct* **25** 035018

[30] Soleimanpour R, Ng CT 2017 *Eng Struct* **131** 207-219

[31] Pruell C, Kim JY, Qu J, Jacobs LJ 2009 *Smart Mater Struct* **18** 035003

[32] Soleimanpour R, Ng CT, Wang CH 2017 *Struct Health Monit* **16** 400-417

[33] Lim HJ, Sohn H, Liu P 2014 *Appl Phys Lett* **104** 214103.

[34] Yang Y, Ng CT, Kotousov A, Sohn H, Lim HJ 2018 *Mech Syst Signal Process* **99** 760-773

[35] Yang Y, Ng CT, Kotousov 2018 *Smart Mater & Struct* https://doi.org/10.1088/1361-665X/aab867

[36] Caccese V, Mewer R, Vel SS 2004 *Eng Struct* **26** 895-906.

[37] Ju SH, Fan CY, Wu GH 2004 *Eng Struct* **26** 403-413.

[38] Minguez JM, Vogwell J 2006 *Eng Failure Analy* **13** 1410-1421

[39] Salih EL, Gardner L, Nethercot DA 2011 *Eng Struct* **33** 549-562

[40] Wang T, Song G, Wang Z, Li Y 2013 *Smart Mater Struct* **22** 087001

[41] Wang T, Liu S, Shao J, Li Y 2016 *Smart Mater Struct* **25** 025010

[42] An YK, Sohn H 2010 *Struct Health Monitor* **17** 730-741

[43] Aryan P, Kotousov A, Ng CT, Cazzolato B 2017 *Struct Control Health Monitor* **24** e1884

[44] Bao J, Giurgiutiu V 2013 *Proc SPIE 2013* **869521**

[45] Dutta D, Sohn H, Harries K, Rizzo P 2009 *Struct Health Monit* **8** 0251-12.

[46] Solodv IY, Krohn N, Busse G 2002 *Ultrasonics* **40** 621-625

[47] Biwa S, Hiraiwa S, Matsumoto E 2006 *Ultrasonics* **44** e1319-e1322

[48] Lee TH, Jhang KY 2009 *NDT&E Int* **42** 757-764

[49] Amerini F, Meo M 2011 *Struct Health Monitor* **10** 659-672

[50] Blau PJ 2009 Friction Science and Technology (Boca Raton: CRC Press).

[51] Lu Y, Ye L, Su Z, Yang C 2008 *NDT&E Int* **41** 59-68

[52] Ng CT 2015 *Intern J Struct Stab Dyn* **15** 1540010

[53] Lowe M, Cawley P, Kao J, Diligent O 2002 *J Acoust Soc Am* **112** 2612-2622

Chapter 5. Second Harmonic Generation of Guided Wave at crack-induced debonding in FRP Strengthened Metal Plates

(Paper 4, Published)

Yi Yang[a], Ching-Tai Ng[a], Andrei Kotousov[b]

[a] School of Civil, Environmental and Mining Engineering, The University of Adelaide, Adelaide, SA 5005, Australia

[b] School of Mechanical Engineering, The University of Adelaide, Adelaide, SA 5005, Australia

Publication: Yang Y, Ng C, Kotousov A, 2019 *Int. J. Str. Stab. Dyn* **19**(1) 1940006

Statement of Authorship

Title of Paper	Second harmonic generation of guided wave at crack-induced debonding in FRP strengthened metal plates
Publication Status	☑ Published ☐ Accepted for Publication ☐ Submitted for Publication ☐ Unpublished and Unsubmitted work written in manuscript style
Publication Details	Yang, Y., Ng, C., & Kotousov, A. (2018). Second harmonic generation of guided wave at crack-induced debonding in FRP strengthened metal plates. *International Journal of Structural Stability and Dynamics*. 19(1), 1940006

Principal Author

Name of Principal Author (Candidate)	Yi Yang
Contribution to the Paper	Undertook literature review, developed numerical models, performed data processing and prepared manuscript
Overall percentage (%)	80%
Certification:	This paper reports on original research I conducted during the period of my Higher Degree by Research candidature and is not subject to any obligations or contractual agreements with a third party that would constrain its inclusion in this thesis. I am the primary author of this paper.
Signature	Date 11/01/2019

Co-Author Contributions

By signing the Statement of Authorship, each author certifies that:

i. the candidate's stated contribution to the publication is accurate (as detailed above);
ii. permission is granted for the candidate in include the publication in the thesis; and
iii. the sum of all co-author contributions is equal to 100% less the candidate's stated contribution.

Name of Co-Author	Ching-Tai Ng
Contribution to the Paper	Helped numerical model development, helped review manuscript and prepare for submission, and acted as corresponding author
Signature	Date 11/1/2019

Name of Co-Author	Andrei Kotousov
Contribution to the Paper	Helped evaluate and edit the manuscript.
Signature	Date 4/1/2019

Please cut and paste additional co-author panels here as required.

Abstract

The use of fibre reinforced polymer (FRP) has been widely recognised to be an effective and economical way to strengthen existing structures or repair damaged structures for extending their service life. This study investigates the feasibility of using nonlinear guided wave to monitor crack-induced debonding in FRP strengthened metallic plates. The study focuses on investigating the nonlinear guided wave interaction with the crack-induced debonding. A three-dimensional (3D) finite element (FE) model is developed to simulate the crack-induced debonding in the FRP strengthened metallic plates. The performance of using fundamental symmetric (S_0) and anti-symmetric (A_0) mode of guided wave as incident wave in the second harmonic generation at the crack-induced debonding is investigated in detail. It is found that the amplitude of the second harmonic and its variation with different damage sizes are very different when using S_0 and A_0 guided wave as the incident wave, respectively. The results suggest that it is possible to detect potential damage and distinguish its type based on the features of the generated second harmonic.

Keywords: FRP strengthening; second harmonic generation; fatigue crack; debonding; finite element simulation, nonlinear guided wave

5.1. Introduction

FRP strengthened aluminium plates have been widely used in aircraft structures due to its ability in fatigue crack grow resistance, high tensile strength and low density [1],[2]. Meanwhile, externally bonded composite patches have also been applied to repair cracks in aircraft structures. The composite repair provides efficient load transfer and reinforcement for the structures with cracks, and thus, it prevents or retards the crack propagation [1].

For the FRP strengthened aluminium plates, damages, such as fatigue crack and debonding, can also be generated due to impact or fatigue loading Thus, it needs a reliable damage detection system that can detect both fatigue crack and debonding to ensure the safety and integrity of the structure. For composite repaired aluminium plates, the existing crack can still propagate under fatigue loading [4]. Meanwhile, debonding between the composite patch and damaged structure can be initiated by poor bonding or propagation of fatigue crack [5]. The

debonding area can grow under loading and result in losing the strength of the reinforcement. As a result, it is necessary to monitor the integrity of the composite repair structures constantly.

5.1.1. Linear guided wave

Guided wave, with the ability to inspect a larger area compared with the ultrasonic bulk wave [6] and high sensitivity to small and different types of damages [7]-[9], provides an attractive approach for damage detection. In the last two decades, guided wave has attracted significant research interests [6], [9]. In general, the studies focused on understanding the physical insights into the guided wave interaction with different types of damages, e.g. thickness reduction [10], crack [11],[12], delamination [13]-[16] and debonding [17],[18], and developing guided wave based damage detection techniques using time-of-flight information of the waves [19], maximum-likelihood estimation [20], imaging approach [21], phase-array approach [22], model-based approach [23], [24] and time-reversal approach [25] etc.

Guided wave has been used to detect and monitor damages in the metallic plates strengthened by externally bonded materials. Pavlopoulou *et al.* [26] used linear Lamb wave propagation through a notched aluminium plate bonded with an aluminium patch. The experiment showed that the crack and debonding growth under cyclic tensile loading could be monitored by their proposed damage detection method using outlier analysis. Puthillath and Rose [27] experimentally studied the adhesive and cohesive weakness on an aluminium aircraft skin repaired by a titanium repair patch using Lamb wave propagation. They observed the energy level of the received Lamb wave after propagating through the defect area. Ihn and Chang [4] carried out an experimental study using a built-in piezoelectric senor/actuator network within a composite repair patch bonded on a notched aluminium plate. They proposed to use fundamental anti-symmetric (A_0) and symmetric mode (S_0) of Lamb wave to detect the debonding and fatigue crack on the repaired material, respectively. It should be noted that of the aforementioned studies only focused on using linear guided wave, which is not as sensitive as the nonlinear guided wave in detecting incipient damages and early state of material degradations [28].

5.1.2. Nonlinear Guided Wave induced by Contact Nonlinearity

Different to linear guided wave, nonlinear guided wave correlates the presence and characteristics of a damage with measured signals whose frequencies differ from the

frequencies of the input signal to the structures. The generation of signal with different frequencies is a result of a nonlinear transformation of the input energy due to damage or other nonlinearities.

Higher harmonic generation is one of the commonly used nonlinear features. The generation of higher harmonics of contact-type defects, such as fatigue cracks, delamination and debonding, is mainly due to \contact nonlinearity [29]. Taking fatigue crack as an example, when guided wave propagates through the fatigue crack, the compressional part of the wave closes the crack while the tensile part open it. As a result, the compression part of the wave can pass through the crack, while the tensile part cannot, and a nearly half-wave rectification of the waveform occurs after the wave passes through the crack [30]. Previous studies proved the ability of using nonlinear guided waves, typically higher harmonic generation, to detect delamination and fatigue cracks [31]-**Error! Reference source not found.**. Soleimanpour *et l.* [32] investigated the higher harmonic generation of A0 guided wave at a delamination in composite beams. Both experiments and FE simulations were used to provide physical insights into the higher harmonic generation due to delaminations with sizes and locations. Yang *et al.* **Error! Reference source not found.** investigated the second harmonic generation in an luminium plate with a fatigue crack. They found that S0 guided wave is more sensitive to the fatigue crack than A0 mode, and it can generate larger magnitude of second harmonic.

In practical situation, when the fatigue crack appears in the FRP strengthened metallic plate, it could lead to debonding between the FRP and metallic plate at the area surrounding the fatigue crack. The study of higher harmonic generation due to the combined effect of both fatigue crack and debonding in the FRP strengthened metallic plate was very limited in the literature. Most of the existing studies only considered the fatigue crack or debonding separately [34]. Therefore, this study investigates the second harmonic generation due to the interaction of guided wave at crack-induced debonding. In this study, three-dimensional (3D) finite element (FE) simulation, which was proved to be capable of providing a reliable prediction on both linear [35] and nonlinear **Error! Reference source not found.** guided wave features at the amages in structures, is used to gain physical insights into the higher harmonic generation phenomenon. This study indicates the feasibility of using second harmonic generation in monitoring the propagation of fatigue crack and debonding in the FRP strengthened metallic plate.

The rest of the paper is arranged as follow. Section 2 describes the details of the 3D FE model, in which the crack-induced debonding is also described in detail. Section 3 presents the results and discussion of a series of numerical case studies using the 3D FE model. Finally, conclusions are presented in Section 4.

5.2. Three-dimensional finite element model

5.2.1. Modelling of guided wave propagation in FRP strengthened aluminium plate

A FRP strengthened aluminium plate is modelled using commercial FE software, ABAQUS. The schematic diagram of the plate model is shown in Figure 5-1. The model consists of a 400mm×200mm×1.6mm aluminium plate, in which the top and bottom surface of the aluminium plate are strengthened by a 400mm×200mm×0.8mm three-ply $[0]_3$ unidirectional composite laminate. The lamina is made by Cycom® 970/T300 unidirectional carbon/epoxy prepreg tapes with 0.55 fibre volume fraction and 0.2 mm thickness[35]. The material properties of the lamina are shown in Table 5.1. In the model, the fibres of the composite laminate are all align with 1-axis direction as defined in Figure 5-1. For the aluminium plate, the Young's modulus, Poisson ratio and density of the material are 70GPa, 0.33 and 2700kg/m^3, respectively.

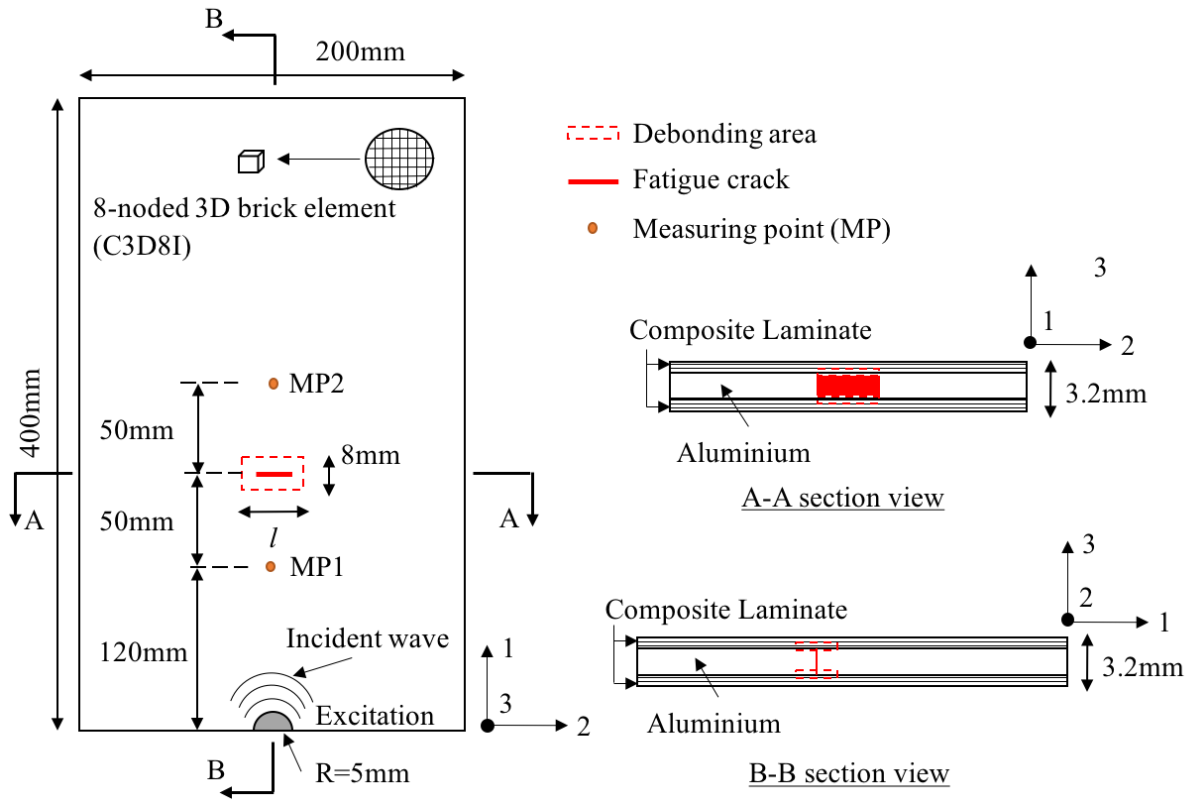

Figure 5-1: Schematic diagram of the 3D FE model in ABAQUS

Table 5-1. Material properties of Cycom® 970/T300 lamina

E_{11}(GPa)	E_{22}(GPa)	E_{33}(GPa)	G_{12}(GPa)	G_{13}(GPa)	G_{23}(GPa)	v_{12}	v_{13}	v_{23}	ρ(kg/m^3)
128.75	8.35	8.35	4.47	4.47	2.90	0.33	0.33	0.44	1517

The incident guided wave is a 200kHz narrow-band six-cycle sinusoidal tone burst pulse modulated by a Hanning window. Figure 5-2 shows the phase and group velocity disperse curves of the FRP strengthened aluminium plate obtained from DISPERSE. The figures show that only S_0 and A_0 guided wave can be excited at 200kHz. The guided wave is excited at the location of the plate as shown in Figure 5-1. The guided wave is excited by applying the nodal displacement to two half circle transducer regions located at the top and bottom surface of the plate. Both reflected and transmitted signals at the damage are measured at the measuring points MP1 and MP2 as shown in Figure 5-1, respectively.

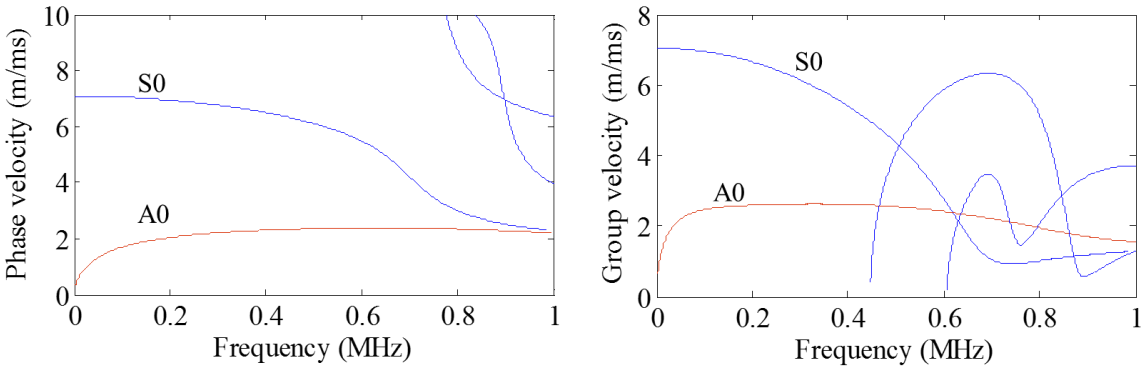

Figure 5-2: Phase and group velocity dispersion curve of the 3.2mm thick FRP strengthened aluminium plate

For the excitation of S_0 guided wave, in-plane displacement is applied to the circumferences of the transducer region located at the top and bottom surface of the plate, at which the displacement is applied in radial direction as shown in Figure 5-3a. While for the excitation of A_0 guided wave, out-of-plate displacement is applied to the whole surface of the transducer regions at the top and bottom surface as shown in Figure 5-3b. The magnitude of the displacement is 1μm. The propagating guided wave signal is obtained at the measurement points as shown in Figure 5-1. The S_0 and A_0 guided wave is measured through the strain in 1-axis and 3-axis direction as shown in Figure 5-1, respectively.

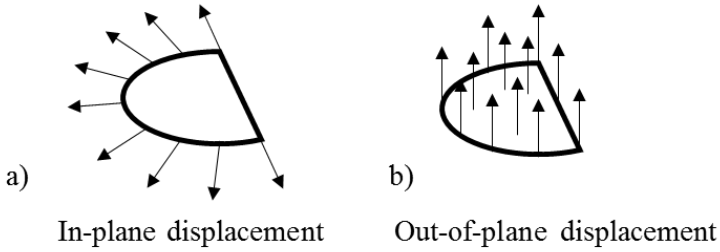

Figure 5-3: Excitation of S_0 and A_0 guided wave on a half circle transducer region

Eight-noded 3D fully integrated linear brick elements, C3D8I, in which each node has three translational degrees-of-freedom (DoFs), are used to model the FRP strengthened plate. The element size is 0.4mm×0.4mm×0.4mm so the FRP strengthened plate are modelled by eight layers of elements in the through-thickness direction, in which the aluminium plate and each of the composite laminate is modelled by four and two layers of elements, respectively. In the in-plane direction, there are at least 20 elements per wavelength for the incident wave at excitation frequency, i.e. 200kHz (10mm for A_0 guided wave and 35mm for S_0 guided wave) and 10 elements per wavelength for the second harmonic guided wave at 400kHz (5mm for A_0 guided wave and 16mm for S_0 guided wave). The simulation is solved using the ABAQUS/Explicit.

5.3. Modelling of crack-induced debonding

A fatigue crack is first modelled in the aluminium plate by inserting a seam as shown in Figure 5-4, which generates duplicated nodes at the pre-defined crack location as shown in Figure 5-1. The composite laminate is bonded to the top and bottom surface of the aluminium plate using tie constraint at the contacting interfaces, except for the areas modelled as debonding as shown in Figure 5-4. The width of the debonding is fixed at 8mm. For the fatigue crack and debonding, hard normal contact and friction tangential contact are applied to the contacting interfaces to prevent nodes penetration, and thus, simulating the clapping behaviour when the guided wave interacts with the contact-type defects. For the fatigue crack, a friction coefficient of 1.5 is used **Error! Reference source not found.**, and for the debonding, a friction of 0.23 coefficient is sed [36].

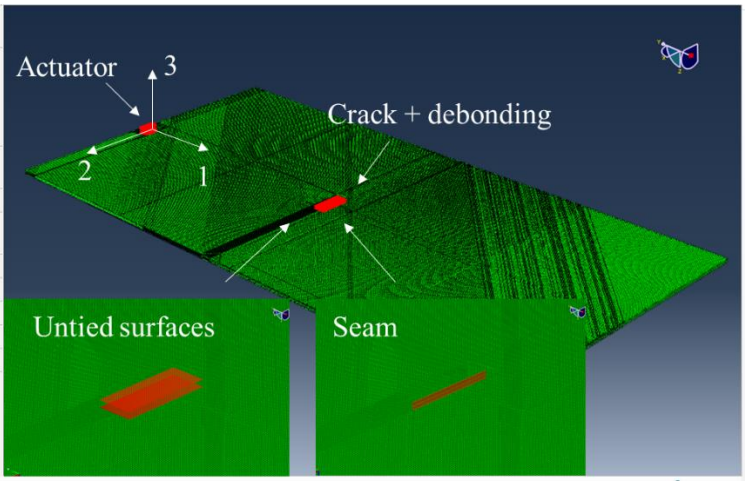

Figure 5-4: FE model of the FRP strengthened aluminium plate with a 20mm long fatigue crack and two 20mm long debonding areas

Figure 5-5 shows the snapshots of A_0 guided wave propagating on the model as shown in Figure 5-4. Figure 5-5a clearly shows that A_0 guided wave is properly excited, and the peak of the wave is in the fibre orientation of the FRP. As shown in Figure 5-5b, when the wave propagate through the damage area, both reflected and transmitted wave from the damage are observed. Meanwhile, Figure 5-5b also shows that the debonding and fatigue crack are opened by the guided wave.

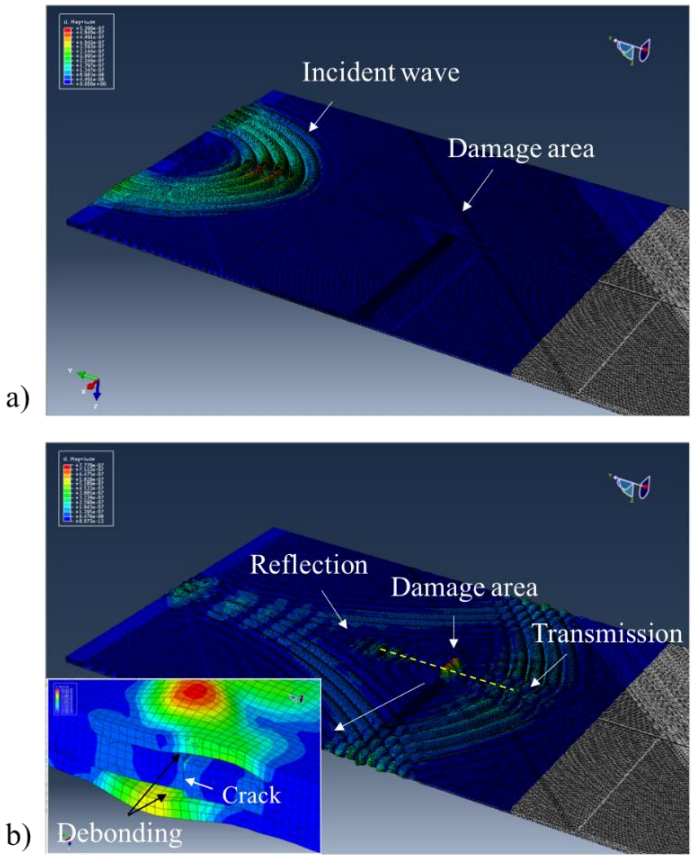

Figure 5-5: Snapshots of guided wave propagation in the FRP strengthened aluminium plate with a 20mm long fatigue crack and a 20mm long debonding: a) A0 guided wave excited by the actuator, and b) transmitted and reflected wave from the damage area and the cross-section view at the damage area.

5.4. Case studies and discussions

A series of case studies were carried out to investigate the crack-induced debonding on the higher harmonic generation of the guided wave in the FRP strengthened aluminium plate. Three scenarios were considered in this study. In each scenario, the S_0 and A_0 guided wave was used as incident wave, separately. Below is a summary of the scenarios considered in this study:

Scenario 1. There is no debonding between aluminium and composite laminates. Only the fatigue crack is modelled and the crack lengths considered are 8mm, 12mm, 16mm and 20mm.

Scenario 2. Both fatigue crack and debonding are modelled, and both crack lengths and debonding lengths considered are 8mm, 12mm, 16mm and 20mm.

Scenario 3. Both figure crack and debonding are modelled. The crack length is fixed at 8mm but the debonding lengths considered are 8mm, 12mm, 16mm and 20mm.

Figure 5-6a shows the time-domain signal obtained at the measurement point MP1, i.e. reflected wave, from the plate with a 20mm long fatigue crack only. In Figure 5-6, S_0 guided wave was used as the incident wave. The obtained time signal was processed using Short Time Fourier Transform (STFT), which provides the time-frequency information of the signal. The spectrogram parameters in the STFT were carefully selected by a series of trials to ensure the balance between time and frequency resolution. Figure 5-6b and c show the spectrogram of the incident wave and the second harmonic wave, respectively. The results show that the second harmonic, which is reflected from the fatigue crack, arrives later than the incident wave. The arrival time of the incident wave and second harmonic wave has good agreement with the arrival time calculated based on the group dispersion curve in Figure 5-2.

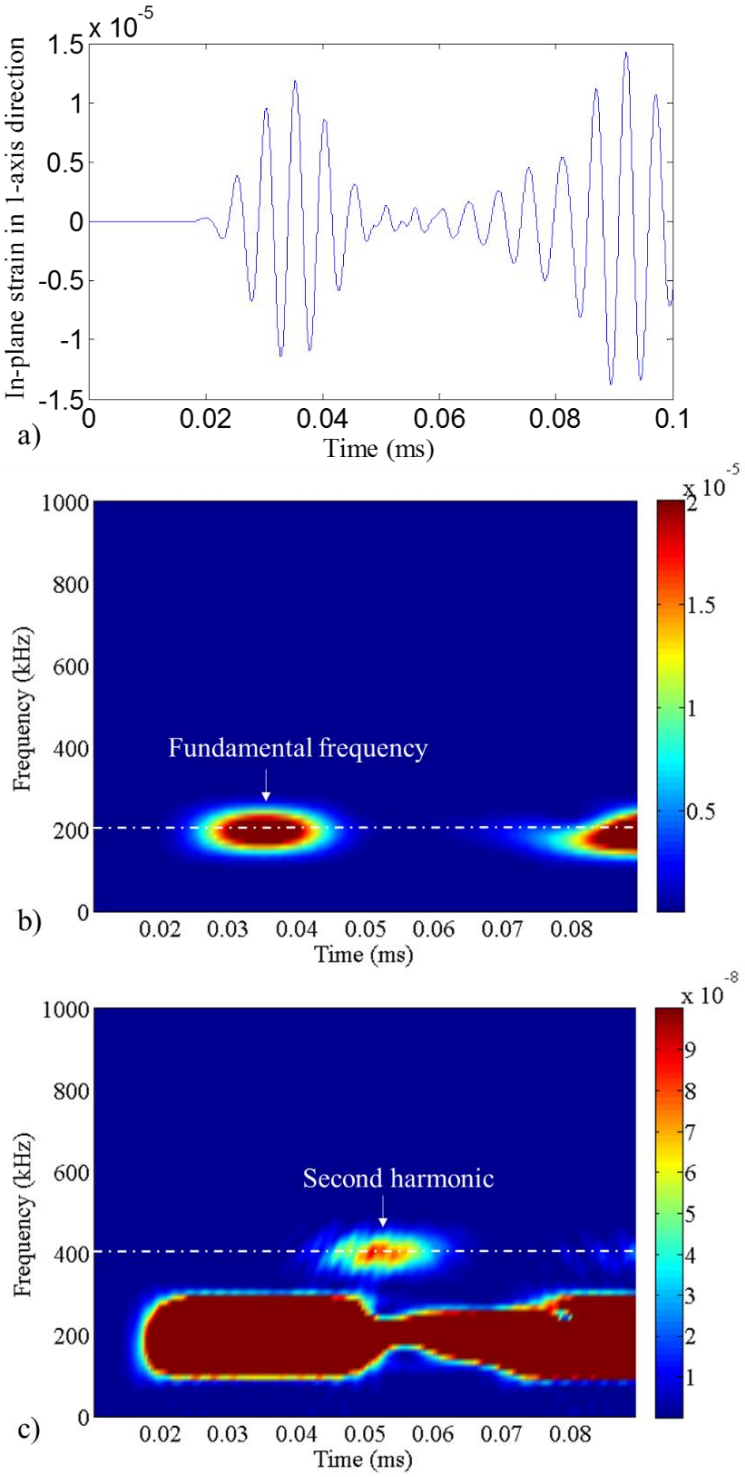

Figure 5-6: Reflected S0 guided wave obtained from the model with a 20mm fatigue crack, a) time-domain signal, b) the corresponding spectrogram, and c) spectrogram with modified colour scale for displaying the second harmonic component

The amplitude profiles of the spectrogram at 200kHz (f_0) and 400kHz ($2f_0$) were extracted and plotted in Figure 5-7. The peak of the second harmonic amplitude profile was obtained and

compared with the results obtained in other scenarios. The second harmonic amplitude was normalised by the maximum amplitude of the signal at fundamental frequency obtained at the damage centre location of the corresponding intact FRP strengthened plate. For Scenario 1 considering only the crack growth, the normalised second harmonic amplitude is denoted as $A_{2,c}$, while for Scenarios 2 and 3, the normalised second harmonic amplitude is denoted $A_{2,c+d}$ and $A_{2,d}$, respectively. The subscripts 'c', 'c+d' and 'd' mean the results obtained from the model with the crack only, crack and debonding, and debonding with fixed crack length, respectively.

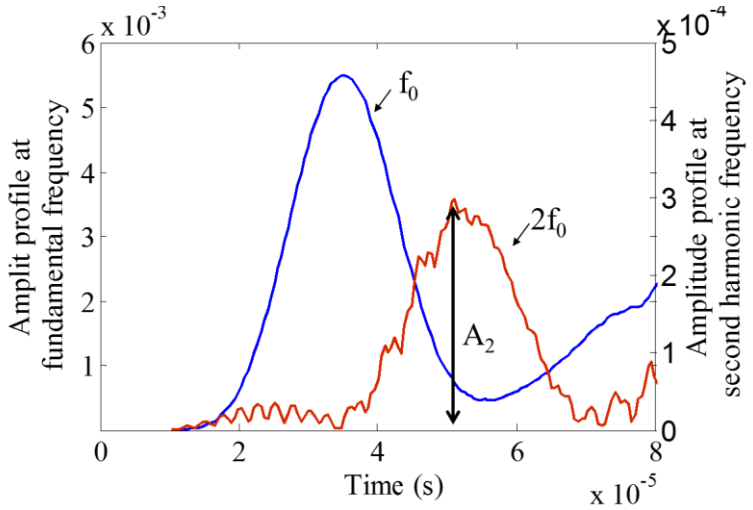

Figure 5-7: Amplitude profile at fundamental frequency (blue line) and second harmonic frequency (red line) for the model with a 20mm fatigue crack and S0 incident wave.

5.4.1. Scenario 1

For the Scenario 1, the model contains a fatigue crack only. Figure 5-8 shows that the value of A_{2c} obtained with S_0 incident wave is higher than that of using A_0 incident wave for different crack lengths in both reflected and transmitted signals. Meanwhile, when crack size increases, the value of $A_{2,c}$ increases monotonously of using both S_0 or A_0 guided wave as incident wave. However, when A_0 guided wave is used as the incident wave, both the magnitude and the rate of increase of $A_{2,c}$ are smaller than that of using S_0 as incident wave. The results suggest that the S_0 guided wave is more sensitive to the fatigue crack than A_0 guided wave, which is consistent with the findings in previous research **Error! Reference source not found.**.

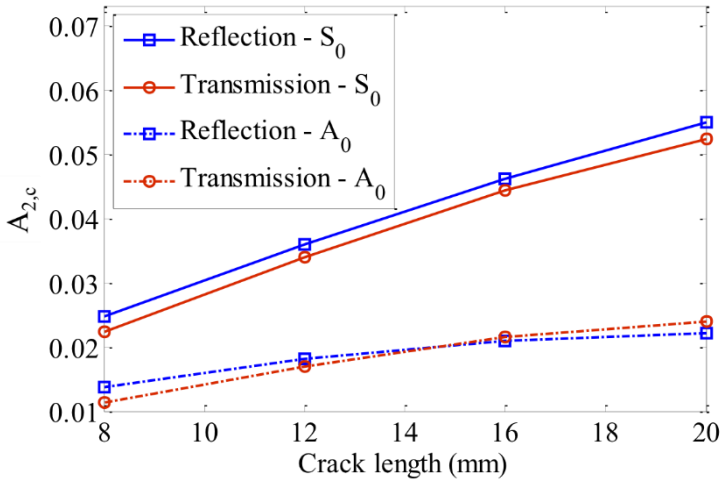

Figure 5-8: Variation of normalised second harmonic with fatigue crack length for Scenario 1: the model with fatigue crack only (A2,c)

5.4.2. Scenario 2

For the Scenario 2, both fatigue crack and debonding are modelled, and the length of both of them increase simultaneously. Figure 5-9 shows that the value of $A_{2,c+d}$ for the reflected and transmitted wave signals increases with the fatigue crack and debonding length when S_0 and A_0 guided wave is used as incident wave, respectively. For transmitted wave, the value of $A_{2,c+d}$ for the case of using A_0 incident wave is higher than that of using S_0 incident wave. However, the value of $A_{2,c+d}$ for using S_0 incident wave is higher than that of using A_0 incident wave in the case of reflected wave. The ratio of $A_{2,c+d}$ to $A_{2,c}$ is also shown in Figure 5-10, which shows the difference of the second harmonic amplitude between the model with both crack and debonding, and crack only. Figure 5-10 shows that when S_0 incident wave is used, the value of $A_{2,c+d}$ is about four times higher than $A_{2,c}$ when both fatigue crack and debonding are existed in the model. There are two reasons that the value of $A_{2,c+d}$ is larger than the $A_{2,c}$. Firstly, it can be due to the frictional contact between debonding interfaces induced by S_0 guided wave. Secondly, compared with the results of Scenario 1, when there is no debonding, the interaction of the crack interfaces is restricted by the composite patches. However, this restriction is released when the composite patches are debonded. In contrast, when A_0 guided wave is used, the $A_{2,c+d}/A_{2,c}$ ratio increases more significantly when the damage length increases, and the $A_{2,c+d}/A_{2,c}$ ratio of the transmitted wave is larger than that of reflected wave. The observations from Figure 5-9 and 5-10 indicate that A_0 guided wave is more sensitive to debonding than S_0

guided wave. The results also show that the second harmonic guided wave induced by debonding are mainly scattered in the wave propagation direction.

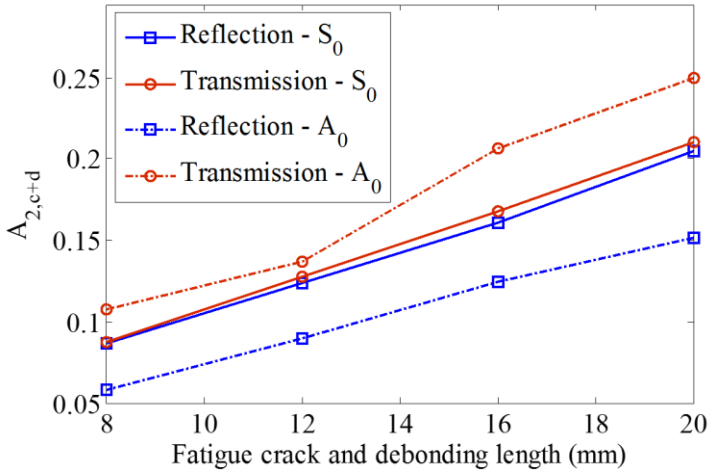

Figure 5-9: Variation of normalised second harmonic with fatigue crack and debonding length on model with fatigue crack and debonding (A2,c+d)

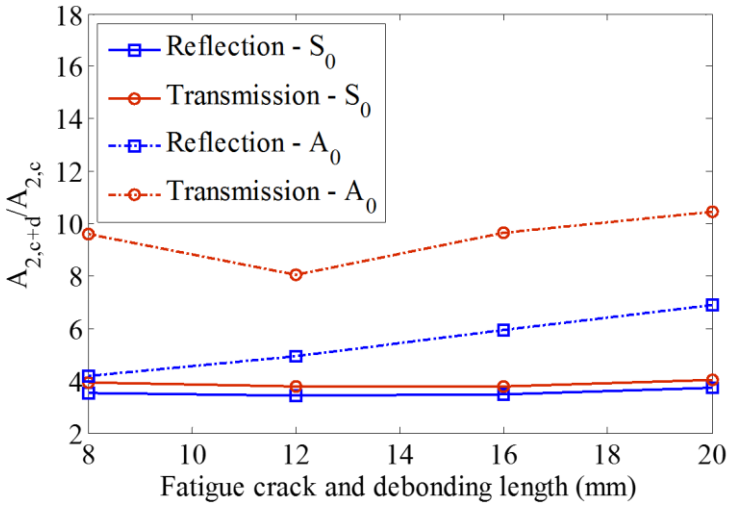

Figure 5-10: Ratio of A2,c+d /A2,c for different fatigue crack and debonding lengths.

5.4.3. Scenario 3

For the Scenario 3, the fatigue crack length is fixed at 8mm and the debonding length increases from 8mm to 20mm. As shown in Figure 5-11, when S_0 incident wave is used, the value of $A_{2,d}$ remains about the same magnitude for both transmitted and reflected wave despite the increase of the debonding length. When A_0 incident wave is used, the value of $A_{2,d}$ in the transmission direction is higher than that when S_0 incident wave is used. For the reflection direction, the $A_{2,d}$

value obtained by using S_0 incident wave is higher than that of using A_0 incident wave. Similar finding was obtained in the work of Soleimanpour *et al*. [32], in which the second harmonic amplitude varies with the delamination length without a clear trend when A_0 incident wave is used. It should be noticed that the second harmonic of the transmitted wave using A_0 incident wave is much higher than that of the reflected wave. Comparing with the results of the model with the fatigue crack only, the ratio between the $A_{2,d}$ and $A_{2,c}$ decreases when A_0 and S_0 incident wave is used, respectively, and the decreasing rate in the transmitted wave of using A_0 incident wave is more obvious (Figure 5-12). Meanwhile, the ratio of using A_0 incident wave is also higher than that of using S_0 incident wave. This is similar to the results of the Scenario 2.

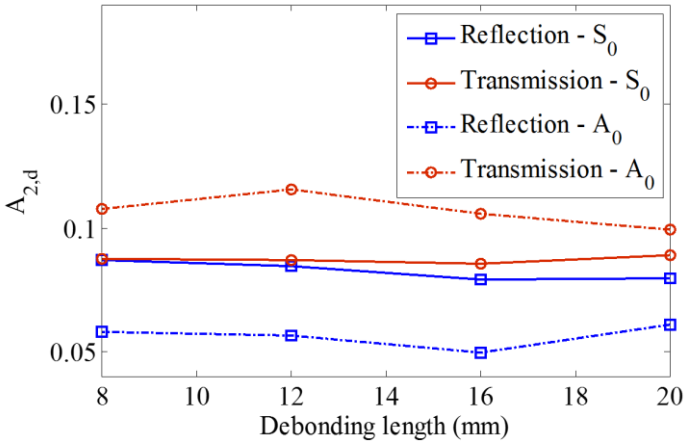

Figure 5-11: Variation of normalised second harmonic with fatigue crack and debonding length for model with both fatigue crack and debonding (A2,d)

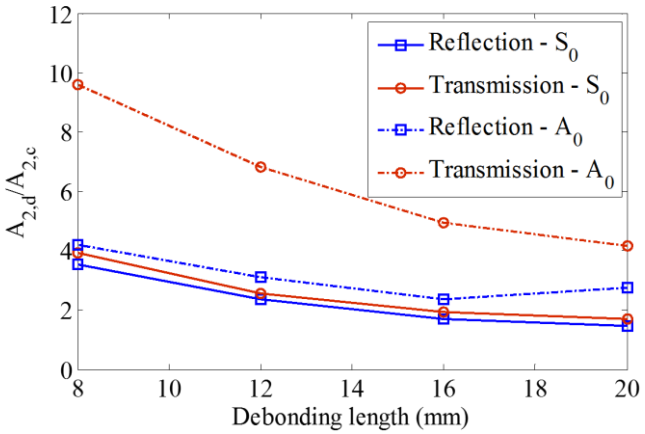

Figure 5-12: Ratios of A2,d /A2,c with different debonding lengths.

5.5. Conclusions

This study has presented an investigation of the second harmonic generation due to guided wave interaction with the crack-induced debonding in the FRP strengthened aluminium plate. In this study, 3D FE simulations have been used to predict the wave propagation and scattering at the crack-induced debonding in the FRP strengthened aluminium plate. Three different damage scenarios, fatigue crack only, both crack and debonding, and debonding with the fixed crack length have been considered. In each damage scenario, a six-cycle 200 kHz S_0 and A_0 incident wave have been used separately to reveal the second harmonic generation due to the contact nonlinearity.

The simulation results have shown that for different damages and different incident wave modes, the second harmonic amplitude variation against the damage length has a unique characteristic. It has been observed that S_0 incident is more sensitive for fatigue crack and A_0 incident wave is more sensitive to debonding. This indicates that normal contact is the major source of nonlinearity contributing the second harmonic generation as compared with the frictional contact. The results have also shown that when A_0 incident wave is used, the second harmonic amplitude is generally larger than that when S_0 incident wave is used for the model with debonding. In addition, when S_0 incident wave is used, the second harmonic amplitude increases only when the length of the fatigue crack increases, while the increase of debonding length will not obviously increase the second harmonic amplitude. For the model with debonding, the second harmonic amplitude of the transmitted wave is larger than that for the reflected wave, especially when A_0 incident wave is used. For the model with the fatigue crack only, the second harmonic amplitude of reflected wave is slightly larger than that of transmitted wave when S_0 incident wave is used.

These findings have shown the potential of using A_0 and S_0 guided wave in detecting and identify the damage, such as debonding or/and fatigue crack, in the FRP strengthened metallic plate. Further work can be carrying out experimental tests to study the practical feasibility of using nonlinear guided wave to detect and distinguish different types of defects in the FRP strengthened metallic plate.

References

[1] Lin CT, Kao PW, Yang FS 1991 *Composites* **22** 135-141

[2] Song SH, Byun YS, Ku TW, Song WJ, Kim J 2010 *J. Mater. Sci. and Technol.* **26** 327-332

[3] Maligno AR, Soutis C, Silberschmidt VV 2013 *Eng. Fract. Mech.* **99** 62-78

[4] Ihn JB and Chang FK 2003 *Smart Mater. Struct.* **13** 621-630

[5] Huang Y, Liu J, Huang X, Zhang J, Yue G 2015 *Int. J. Fatigue* **78** 53-60

[6] Rose JL 2002 *J. Press. Vessel. Technol.* **124**(3) 273-282.

[7] Haynes C and Todd M 2015 *Mech. Syst. Sig. Process.* **54-55** 195-209

[8] He S and Ng CT 2016 *Eng. Struct.* **127** 602-614

[9] Mitra M and Gopalakrishnan S 2016 *Smart Mater. Struct*. **25**(5) 053001

[10] Moreau L, Caleap M, Velichko A, Wilcox P.D 2011 *Wave Motion* **48** 586–602

[11] Rajagopal P and Lowe M 2008 *J. Acoust. Soc. Am.* **124**(5) 2895-2904

[12] He S and Ng CT 2017 *Mech. Syst. Sig. Process.* **84** 324-345

[13] Guo N and Cawley P 1993 *J. Acoust. Soc. Am.* **94**(4) 2240-2246

[14] Michaels TE, Michaels JE, Ruzzene M 2011 *Ultrasonics.* **51** 452-466

[15] Ng CT 2015 *Int. J. Str. Stab. Dyn.* **15** 1540010.

[16] Soleimanpour R and Ng CT 2016 *J. Civil Struct. Health Monit.* **6** 447-459

[17] Eckstein B, Bonet MM, Bach M, Fritzen CP 2017 *Proc. SPIE* **10170** 101701Q

[18] Mohseni H and Ng CT 2017 *Comp. Concrete* **20**(5) 583-593

[19] Quek ST, Tua P, Wang Q 2003 *Smart Mater. Struct.* **12**(3) 447

[20] Flynn EB, Todd MD, Wilcox PD, Drinkwater BW, Croxford AJ 2011 *Proc. R. Soc. A* **467** 2575-2596

[21] Ng CT 2015 *Earthq. Struct*. **8**(4) 821-841

[22] Han JH and Kim YJ 2015 *Mech. Syst. Sig. Process.* **54-55** 336-356

[23] Ng CT 2014 *Struct. Health Monitor.* **13**(4) 359-373

[24] Aryan P, Kotousov A, Ng CT, Cazzolato B 2017 *Struct. Contr. Health Monitor.* **24** e1884

[25] Sohn H. Park HW, Law KH and Farrar CR 2007 *J. Aerospace Eng.* **20** 141-151

[26] Pavlopoulou S, Soutis C, Manson G 2012 *Plast, Rubber and Compos.* **41**(2) 61-68

[27] Puthillath P and Rose JL 2010 *Int. J. Adhesion Adhesives* **30** 566-573

[28] Bermes C, Kim JY, Qu J, Jacobs LJ 2008 *Mech. Syst. Sig. Process.* **22**(3) 638-646

[29] Jhang KY 2009 *Int. J. Precision Eng. Manufacture.* **10**(1) 123-135

[30] He S and Ng CT 2017 *Smart Mater. Struct.* **26** 085002

[31] Hong M, Su Z, Wang Q, Cheng L, Qing X 2014 *Ultrasonics* **54** 770-778

[32] Soleimanpour R, Ng CT, Wang CH 2017 *Struct. Health Monit.* **16**(4) 400-417

[33] Yang Y, Ng CT, Kotousov A, Sohn H, Lim HJ 2018 *Mech. Syst. Sig. Process.* **99** 760-773

[34] Wang Y, Guan R, Lu Y 2017 *Ultrasonics* **80** 87-95

[35] Ng CT and Veidt M 2011 *J. Acoust. Soc. Am.* **129**(3) 1288-1296

[36] Schon J 2003 *Tribol. Int.* **34** 395-404

Chapter 6. Lamb Wave Propagation on Prestressed Plates by Finite Element Modelling

(Paper 5, Manuscript)

Yi Yang[a], Ching-Tai Ng[a], Munawwar Mohabuth[b], Andrei Kotousov[b]

[a] School of Civil, Environmental and Mining Engineering, The University of Adelaide, Adelaide, SA 5005, Australia

[b] School of Mechanical Engineering, The University of Adelaide, Adelaide, SA 5005, Australia

Statement of Authorship

Title of Paper	Finite element prediction of acoustoelastic effect for Lamb wave propagation in prestressed plates
Publication Status	☐ Published ☐ Accepted for Publication ☐ Submitted for Publication ☑ Unpublished and Unsubmitted w ork w ritten in manuscript style
Publication Details	Yang, Y., Ng, C., Mohabuth M., & Kotousov, A. (2019). Finite element prediction of acoustoelastic effect for Lamb wave propagation in prestressed plates.

Principal Author

Name of Principal Author (Candidate)	Yi Yang		
Contribution to the Paper	Undertook literature review, developed theoretical formulation of subroutine and code of subroutine, prepared manuscript		
Overall percentage (%)	80%		
Certification:	This paper reports on original research I conducted during the period of my Higher Degree by Research candidature and is not subject to any obligations or contractual agreements with a third party that would constrain its inclusion in this thesis. I am the primary author of this paper.		
Signature		Date	11/01/2019

Co-Author Contributions

By signing the Statement of Authorship, each author certifies that:

i. the candidate's stated contribution to the publication is accurate (as detailed above);

ii. permission is granted for the candidate in include the publication in the thesis; and

iii. the sum of all co-author contributions is equal to 100% less the candidate's stated contribution.

Name of Co-Author	Ching-Tai Ng		
Contribution to the Paper	Helped numerical model development, helped review manuscript and prepare for submission, and acted as corresponding author.		
Signature		Date	11/1/2019

Name of Co-Author	Andrei Kotousov		
Contribution to the Paper	Helped develop analytical solution for comparison to verify the finite element model.		
Signature		Date	4/1/2019

Name of Co-Author	Munawwar Mohabuth		
Contribution to the Paper	Helped numerical model development and evaluate and edit the manuscript.		
Signature		Date	11/01/2019

Please cut and paste additional co-author panels here as required.

Abstract

The study presents a finite element (FE) prediction of acoustoelastic effect of Lamb wave propagation in pre-stressed plates. A three-dimensional (3D) FE model is developed to incorporate the acoustoelastic effect in simulating Lamb wave in plates subjected to different levels and types of stresses. The change of phase velocity due to axial stresses is obtained with the consideration of different stress magnitudes, biaxial stress ratios and wave propagation angles. Good agreement is found between the FE prediction and analytical results. A series of numerical case studies are also carried out to investigate the effect of bending stress. The study proves the feasibility of using the FE simulation to predict the acoustoelastic effect of Lamb wave propagation on pre-stressed plates for cases that do not have analytical results. This demonstrates the importance of incorporating the acoustoelastic formulation in the 3D FE simulation.

Keywords: Acoustoelasticity, Lamb wave, pre-stressed plate, finite element, finite deformation

6.1. Introduction

6.1.1. Structural Health Monitoring using guided waves

Structural health monitoring (SHM) has attracted significant attention in last two decades. Different damage detection methods were developed in the literature [1]-[4]. In particular, ultrasonic guided wave has proved to be one of the promising approaches for detecting damage [5]-[8]. Different types of waves have been investigated, such as Lamb wave [9], [10] and Rayleigh wave [11]-[13]. In the literature, the studies have focused on fundamental understanding of guided wave propagation and scattering at damage [14]-[16], and developing damage detection techniques using guided waves [17]-[20]. In particular, Lamb wave is one of the focuses in these studies, which is a special type of ultrasonic guided wave. Lamb wave can propagate in thin-walled structures with traction-free surface conditions, and travel at relatively long distance with very little energy loss. A number of studies were carried out to investigate the feasibility and sensitivity of using guided wave in damage detection for different types of structures, for example, beam [21],[22], plate [23],[24], pipe [25],[26] and concrete. The findings show that Lamb wave has potential to provide new opportunities for cost-effective safety inspection of structures [28],[29].

In the last decade, a wide range of damage detection techniques was developed using Lamb wave. In general, these methods rely on comparing the current data with a reference data to extract the damage information for damage detection and identification [30],[31]. However, the varying environmental and operational conditions [32],[33], such as temperature and loading condition change, usually mask the signal changes caused by the damage [34]. This limits the transition of the damage detection techniques to real-world applications. In the literature, a number of techniques were developed to compensate the error due to variation in temperature and loading conditions [35],[36]. Alternatively, some studies investigated the nonlinear guided wave in the damage detection to address this issue [37]-[39].

One fundamental solution to this issue is to investigate and quantify the effect of these varying conditions on Lamb wave propagation. The focus of the current paper is on the effect of variations in applied or thermally induced stresses on Lamb wave propagation, which is comparable to the effect of moderate temperature fluctuation. The next subsection will provide a brief review on the existing developments related to acoustoelastic effect of the Lamb wave propagation in prestressed plates.

6.1.2. Acoustoelastic effect of Lamb wave propagation

Acoustoelastic effect is known as the effect of stress on the wave propagation in a pre-stressed media. It has been studied since the development of the finite deformation theory by Murnaghan [40], who formulated the material nonlinearity using third order elastic constants. Some pioneering studies in this area include the research of Hughes and Kelly [41], who derived equations relating the wave velocity to the applied stress and also experimentally measured the acoustoelastic effect. The other study of Egle and Bray [42] measured the acoustoelasticity and showed how to obtain higher-order elastic constants from the experiment data.

In the literature, many developments and studies based on the theory of acoustoelasticity mainly focused on bulk waves (Pau and Scalea [43]). The acoustoelastic effect is usually quantified by measuring the velocity change of the propagating wave on the nonlinear media. However, the velocity change of ultrasonic bulk wave due to applied stress is small (Mohabuth *et al*. [44]). In recent years, guided waves have attracted increasing research interests due to its high sensitivity to micro changes of material properties and ability to propagate over long distance. Gandhi *et al.* [45] provided a comprehensive analysis of the acoustoelastic effect due to biaxial loading through analytical formulation and experimental measurements. However, their work only considered the first order in the infinitesimal strain tensor. In a more recent study by Mohabuth *et al*. [44], they developed the governing equation for the propagation of small amplitude waves in a pre-stressed plate using the theory of incremental deformations superimposed on large deformation. The development was extended to estimate the effect of applied or thermally-induced stresses on the Lamb wave propagation [46]. In similar time, Packo *et al*. [47] studied the dispersion of finite amplitude Lamb wave on nonlinear plates with the consideration of up to fourth order elastic constants.

Analysis of geometrically complicated structures or structures subjected to complex loadings using analytical approach is infeasible. Previous theoretical studies focused on acoustoelastic effect of Lamb wave propagation in plates were all based on analytical approach and these studies only focused on simple structures or structures subjected to simple loadings. It is important to develop a numerical approach so that the study of acoustoelastic effect on Lamb wave propagation is extendable to complicated situations. It is possible to simulate the acoustoelastic effect using FE simulation, by which different complex structures or structures subjected to complex loadings can be modelled and investigated.

In the current study, a material subroutine is developed in ABAQUS based on Murnaghan's energy function [40] to model the phase velocity change due to applied stress. The FE model is then validated by comparing the simulation results with the analytical results obtained by Mohabuth *et al*. [44]. The validated FE model is then used to predict the acoustoelastic effect of Lamb wave propagation in the pre-stressed plate. The study could contribute the development of practical damage detection techniques using Lamb wave.

The current paper is structured as follows. In Section 2, a theoretical basis of the acoustoelastic effect of Lamb wave is elaborated, followed by a derivation of the constitutive equation to develop the material nonlinearity in ABAQUS VUMAT in Section 3. Then, the FE model with nonlinear material is developed in Section 4, and the simulation results of the FE model is validated by comparing them with the theoretical solutions obtained from previous studies. A series of case studies is then carried out using the validated FE model in Section 5, which considers the acoustoelastic effect of Lamb wave on a plate under bending. Finally, conclusions are drawn in Section 6.

6.2. Governing equations for acoustoelastic Lamb wave propagation

According to Mohabuth *et al*. [44], the position of the material particle in the reference (β_r) and current (β_0) configurations is denoted by $\boldsymbol{X}$ and $\boldsymbol{x}$, respectively. The deformation gradient **F** is defined by

$$\mathbf{F} = \frac{\partial \mathbf{x}}{\partial \mathbf{X}} \tag{1}$$

The nominal and Cauchy stress tensors are given by

$$\mathbf{S} = \frac{\partial W}{\partial \mathrm{F}}, \boldsymbol{\sigma} = J^{-1}\mathrm{F}\frac{\partial W}{\partial \mathrm{F}} \tag{2}$$

where W is the strain energy function and $J = \det\mathbf{F}$. In the study of Mohabuth *et al*. [44], the strain energy function is defined by deformation gradient. The corresponding incremental constitutive equation of the stress tensor is given in component form by

$$\hat{\mathrm{S}}_{0_{\mathrm{pi}}} = \mathrm{A}_{0_{\mathrm{piqj}}} u_{\mathrm{j,q}} \tag{3}$$

where $\hat{\mathrm{S}}_{0_{\mathrm{pi}}}$ are the components of the incremental nominal stress tensor. $\mathrm{A}_{0_{\mathrm{piqj}}}$ are the components of the fourth-order elasticity tensor of instantaneous elastic moduli [44], [45]. u is

the displacement vector relative to β_0, and a comma indicates partial differentiation with respect to Eulerian coordinates.

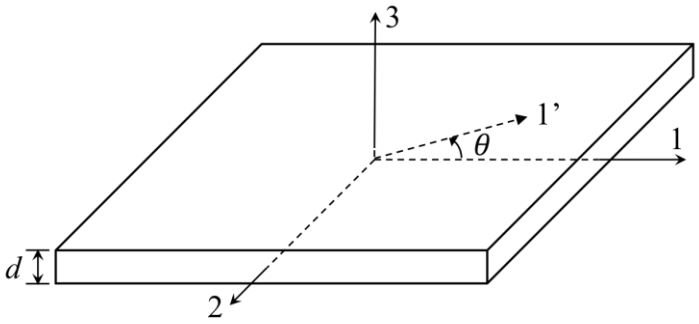

Figure 6-1: Cartesian coordinate system defined in the mid-plane of the plate with stresses applied in axes 1 and 2 direction and Lamb wave propagation in axis 1' direction

As shown in Figure 6-1, consider an isotropic plate with density of ρ defined in a Cartesian coordinate system located at the mid-plane of the plate. The equation of motion in a prestressed plate is given by

$$A_{0piqj}\,\frac{\partial^2 u_j}{\partial x_p \partial x_q} = \rho \frac{\partial^2 u_i}{\partial t^2} \tag{4}$$

When considering a Lamb wave propagating along axis 1' direction with an angle of θ, the equation of motion can be transformed to the rotated coordinate system

$$A'_{0piqj}\,\frac{\partial^2 u'_j}{\partial x'_p \partial x'_q} = \rho \frac{\partial^2 u'_i}{\partial t^2} \tag{5}$$

and the relationship between the two elasticity tensors before and after transformation is

$$A'_{0piqj} = \beta_{pr}\beta_{ik}\beta_{qs}\beta_{jl}A_{0rksl} \tag{6}$$

where β_{ij} is the cosine of the angle of rotation. In the following discussions, all the equations are formulated based on the original coordinate system.

The wave motion is assumed as

$$u_j = U_j e^{i\xi(x_1 + \alpha x_3 - ct)} \tag{7}$$

where ξ is the wave number in x_1 direction, c is the phase velocity along x_1 direction, and α is the ratio of x_3 to x_1 wave numbers. Substitute the equation to the equation of motion yields the Christoffel equations

$$\mathrm{K_{ij}U_j} = 0 \tag{8}$$

and the parameters $\mathrm{K_{ij}}$ are given by

$$\begin{aligned}
\mathrm{K_{11}} &= \rho c^2 - \mathrm{A_{01111}} - \alpha^2 A_{01313}, \\
\mathrm{K_{22}} &= \rho c^2 - \mathrm{A_{01212}} - \alpha^2 A_{02323}, \\
\mathrm{K_{33}} &= \rho c^2 - \mathrm{A_{01313}} - \alpha^2 A_{03333}, \\
\mathrm{K_{12}} &= \mathrm{K_{21}} = -\mathrm{A_{01112}} - \alpha^2 A_{01323}, \\
\mathrm{K_{13}} &= \mathrm{K_{31}} = -\alpha(A_{01133} + A_{01331}), \\
\mathrm{K_{23}} &= \mathrm{K_{32}} = -\alpha(A_{01233} + A_{01332}),
\end{aligned} \tag{9}$$

For non-trivial solutions of the displacement amplitude $\mathrm{U_j}$, the determinant of the K matrix goes to zero. This yields a six order equation with six solutions α_q, $\mathrm{q} \in \{1,2,3,4,5,6\}$, which is expressed as

$$\mathrm{P_6}\alpha^6 + \mathrm{P_4}\alpha^4 + \mathrm{P_2}\alpha^2 + \mathrm{P_0} = 0 \tag{10}$$

where the coefficients can be found in **Error! Reference source not found.**. To satisfy the tress-free boundary condition, the approach developed in the work of Nayfeh and Chimenti **Error! Reference source not found.**, and the displacement ratios between $\mathrm{U_2}$ to $\mathrm{U_1}$ and $\mathrm{U_3}$ to U1 are defined

$$\mathrm{V_q} = \frac{\mathrm{U_{2q}}}{\mathrm{U_{1q}}},\ \mathrm{W_q} = \frac{\mathrm{U_{3q}}}{\mathrm{U_{1q}}} \tag{11}$$

The expansion of V_q and W_q can also be found in the work of Nayfeh and Chimenti **Error! eference source not found.**. With the displacement ratios, the displacement filed of the Lamb waves can be written as

$$\begin{aligned}
\mathrm{u_1} &= \textstyle\sum_{q=1}^{6} \mathrm{U_{1q}} e^{\mathrm{i}\xi(\mathbf{x_1} + \boldsymbol{\alpha_q} \mathbf{x_3} - \mathbf{ct})}, \\
\mathrm{u_2} &= \textstyle\sum_{q=1}^{6} V_q \mathrm{U_{1q}} e^{\mathrm{i}\xi(\mathbf{x_1} + \boldsymbol{\alpha_q} \mathbf{x_3} - \mathbf{ct})}, \\
\mathrm{u_3} &= \textstyle\sum_{q=1}^{6} W_q \mathrm{U_{1q}} e^{\mathrm{i}\xi(\mathbf{x_1} + \boldsymbol{\alpha_q} \mathbf{x_3} - \mathbf{ct})},
\end{aligned} \tag{12}$$

Substitute the displacement relations to equation (3), gives the expression for stresses in 3 direction

$$\hat{S}_{33} = \sum_{q=1}^{6} i\xi D_{1q} U_{1q} e^{i\xi(x_1+\alpha_q x_3-ct)},$$

$$\hat{S}_{13} = \sum_{q=1}^{6} i\xi D_{2q} U_{1q} e^{i\xi(x_1+\alpha_q x_3-ct)},$$

$$\hat{S}_{23} = \sum_{q=1}^{6} i\xi D_{3q} U_{1q} e^{i\xi(x_1+\alpha_q x_3-ct)}, \quad (13)$$

where the coefficients D_{1q}, D_{2q} and D_{3q} are defined with the elasticity tensor and displacement ratios **Error! Reference source not found.**. For the stress-free condition at the upper (d/2) and ower (-d/2) surfaces of the plate, there are six equations in terms of the amplitudes U_{11}, U_{12}, …, U_{16}, and the determinant is

$$\begin{vmatrix} D_{11}E_1 & D_{12}E_2 & D_{13}E_3 & D_{14}E_4 & D_{15}E_5 & D_{16}E_6 \\ D_{21}E_1 & D_{22}E_2 & D_{23}E_3 & D_{24}E_4 & D_{25}E_5 & D_{26}E_6 \\ D_{31}E_1 & D_{32}E_2 & D_{33}E_3 & D_{34}E_4 & D_{35}E_5 & D_{36}E_6 \\ D_{11}\hat{E}_1 & D_{12}\hat{E}_2 & D_{13}\hat{E}_3 & D_{14}\hat{E}_4 & D_{15}\hat{E}_5 & D_{16}\hat{E}_6 \\ D_{21}\hat{E}_1 & D_{22}\hat{E}_2 & D_{23}\hat{E}_3 & D_{24}\hat{E}_4 & D_{25}\hat{E}_5 & D_{26}\hat{E}_6 \\ D_{31}\hat{E}_1 & D_{32}\hat{E}_2 & D_{33}\hat{E}_3 & D_{34}\hat{E}_4 & D_{35}\hat{E}_5 & D_{36}\hat{E}_6 \end{vmatrix} = 0 \quad (14)$$

where $\hat{E}_q = E_q^{-1} = e^{-i\xi\alpha_q\frac{d}{2}}$. The determinant leads to two uncoupled characteristic equation

$$D_{11}G_1 \cot(\gamma\alpha_1) - D_{13}G_3 \cot(\gamma\alpha_3) + D_{15}G_5 \cot(\gamma\alpha_5) = 0,$$

$$D_{11}G_1 \tan(\gamma\alpha_1) - D_{13}G_3 \tan(\gamma\alpha_3) + D_{15}G_5 \tan(\gamma\alpha_5) = 0, \quad (15)$$

corresponding to symmetric and anti-symmetric Lamb wave modes, respectively, and $\gamma = \xi d/2 = \omega d/2c$. The parameters G_i are provided in **Error! Reference source not found.**. Consequently, with the elasticity tensor defined through nonlinear energy function and equation (15), the dispersion relation of Lamb wave can be obtained.

6.3. Finite element modelling of acoustoelastic effect

In ABAQUS/Explicit, VUMAT can be used to define the mechanical constitutive behaviour based on the nonlinear strain energy function of Murnaghan [40], which is written as:

$$W(\mathbf{E}) = \frac{1}{2}(\lambda+2\mu)i_1^2 - 2\mu i_2 + \frac{1}{3}(l+m)i_1^2 - 2mi_1i_2 + ni_3 \quad (16)$$

where λ and μ are the lamé elastic constants; *l*, *m* and *n* are the third order elastic constants. $i_1 = tr\mathbf{E}$, $i_2 = \frac{1}{2}[i_1^2 - tr(\mathbf{E})^2]$, $i_3 = det\mathbf{E}$, respectively. **E** is the Green-Lagrange strain tensor given by:

$$\mathbf{E} = \frac{1}{2}(\mathbf{C} - \mathbf{I}) \tag{17}$$

where **I** is the identity tensor and **C** is the right Cauchy-Green deformation tensor, defined as:

$$\mathbf{C} = \mathbf{F}^{\mathrm{T}}\mathbf{F} = \mathbf{U}^{\mathbf{2}} \tag{18}$$

where **U** is the right stretch tensor.

In ABAQUS, the stress in VUMAT of ABAQUS/Explicit is the Cauchy stress tensor in Green-Naghdi basis,

$$\widehat{\boldsymbol{\sigma}} = \mathbf{R}^{\mathrm{T}}\boldsymbol{\sigma}\mathbf{R} \tag{19}$$

where **R** is rotation tensor, and R is a proper orthogonal tensor, i.e., $\mathbf{R}^{-1} = \mathbf{R}^{\mathrm{T}}$. The relationship between **F**, **U** and **R** is given by

$$\mathbf{F} = \mathbf{RU} \tag{20}$$

So, equation (19), with the energy function presented in equation (16) can be translated to,

$$\widehat{\boldsymbol{\sigma}} = \mathrm{J}^{-1}\mathbf{R}^{\mathrm{T}}\mathbf{F}\mathbf{T}\mathbf{F}^{\mathrm{T}}\mathbf{R} = \mathrm{J}^{-1}\mathbf{R}^{\mathrm{T}}\mathbf{R}\mathbf{U}\mathbf{T}\mathbf{U}^{\mathrm{T}}\mathbf{R}^{\mathrm{T}}\mathbf{R} = \mathrm{J}^{-1}\mathbf{U}\frac{\partial W(\mathbf{E})}{\partial \mathbf{E}}\mathbf{U}^{\mathrm{T}} \tag{21}$$

where **T** is the second Piola-Kirchhoff (PK2) stress. The stress in VUMAT must be updated with the equation at the end $(t + \Delta t)$ of an integration step and stored in stressNew(i), based on the values of F and U given in the subroutine at the end of previous step (t).

6.4. Numerical Case Studies

6.4.1. 3D Finite Element Model

A 3D FE model of a 6061-T6 aluminium plate was created in ABAQUS and wave propagation problem was solved by explicit integration approach [49]. The material properties of the 6061-T6 aluminium are shown in Table 6-1. The thickness of the plate is 3.2mm and the in-plane dimension is 240mm×240mm. The element type used in the model is the 8-node linear brick with reduced integration, and hourglass control (C3D8R). The in-plane dimension of an element is 0.25×0.25mm^2 to ensure that there are at least 20 elements per wavelength. There

are 10 elements in the thickness direction, and hence, the thickness of each element is 0.32mm. To reduce the computational cost, only a quarter of the plate (120mm×120mm) is modelled using symmetric boundary conditions due to the symmetric nature of the model (Figure 6-2).

As shown in Figure 6-2, biaxial stresses are applied to the plate, which are defined as σ_1 and σ_2, with

$$\sigma_2 = \lambda\sigma_1 \tag{22}$$

where λ defines the biaxial stress ratio. In this study, quasi-static loading with a duration of 2ms is used to apply the initial stress on the plate to minimise transient effect due to the loading process on the propagating wave signals in the later step. After the plate is stressed, the fundamental symmetric mode (S_0) of Lamb wave is excited by applying in-plane nodal displacement to nodes at the circumference of a quarter of10mm diameter circle located at the bottom right of the modelled quarter plate. The excitation is a 250kHz 4-cycle narrow-band sinusoidal tone burst pulse modulated by a Hanning window. The measurements are taken in five different directions, i.e., 0°, 22.5°, 45°, 67.5° and 90°. There are six measurement points in each direction as shown in Figure 6-2. The first measurement point is 30mm away from the excitation, and all the five points are equally spaced at 4mm. In this study, pure S_0 mode is excited to validate the FE model.

Table 6-1: Material properties of 6061-T6 aluminium [48]

λ (GPa)	μ (GPa)	l (GPa)	m (GPa)	n (GPa)	Density (kg/m^3)
54.3	27.2	-281.5	-339.0	-416.0	2704

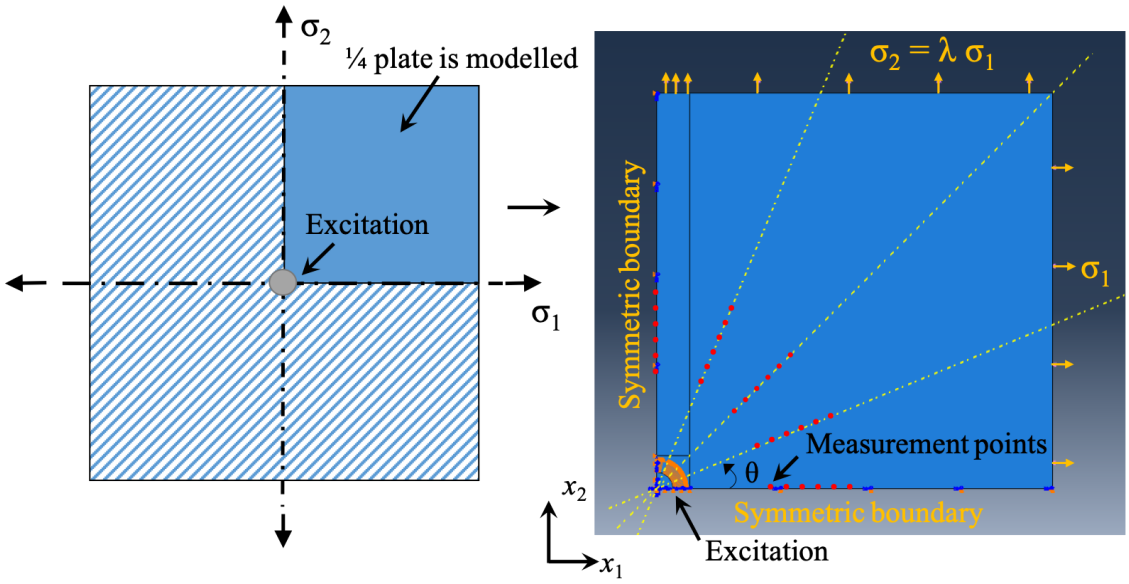

Figure 6-2: Schematic diagram of the FE model with applied stresses

6.4.2. Plate with applied biaxial stresses

Figure 6-3 shows the time domain signal of the excited Lamb wave propagate in θ = 0° direction for the FE model with nonlinear material defined in VUMAT and linear material defined without using material subroutine, respectively. It can be seen that for the results obtained from nonlinear material model, there is a clear shift of the peak of the Lamb wave signal when the plate is under an 80MPa biaxial tension. In contrast, for the wave signals obtained from linear material model, there is no shift of the peak no matter the model is loaded or not.

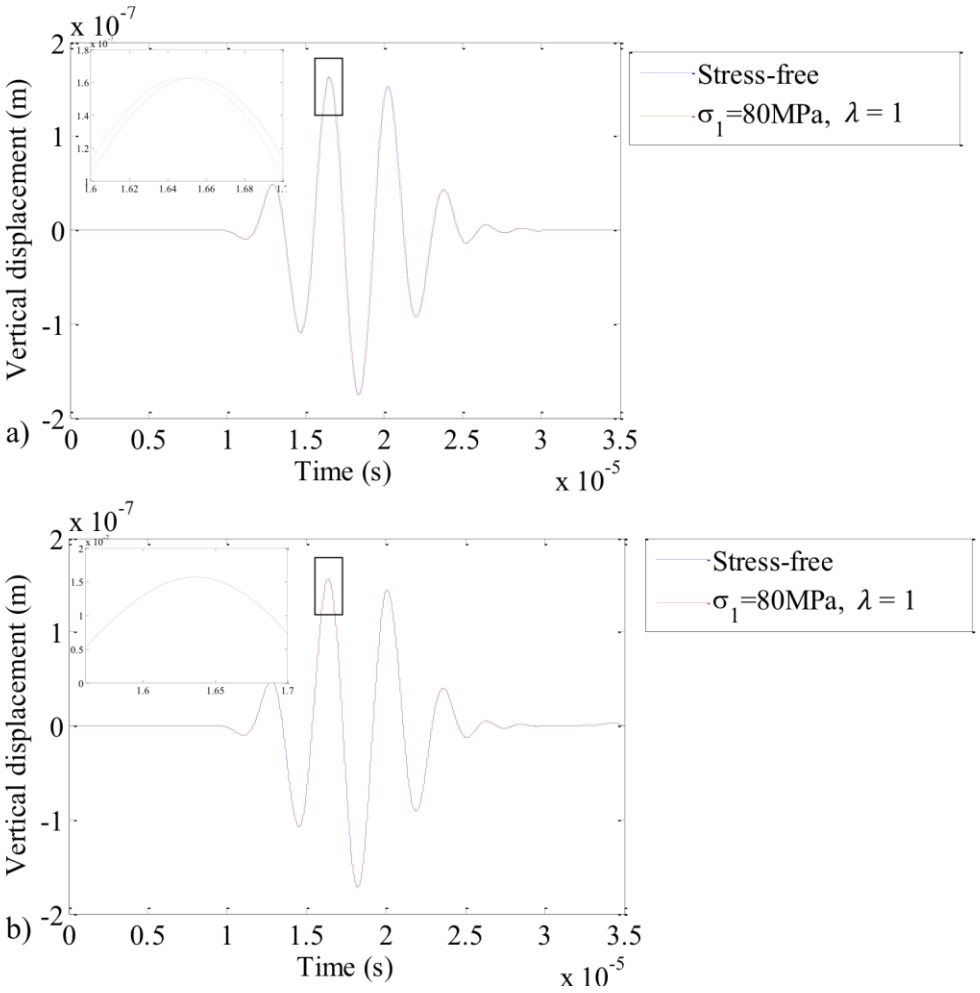

Figure 6-3: FE simulated Lamb wave signal at θ = 0° propagation direction in a plate with a) nonlinear material properties and b) linear material properties.

The signals of the Lamb wave propagation are measured in different wave propagation directions (θ). Using the measured signals, the phase velocity can be calculated by

$$C_p = \frac{2\pi f d}{\Delta\phi} \tag{23}$$

where C_p is the phase velocity, f is the excitation frequency, d is the distance between two adjacent measurement points and $\Delta\phi$ is the phase change between the two points. In this study, as the plate undergoes in-plane deformation due to pre-stress, the distance d used for the formula is the distance after deformation. Five phase velocities are calculated in each direction using signals measured at six measurement points, and the averaged velocity is calculated. The effect of the plate thickness change due to the stress effect is not considered as the change of thickness is very small and its influence on phase velocity is negligible.

The dispersive nature of Lamb wave simulated in FE model can introduce some errors to the velocity calculated from the FE model based on the time-windowed data of the calculated wave signals. According to the dispersion curve of the 6061-T61 aluminium (Figure 6-4), the excitation frequency used in the simulation is chosen in a region having relatively flat phase velocity so that the dispersive effect can be minimised. For the fundamental anti-symmetric mode (A_0) of Lamb wave at low frequency region (< 500kHz) and S_0 Lamb wave at frequency region of 500 – 1000kHz, as well as the higher order anti-symmetric and symmetric modes Lamb wave, they are very dispersive. In this study, the excitation signal has a larger number of cycles to reduce the frequency bandwidth so that the phase velocity change can be estimated accurately.

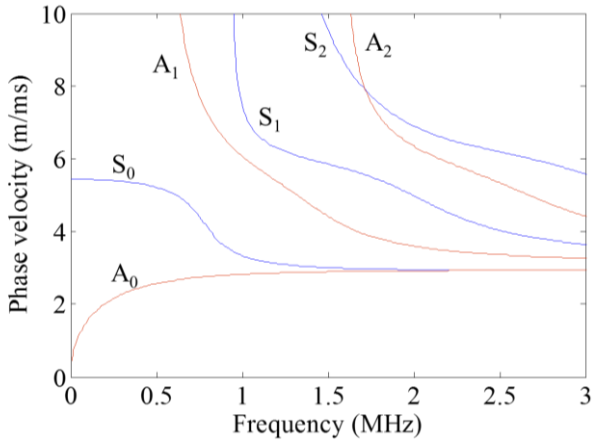

Figure 6-4: Phase velocity dispersion curve of 6061-T6 Aluminium

Four cases are used to validate the accuracy of the 3D FE model with the material nonlinearity. Case 1 investigates the effect of stress ratio λ, in which different values of λ are considered and σ_1 = 80MPa. Case 2 investigates the effect of stress magnitude, in which σ_1 = 80MPa and λ = -0.5 and -1. Case 3 studies the effect of wave propagation angle, in which σ_1 = 0MPa, 20MPa, 40MPa, 60MPa and 80MPa and λ = -1, -0.5, 0, 0.5 and 1. Case 4 analyses the effect of wave excitation frequency, in which the considered excitation frequency 200kHz (*fd* = 640kHz-mm) is different to the excitation frequencies considered in Cases 1 – 3 with different stress ratios λ and σ_1 =80MPa . Table 6-2 is a summary of these cases.

Table 6-2: Summary numerical case studies of biaxial stresses

	Investigation	σ_1 (MPa)	σ_2 (MPa)	λ	Excitation frequency
Case 1	Biaxial stress ratio λ effect	80	-80, -40, 0, 40, 80	-1,-0.5,0,0.5,1	250kHz
Case 2	Stress magnitude effect	0,20,40,60,80	0,-20,-40,-60,-80	-1	250kHz
		0,20,40,60,80	0,-10,-20,-30,-40	-0.5	250kHz
Case 3	Wave propagation angle effect	80	-80,-40,0,40,80	-1,-0.5,0,0.5,1	250kHz
Case 4	Wave excitation frequency effect	80	-80-40,0,-40,80	-1,-0.5,0,0.5,1	200kHz

In Case 1, the value of σ_2 is fixed at 80MPa while the values of σ_1 are -80MPa, -40MPa, 0MPa, 40MPa and 80MPa. The corresponding biaxial stress ratios λ are -1, -0.5, 0, 0.5 and 1. Figure 6-5 shows the results of the phase velocity change against different values of biaxial stress ratio λ. The analytical solutions calculated based on the equations developed in [44] and the 3D FE simulation results are shown in Figure 6-5: Phase velocity change for different values of stress ratio λ with fd = 800kHz-mm, σ1 = 80MPa, in which they are presented by solid and dash-dotted lines, respectively. There is very good agreement between the analytical solutions and FE simulation results in all wave propagation angles ($\theta = 0°, 22.5°, 45°, 67.5^\circ$ and 90°). The results also show that the phase velocity change has a linear relationship with the biaxial stress ratios. It should be noted that when the biaxial stress ratio λ = 1, the phase velocity changes in all propagation directions are all negative with the same magnitude. In comparison, when λ = -1, there is no velocity change in 45^o direction, and for propagation directions in 22.5^o and 67.5^o, as well as 0^o and 90^o, the magnitude of velocity changes are the same but in opposite signs. It can be seen that, when λ is changed from -1 to 1, phase velocity change in 90^o propagation direction experiences the largest variation, while in 22.5^o direction the variation is trivial as compared with those in all other directions.

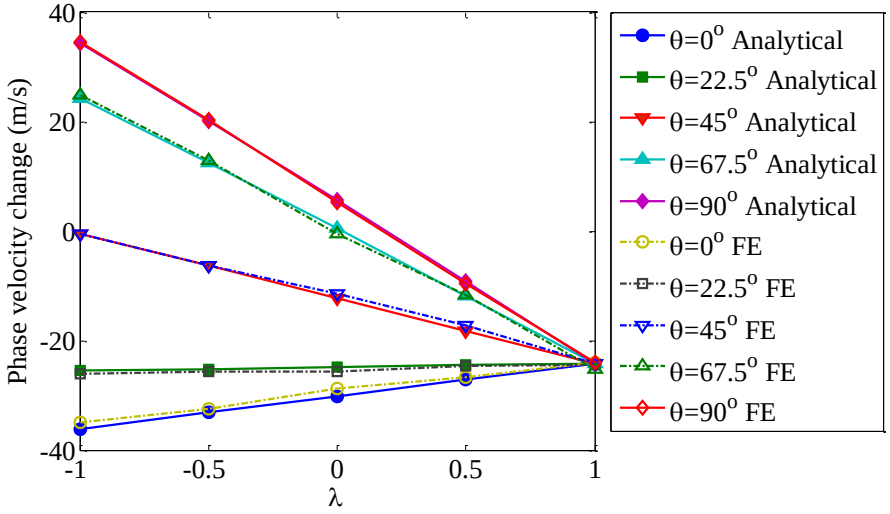

Figure 6-5: Phase velocity change for different values of stress ratio λ with fd = 800kHz-mm, σ1 = 80MPa

Figure 6-6 and Figure 6-7show the effect of the stress magnitude on the phase velocity change of the S_0 Lamb wave. The values of σ_1 considered in Case 2 are 0MPa, 20MPa, 40MPa, 60MPa and 80MPa, and the biaxial stress ratios λ are -1 and -0.5. This means that the σ_2 are 0MPa, -20MPa, -40MPa, -60MPa and -80MPa for λ = -1 as shown in Figure 6, and 0MPa, -10MPa, -20MPa, -30MPa and -40MPa for λ = -0.5 as shown in Figure 6-7: Phase velocity change for different stress levels with fd = 800kHz-mm, λ = -0.5. The same as Figure 6-5, there is very good agreement between the analytical solutions and FE simulation results in Figure 6-6 and Figure 6-7. Figure 6-6 considers the stresses adding in x_1 and x_2 direction are of the same magnitude (λ = -1). Therefore, the values of the phase velocity change are the same in $\theta = 0°$ and 90°, and $\theta = 22.5°$ and 67.5°, respectively, but they are in opposite sign. There is no change in the phase velocity for $\theta = 45°$ regardless the changes in the applied stress. Different to Figure 6-6, Figure 6-7 considers λ = -0.5. The phase velocity change in $\theta = 45°$ is no longer equal to zero when biaxial stress is applied on the plate. Also, the values of the phase velocity change for wave propagation at $\theta < 45°$ are larger than those at $\theta > 45°$. This is because the stress value in x_1 direction is always larger than x_2 in Case 2.

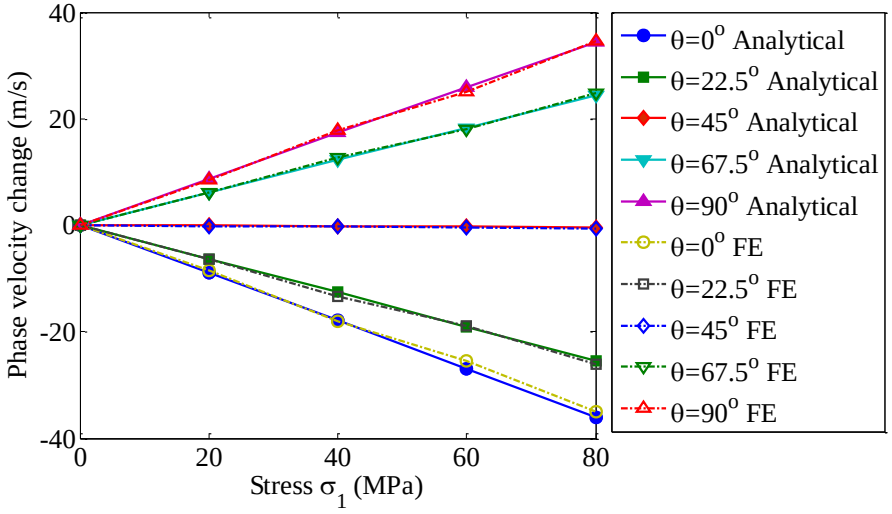

Figure 6-6: Phase velocity change for different stress levels with fd = 800kHz-mm, λ = -1

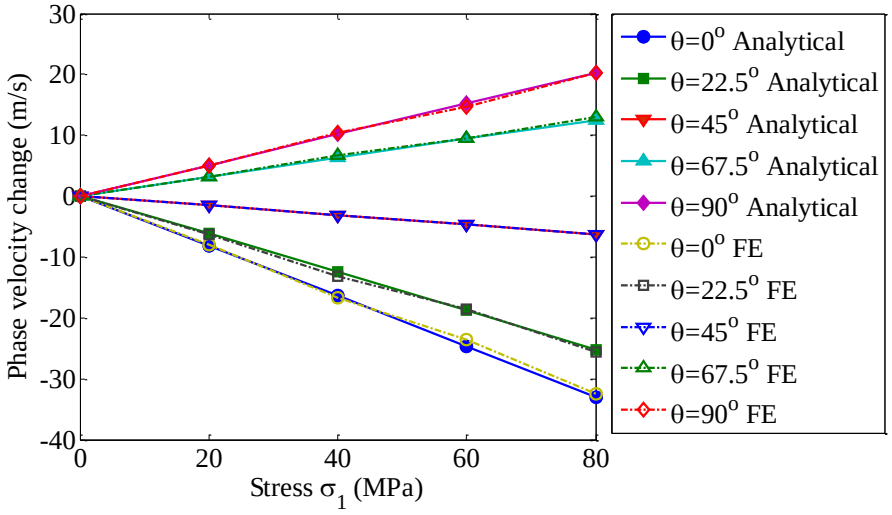

Figure 6-7: Phase velocity change for different stress levels with fd = 800kHz-mm, λ = -0.5

Figure 6-8 shows the phase velocity change in relation to the wave propagation angle. The wave propagation angles considered are $\theta = 0°, 22.5°, 45°, 67.5°$ and 90°. Biaxial ratios λ = -1, -0.5, 0 , 0.5 and 1 while σ_1 = 80MPa are considered in Case 3. As shown in Figure 6-8, it is found that the phase velocity changes are always the same for different biaxial stress ratios when the propagation angle roughly is equal to 22.5°. When λ = 1, the phase velocity is the same for all wave propagation angle. Figure 6-9 shows the results of Case 4, in which are setting are the same, expect the excitation frequency is 200kHz. The phenomena of the phase velocity change in relation to the wave propagation angle and biaxial stress ratio are very

similar. The results in Figure 6-8 and Figure 6-9 show that there is good agreement between the analytical solutions and FE simulation results.

Overall, the FE simulation results from the model with material subroutine matches very well with the analytical results in all cases. It can be observed that the tensile stress reduces the phase velocity while the compressional stress increases the phase velocity of the S_0 Lamb wave. The phase velocity changes in different cases with different loads, propagation angles and stress ratios are quite different.

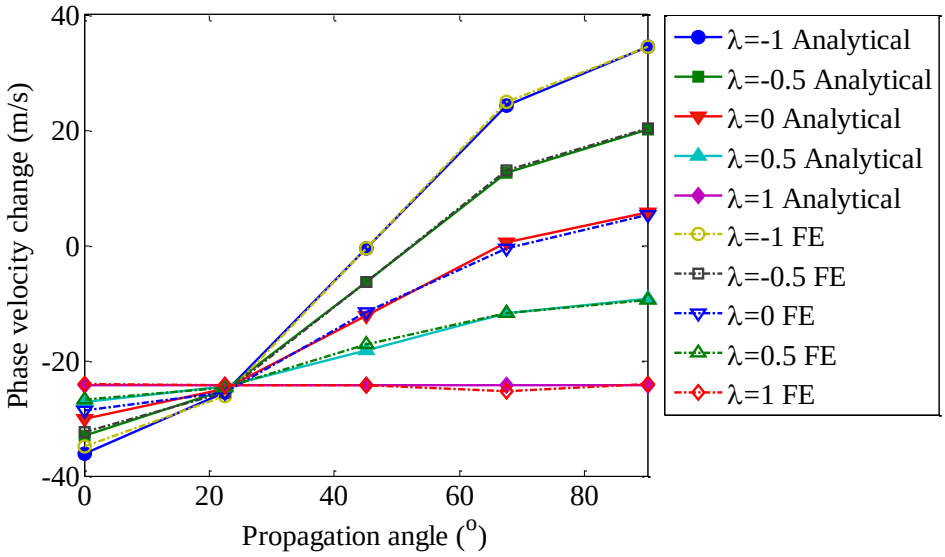

Figure 6-8: Phase velocity change for different wave propagation directions with fd = 800kHz-mm, σ_1 = 80MPa

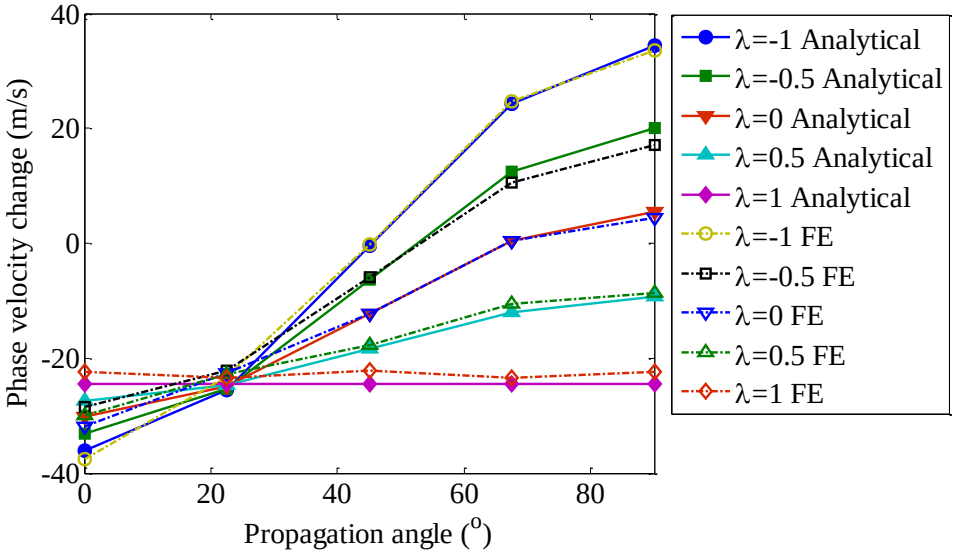

Figure 6-9: Phase velocity change for different wave propagation directions with fd = 640kHz-mm, σ_1 = 80MPa

6.5. Acoustoelastic effect of Lamb wave propagation under bending stress

6.5.1. Modeshape of Lamb wave under applied bending stress

A 2D plane strain model is first developed in ABAQUS to investigate the variation of the modeshape of S_0 Lamb wave propagation on a plate under a bending stress. The dimension of the plate is 1000mm long by 3.2mm thick. 4-node bilinear plane strain quadrilateral elements are used with reduced integration and hourglass control (CPE4R). The element size is 0.25mm in length and 0.32mm in depth to ensure there are at least 10 elements in the thickness direction and 20 elements per wavelength. The excitation is a 250kHz 4-cycle narrow-band sinusoidal tone burst pulse modulated by a Hanning window. The S_0 Lamb wave is excited at the middle of the plate. The bending stress is applied at both ends of the plate and varies linearly through the plate thickness. The material nonlinearity sub-routine is modified to accommodate the 2D plane strain condition. The measurement location is at 400mm away from the excitation location. At this location, both in-plane and out-of-plane displacements of the nodal points located along the plate thickness are calculated for the plate at stress free condition and the under a maximal bending stress of 80MPa.

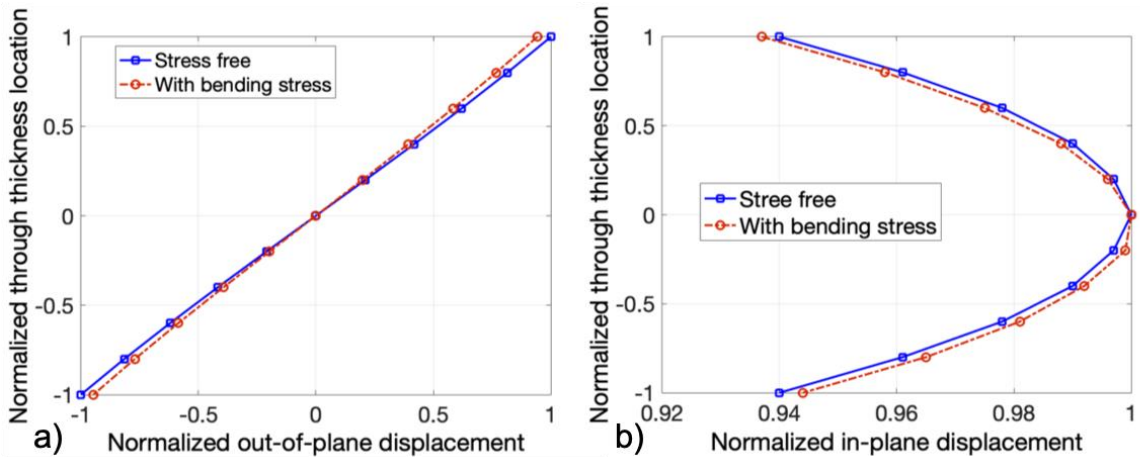

Figure 6-10: a): In-plane and b) out-of-plane displacement modeshape with and without applied bending stress

As shown in Figure 6-10, it can be seen that when the plate is at stress free condition, the in-plane displacement modeshape of the S_0 Lamb wave is symmetric about the mid-plane of the plate, while the out-of-plane mode shape is antisymmetric. As compared, when the plate is under the bending stress, both in-plane and out-of-plane displacement modeshapes are distorted.

6.5.2. Phase velocity change due to applied bending stress

In this section, the validated 3D FE model with material nonlinearity effect is used to simulate the acoustoelastic effect on Lamb wave propagation in plate under bending stress. The 3D FE model has same set-up (excitation frequency and location, boundary conditions, and FE mesh) as the one shown in Figure 6-2. Measurements are calculated for the nodal points at the top, mid-plane and bottom of the plate. A bending stress is applied along the surface highlighted in Figure 6-11, and the maximal magnitude of the stress is varied from 20MP to 80MPa.

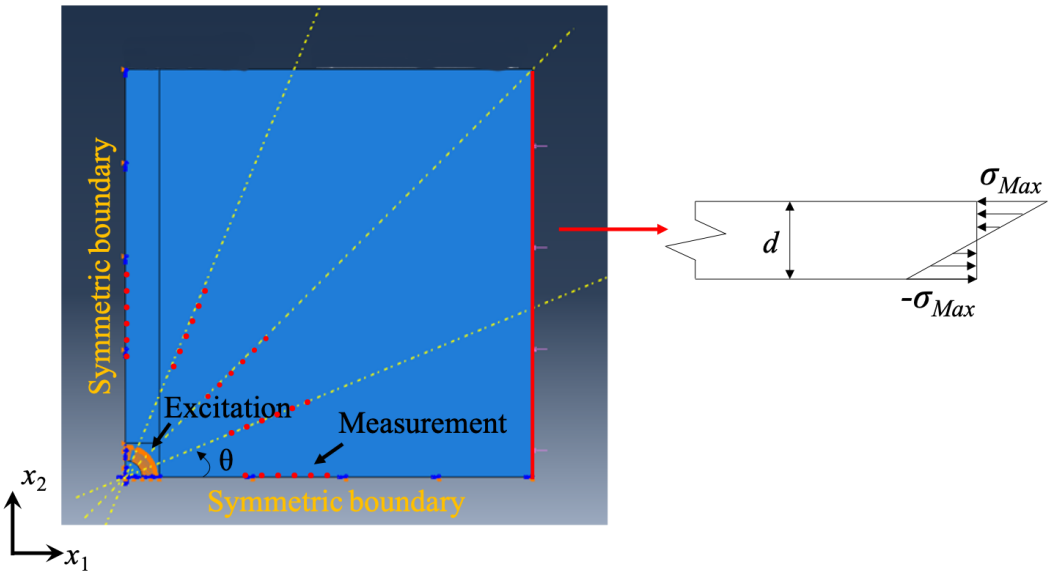

Figure 6-11: 3D FE model under bending stress

Results are shown in Figure 6-12. As shown in Figure 6-12a and b, the variation of phase velocity change against applied bending stress is linear in all propagation directions. Meanwhile, it should be noticed that, the phase velocity change obtained from the top and bottom of the plates in the same propagation direction under the same stress condition has very similar magnitudes but with opposite sign. In addition, as shown in Figure 6-12c, the phase velocity changes are about zero in all directions for all stress conditions. The results indicate that the phase velocity change is caused by the applied bending stresses. The region above and below the mid-plane of the plate are under tension and compression, respectively. As a result,

the phase velocity changes in Figures 6-12a and b have opposite trend. At the location of the mid-plane, the stress is zero so the value of the phase velocity change is almost zero despite increasing the applied bending stress.

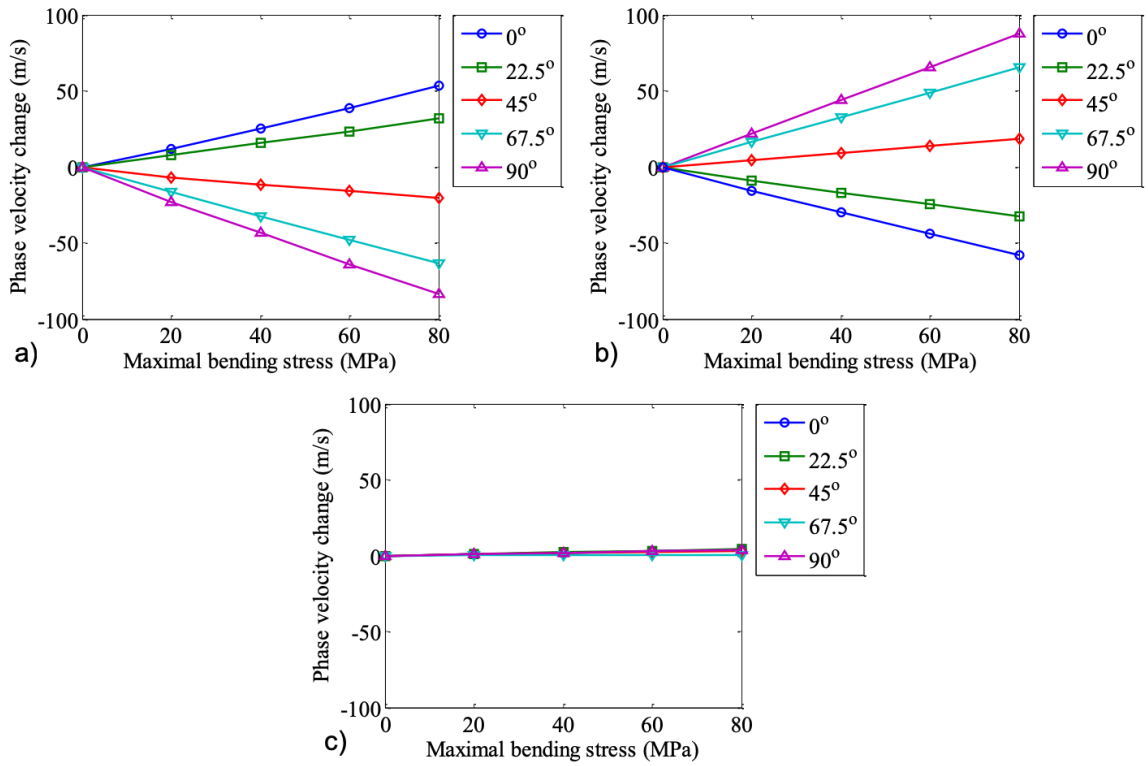

Figure 6-12: Phase velocity change with measurement calculated at the a) top, b) bottom, and c) mid-plane of the plate for different propagation directions and under different magnitudes of maximal bending stresses

6.6. Conclusions

The study provides a numerical analysis of the acoustoelastic effect of S_0 Lamb wave on a prestressed plate through the 3D FE model with nonlinear material model formulated based on Murnaghan's energy equation. A series of case studies have been conducted and the 3D FE calculated phase velocity changes have been compared with the analytical results. The 3D FE results show nearly perfect match with the analytical solutions with the consideration of different stress ratios, stress magnitudes and propagation angles. The results indicate that the 3D FE model with VUMAT subroutine, is able to simulate the acoustoelastic effect due to the nonlinear characteristics of a material under pre-stressed condition. The study has also investigated a more complicated stress situation, in which the bending stress has been

considered. The effects of the applied bending stress on the in-plane and out-of-plane displacement modeshapes have been studied. The analytically validated 3D FE model has been used to investigate the bending stress effect on the S_0 Lamb wave propagation in the plate.

The study has shown that the 3D FE model with nonlinear material model could be used to predict the acoustoelastic effect on the Lamb wave propagation in plate subjected to applied stress, including those complicated stress situations, where the analytically solution are not available. Meanwhile, the outcome of this study also provides physical insight into the acoustoelastic effect on the S_0 Lamb wave propagation. The findings contribute to the further developments of damage detection using Lamb waves.

Acknowledgement

This work was supported by the Australian Research Council (ARC) under Grant Numbers DP160102233. The support is greatly appreciated.

References

[1] Pan J, Zhang Z, Wu J, Ramakrishnan KR, Singh HK. 2019 *Compos. B: Eng.* **159** 437-446

[2] Zhou C, Zhang C, Su Z, Yue X, Xiang J, Li G. 2017 *Struct. Control Health Monit.* **24** e1966

[3] Zhang Z, Zhang C, Shankar K, Morozov EV, Singh HK, Ray T 2017 *Compos. Struct.* **176** 844-859.

[4] Zhang Z, Shankar K, Morozov EV, Tahtali M. 2016 *J. Vib. Control* **22** 496-512.

[5] Yu L, Leckey CAC, Tian Z. 2013 *Smart Mater. Struct.* **22** 065019.

[6] Dao PB, Staszewski WJ. 2014 *Mech. Syst. Signal. Process.* **49**(1-2) 285-301

[7] Soleimanpour R, Ng CT, Wang CH. 2017 *Struct. Health Monit.* **16**(4) 400-417

[8] Alguri KS, Melville J, Harley JB. 2018 *J. Acoust. Soc. Am.* **143**(6) 3807-3818

[9] Zak A, Radzienski M, Krawczuk M, Ostachowicz W. 2012 *Smart Mater. Struct.* **21** 035024

[10] Mitra M, Gopalakrishnan S. 2016 *Smart Mater. Struct.* **25** 053001

[11] Mohseni H, Ng CT. 2018 *Smart Mater. Struct.* **27** 105038

[12] Mohseni H, Ng CT, Lam HF. 2018 *Mech. Syst. Signal. Process.* https://doi.org/10.1016/j.ymssp.2018.08.027

[13] Liu Y, Lin S, Li Y, Li C, Liang Y. 2018 *Compos. B: Eng.* **158** 230-238

[14] Ng CT. 2015 *Int. J. Struct. Stab. Dyn.* **15**(8) 1540010.

[15] Panda RS, Rajagopal P, Balasubramaniam K. 2017 Struct. Health Monit. **16**(2) 142-152

[16] Memmolo V, Monaco E, Boffa ND, Maio L, Ricci F. 2018 *Compos. Struct.* **184** 568-580

[17] An YK, Sohn H. 2012 *Mech. Syst. Signal. Process.* **28** 50-62

[18] Yang Y, Ng CT, Kotousov A. 2019 *Int. J. Struct. Stab. Dyn.* **19**(1): 1940006

[19] He J, Yuan FG. 2016 *Struct. Health Monit.* **15**(1) 65-80

[20] He S, Ng CT. 2017 *Mech. Syst. Signal. Process.* **84** 324-345

[21] Hu N, Shimomukai T, Yan C, Fukunaga H. 2008 *Compos. Sci. and Tech.* **68**(6) 1548-1554.

[22] He S, Ng CT. A 2016 *Eng. Struct.* **127** 602-614

[23] Nasrollahi A, Deng W, Ma Z, Rizzo P. 2018 *Struct. Health Monit.* **17**(2) 395-409

[24] Aryan P, Kotousov A, Ng CT, Cazzolato BS. 2017 *Struct. Control Health Monit.* **24** e1894.

[25] Liu C, Dobson J, Cawley P. 2017 *Proc. R. Soc. A* **473** 2199

[26] Song Z, Qi X, Liu Z, Ma H. 2018 *NDT&E Int.* **93** 78-85

[27] Mohseni H, Ng CT. Rayleigh wave propagation and scattering characteristics at debondings in fibre-reforced polymer-retriofitted concrete strtuctures. Structural Health Monitoring, 2018, https://doi.org/10.1177/1475921718754371

[28] Rose JL. 2002 *J. Press. Vess. Tech.* **124**(3) 273-282

[29] Soleimanpour R, Ng CT. 2017 *Eng. Struct.* **131** 207-219

[30] Attarian VA, Cegla FB, Cawley P. 2014 *Struct. Health. Monit.* **13**(3) 265-280

[31] McKeon P, Yaacoubi S, Declercq NF, Ramadan S, Yaacoubi WK. 2014 *Ultrasonics* **54**(2) 592-603

[32] Aryan P, Kotousov A, Ng CT, Cazzolato B. 2017 *Struct. Control Health. Monit.* **24** e1894

[33] Sohn H. 2017 *Proc. R. Soc. A* **365**(1851) 539-560

[34] Lanza di Scalea F, Salamone S. 2008 *J. Acoust. Soc. Am.* **124**(161) 161-174

[35] Dao PB, Staszewski W. 2013 *Smart Mater. Struct.* **22**(9) 095002

[36] Aryan, P, Kotouso A, Ng CT, Wildy S. 2016 *Smart Mater. Struct.* **25** 035018

[37] Liu Y, Kim JY, Jacobs LJ, Qu J, Li Z. 2012 *J. Appl. Phy.* **111** 053511

[38] He S, Ng CT 2012 *Smart Mater. Struct.* **26** 085002

[39] Yang Y, Ng CT, Kotousov A, Sohn H, Lim HJ. 2018 *Mech. Syst. Signal. Process.* **99** 760-773

[40] Murnaghan FD. 1937 *Am. J. Math.* **59**(2) 235-260

[41] Hughes DS, Kelly JL. 1953 *Phy. Rev.* **92**(5) 1145

[42] Egle DM, Bray DE. 1976 *J. Acoust. Soc. Am.* **60**(3) 741-744

[43] Pau A, Lanza di Scalea F. 2015 *J. Acoust. Soc. Am.* **137**(3) 1529-1540

[44] Mohabuth M, Kotousov A, Ng CT. 2016 *Int. J. Nonlin. Mech.* **86** 104-111

[45] Gandhi N, Michaels JE, Lee SJ. 2012 *J. Acoust. Soc. Am.* **132**(3) 1284-1293

[46] Mohabuth M, Kotousov A, Ng CT, Rose LRF. 2018 *Smart Mater. Struct.* **27** 025003

[47] Packo P, Uhl T, Staszewski WJ, Leamy MJ. 2016 *J. Acoust. Soc. Am.* **140**(2) 1319-1331

[48] Asay JR, Guenther AH. 1967 *J. Appl. Phy.* **38** 4086-4088

[49] Yang Y, Ng CT, Kotousov A. 2018 *Smart Mater. Struct.* **27** 055013

Chapter 7. Simulation of acoustoelastic effect on second harmonic generation of Lamb wave in prestressed plate using three-dimensional finite element method

(Paper 6, Manucript)

Yi Yang[a], Ching-Tai Ng[a], Andrei Kotousov[b]

[a] School of Civil, Environmental and Mining Engineering, The University of Adelaide, Adelaide, SA 5005, Australia

[b] School of Mechanical Engineering, The University of Adelaide, Adelaide, SA 5005, Australia

Statement of Authorship

Title of Paper	Simulation of acoustoelastic effect on second harmonic generation of Lamb wave in prestressed plate using three-dimensional finite element method
Publication Status	☐ Published ☐ Accepted for Publication ☐ Submitted for Publication ☑ Unpublished and Unsubmitted w ork w ritten in manuscript style
Publication Details	Yang, Y., Ng, C., & Kotousov, A. (2019). Simulation of acoustoelastic effect on second harmonic generation of Lamb wave in prestressed plate using three-dimensional finite element method.

Principal Author

Name of Principal Author (Candidate)	Yi Yang
Contribution to the Paper	Undertook literature review, developed theoretical formulation of subroutine and code of subroutine, prepared manuscript
Overall percentage (%)	80%
Certification:	This paper reports on original research I conducted during the period of my Higher Degree by Research candidature and is not subject to any obligations or contractual agreements with a third party that would constrain its inclusion in this thesis. I am the primary author of this paper.
Signature	Date 11/01/2019

Co-Author Contributions

By signing the Statement of Authorship, each author certifies that:

i. the candidate's stated contribution to the publication is accurate (as detailed above);

ii. permission is granted for the candidate in include the publication in the thesis; and

iii. the sum of all co-author contributions is equal to 100% less the candidate's stated contribution.

Name of Co-Author	Ching-Tai Ng
Contribution to the Paper	Helped numerical model development, helped review manuscript and prepare for submission, and acted as corresponding author.
Signature	Date 11/1/2019

Name of Co-Author	Andrei Kotousov
Contribution to the Paper	Helped numerical model development and evaluate and edit the manuscript.
Signature	Date 4/1/2019

Please cut and paste additional co-author panels here as required.

ABSTRACT

This paper presents a three-dimensional (3D) finite element (FE) modelling of applied stresses effect on second harmonics generation of finite amplitude Lamb wave in an aluminium plate. In this study, the proposed 3D FE model incorporates stress constitutive equations formulated by Murgnahan's strain energy function to takes into account the acoustoelastic effect of higher harmonic generation of Lamb wave propagation in weakly nonlinear media. The stress constitutive equations formulated by Murgnahan's stain energy function are implemented in the 3D FE model using VUMAT in ABAQUS. The proposed 3D FE model is first validated by comparing with the simulation results with previous studies in the literature. The validated 3D FE model is then used to predict the variation of the relative second order nonlinear parameter (β'), at different wave propagation angles and distances under different scenarios of applied stresses. It is found that the proposed 3D FE model is able to provide a reliable simulation of the material nonlinearity of Lamb wave propagation in plate subjected to applied stress. The results show that the applied stresses can change the relative nonlinear parameter and the changes are different for different cases of applied stresses and wave propagation directions. A parametric study is also performed to investigate the effect of applied stresses on a plate with fatigue crack. The results show that the applied stresses can profoundly change the β' value due to contact nonlinearity.

KEYWORDS: Second harmonic, material nonlinearity, prestressed plate, finite element simulation, VUMAT, Abaqus, acoustoelastic effect

7.1. Introduction

The importance of Structural Health Monitoring (SHM) in engineering field is evidenced by different damage detection techniques developed in the last decade [1]-[3]. Non-destructive evaluation (NDE) using ultrasonic guided waves, such as Rayleigh wave [4][5] and Lamb wave [6] [7], has become a widely used technique to assess the safety condition of engineering structure. As compared with ultrasonic bulk wave, which provides point-by-point inspection, ultrasonic guided wave inspection technique is more efficient due to its ability to propagate long distances [8]-[10]. In the last two decades, different damage detection techniques using

conventional linear guided wave were developed [11]-[13]. However, conventional linear guided wave approach is limited to detect gross damages and their performance in damage detection is significantly affected by varying environmental conditions [14],[15], such as temperature changes and external loadings, while nonlinear guided wave is robust in detecting micro-structural defects.

7.1.1. Nonlinear guided wave

The nonlinear features of ultrasonic wave are revealed in frequency-domain of measured signals, e.g. higher harmonics [16][17] and sidebands [18][19] etc., which are different from the excitation frequency when the wave travels through structures with material nonlinearity. According to the review of Jhang [24], the nonlinearity can arise mainly from two aspects, material nonlinearity and contact nonlinearity due to contact-type damages. For higher harmonic generated due to contact nonlinearity, different types of guided wave were investigated, such as bulk wave [21], Rayleigh wave [4]-[5][22] and Lamb wave. Recently, the study of higher harmonic generation due to Lamb wave interaction with contact-type of damage has attracted significant attention. A number of studies focused on different types of damage, such as delamination [23]-[25], fatigue cracks [26]-[28], debonding [28][30], loosen bolt connections [29][32].

The studies of material nonlinearity using Lamb wave can be found in the literatures. The theoretical studies of material nonlinearity include research of Deng [16], Chillara and Lissenden [33], Wan *et al*. [34]. According to the studies of Pruell *et al*. [35] and Kim [36], material nonlinearity can be enhanced due to plastic deformation of a plate subjected to fatigue loading. The variation of the second order nonlinear parameter can be used to predict the fatigue life of the material. The study of Hong *et al*. [17] combined the intrinsic material nonlinearity and contact nonlinearity of a fatigue crack for damage detection.

In the literature, it has been demonstrated by studies concerning material nonlinearity that phase velocity matching and non-zero power flux are two necessary conditions to achieve a cumulative second order nonlinear parameter with increasing propagating distances. Most of the studies considered the cumulative second order nonlinearity due to the first order symmetric (S_1)-second order symmetric (S_2) mode pairs of Lamb wave propagation. However, high frequency Lamb wave includes multiple wave modes, which makes it difficult to distinguish the modes that satisfy phase matching and non-zero power flux conditions. Moreover, Lamb

waves are excited with finite frequency bandwidth and S_1 and S_2 Lamb wave are highly dispersive. Thus, there is only a fraction of the propagating waves strictly satisfy the velocity matching conditions.

Wan *et al*. [34] demonstrated that the velocity change of the fundamental symmetric (S_0) mode Lamb wave is very small in the low frequency region. It approximately satisfies the velocity matching condition and the cumulative material nonlinearity can also be observed within a certain propagation distance. The distance is closely related to the difference of phase velocity between the primary and second harmonic Lamb waves. The study also shows that the data processing becomes much easier when only one single Lamb wave mode exists, which can be achieved by using dual-PZT excitation in the low frequency region [38]. Different studies have also demonstrated the low frequency S_0 Lamb wave can be effectively used for detecting contact-type damage.

The previous studies using nonlinear Lamb wave showed that this feature is able to depict the weak nonlinearity on an intact plate and a plate with plasticity-driven nonlinearity under cyclic loading [35], and it can also be used to detect fatigue crack [39]. These findings demonstrated the potential of using nonlinear Lamb wave to develop a practical NDE technology to monitor the current conditions of a structure throughout the life cycle.

7.1.2. Acoustoelastic effect

Besides the change of structural discontinuity, the impact of stresses on the propagating wave on prestressed media, which is known as acoustoelastic effect, could also change the detected nonlinearity. Most studies on acoustoelastic effect on weakly nonlinear media using guided waves are based on the change of phase velocity of the propagating. Gandhi *et al*. [40] provided a comprehensive analysis of the acoustoelastic due to biaxial loading through analytical formulation and experimental measurement. However, their work only considered the first order in the infinitesimal strain tensor. In the more recent study by Mohabuth *et al*. [41], they developed the governing equation for the propagation of small amplitude waves in a pre-stressed plate using the theory of incremental deformations superimposed on large deformations. Their study was also extended to plates subjected biaxial stress condition. The dispersion of finite amplitude Lamb wave on nonlinear plates was studied with the consideration of up to fourth order elastic constants by Packo *et al*. [43]. The study of Pau and Lanza di Scalea [44] provided a theoretical insight of the stress effect on the second harmonics.

In the literature, there was very limited studies on the stress effect of the cumulative characteristic of second harmonic Lamb wave in isotropic material with weak nonlinearity. In this study, a three-dimensional (3D) FE model is proposed to gain fundamental understanding on stress variation effect of second harmonic Lamb wave against wave propagation distance. The proposed 3D FE model could be applied to study the second harmonic generation on damaged structures under prestress conditions. The 3D FE model would also show the potential of using second harmonic generation to estimate the stress magnitude in a prestressed material.

The paper is structured as follows. Section 2 describes the constitutive equations formulated by Murgnahan's strain energy function. Section 3 provides the details of implement the constitutive equations through VUMAT in ABAQUS. In Section 4, a 2D plane strain model used in the literature is modelled using the proposed FE model and the results are compared to verify the VUMAT in ABAQUS. Section 5 presents a study of the effect of different biaxial stress ratios, applied stress direction and magnitude on the higher harmonic generation. The study is extended to consider a prestressed plate with a fatigue crack. Finally, conclusions are drawn in Section 6.

7.2. Constitutive Equations

In this study, the definition of position for material particle in the reference and current configuration follows the definition of Mohabuth *et al*. [41][42], which are defined as $\boldsymbol{X}$ and $\boldsymbol{x}$, respectively. The deformation gradient **F** is defined as

$$\boldsymbol{F} = \frac{\partial \boldsymbol{x}}{\partial \boldsymbol{X}} \tag{1}$$

The Green-Lagrange strain tensor used in this study is given by:

$$\mathbf{E} = \frac{1}{2}(\mathbf{C} - \mathbf{I}) \tag{2}$$

where **I** is the identity tensor and **C** is the right Cauchy-Green deformation tensor, which is defined as:

$$\mathbf{C} = \mathbf{F}^{\mathrm{T}}\mathbf{F} = \mathbf{U}^{\mathbf{2}} \tag{3}$$

where **U** is the right stretch tensor.

The strain energy function according to Murnaghan [46] is written as:

$$\mathrm{W}(\mathbf{E}) = \frac{1}{2}(\lambda + 2\mu)i_1^2 - 2\mu i_2 + \frac{1}{3}(l + m)i_1^2 - 2mi_1 i_2 + ni_3 \tag{4}$$

where λ and μ are the lamé elastic constants; l, m and n are the third order elastic constants. $i_1 = \mathrm{tr}(\mathbf{E})$, $i_2 = \frac{1}{2}[i_1^2 - \mathrm{tr}(\mathbf{E})^2]$, $i_3 = \det(\mathbf{E})$, respectively. The partial derivatives of $\mathbf{W}$ with respect to $\mathbf{E}$ give the second Piola-Kirchhoff (PK2) stress

$$\mathbf{T} = \frac{\partial \mathrm{W}(\mathbf{E})}{\partial \mathbf{E}} \tag{5}$$

The relationship between Cauchy stress and PK2 stress is

$$\boldsymbol{\sigma} = \mathrm{J}^{-1}\mathbf{F}\mathbf{T}\mathbf{F}^{\mathrm{T}} = \mathrm{J}^{-1}\mathbf{F}\frac{\partial \mathrm{W}(\mathbf{E})}{\partial \mathbf{E}}\mathbf{F}^{\mathrm{T}} \tag{6}$$

where $\mathrm{J} = \det(\mathbf{F})$.

7.3. VUMAT Implementation

In ABAQUS/Explicit, VUMAT can be used to define the mechanical constitutive behaviour of the nonlinear material property formulated in Section 2. In ABAQUS, the stress in VUMAT of ABAQUS/Explicit is the Cauchy stress tensor in Green-Naghdi basis and is given by

$$\hat{\boldsymbol{\sigma}} = \mathbf{R}^{\mathrm{T}}\boldsymbol{\sigma}\mathbf{R} \tag{7}$$

where $\mathbf{R}$ is rotation tensor, and $\mathbf{R}$ is a proper orthogonal tensor, i.e., $\mathbf{R}^{-1} = \mathbf{R}^{\mathrm{T}}$. The relationship between $\mathbf{F}$, $\mathbf{U}$ and $\mathbf{R}$ is given by

$$\mathbf{F} = \mathbf{R}\mathbf{U} \tag{8}$$

Using Equations (6) and (8), Equation (7) can be translated to

$$\hat{\boldsymbol{\sigma}} = \mathrm{J}^{-1}\mathbf{R}^{\mathrm{T}}\mathbf{F}\mathbf{T}\mathbf{F}^{\mathrm{T}}\mathbf{R} = \mathrm{J}^{-1}\mathbf{R}^{\mathrm{T}}\mathbf{R}\mathbf{U}\mathbf{T}\mathbf{U}^{\mathrm{T}}\mathbf{R}^{\mathrm{T}}\mathbf{R} = \mathrm{J}^{-1}\mathbf{U}\frac{\partial \mathrm{W}(\mathbf{E})}{\partial \mathbf{E}}\mathbf{U}^{\mathrm{T}} \tag{9}$$

Equation (9) provides the stress constitutive equation that is used in the VUMAT subroutine. The stress in VUMAT must be updated with the equation at the end $(t + \Delta t)$ of an integration step and stored in stressNew(i), based on the values of $\mathbf{F}$ and $\mathbf{U}$ given in the subroutine at the end of previous step (t).

7.4. Numerical Validation

This section presents a validation of the VUMAT subroutine developed based on the stress constitutive equations described in Section 2. The second harmonic generation calculated by the FE model with the developed VUMAT subroutine is first validated by comparing the results presented by Wan *et al*. [34]. A similar two-dimensional (2D) plane strain model is created in ABAQUS/Explicit and constitutive equations are simplified to 2D condition and implemented in the VUMAT of ABAQUS. Figure 7-1 shows the schematic diagram of the FE model, which is 2mm thick and 1000mm long aluminium plate. The Lamb wave signal is excited at the left end of the plate and the excitation signal is a sinusoidal tone burst pulse modulated by a Hanning window. The excitation signal is applied through the displacement at the nodal points. A fixed boundary condition is assigned to the right end of the plate. Both 6061-T6 and 7075-T651 aluminium plates are considered in the study and the material properties are shown in Table 7-1.

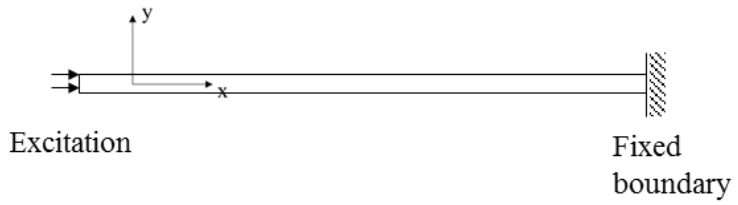

Figure 7-1: Schematic diagram of 2D FE plate model in ABAQUS

Table 7-1. Material properties of 6061-T6 and 7075-T651

Material	ρ (kg/m^3)	λ (GPa)	μ (GPa)	l (GPa)	m (GPa)	n (GPa)
6061-T6	2704	50.3	25.9	-281.5	-339	-416
7075-T651	2810	52.3	26.9	-252.2	-325	-351.2

In this study, the element size is controlled to ensure there are at least 20 elements exist per wavelength so that it can ensure the accuracy of the simulations. There are 8 elements in the thickness direction. Since the second harmonic generation is of interest, the element size is chosen based on the wavelength of the second harmonic Lamb wave. The element is a 4-node bilinear plane strain quadrilateral with reduced integration (CPE4R).

7.4.1. Second harmonic amplitude variation against propagation distance

In the first set of validation study, the maximum cumulative propagation distance (MCPD) within which the displacement amplitude of second harmonic increases with the propagation distance [34] is investigated. The excitation signals of 300kHz and 400kHz fundamental symmetric mode (S_0) Lamb wave are used separately. The number of cycles of the wave signal is 18 and the excitation magnitude of the displacement is 5μm. The time dependant strain component in *x* direction is obtained and transformed to frequency-domain by Fast Fourier Transform (FFT). For the 300 kHz excitation, measurements are taken at every 50mm and for 400 kHz excitation the measurements are taken at every 12.5mm. Figure 7-2 shows the excited signal calculated at 200mm away from the excitation location in time- and frequency-domain and the excitation frequency is 300kHz.

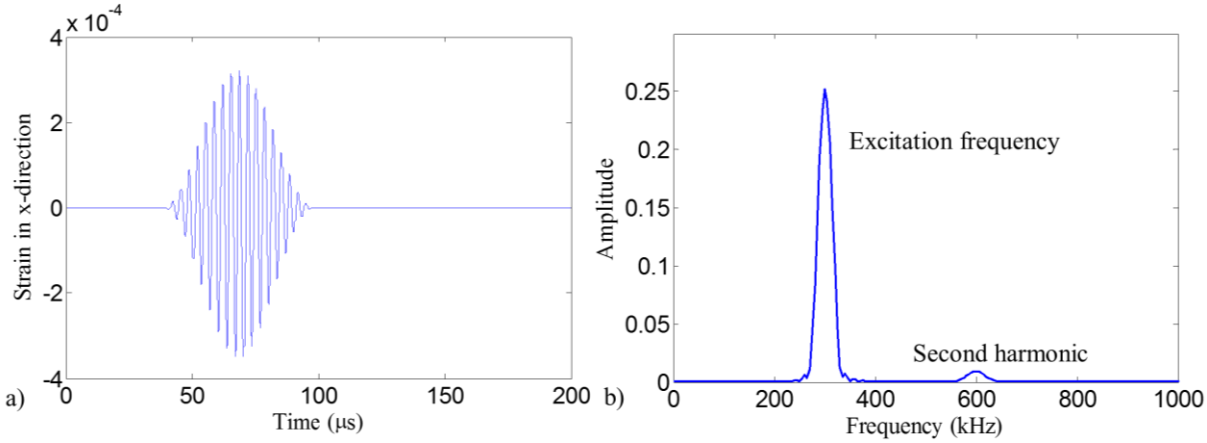

Figure 7-2: a) Time-domain and b) frequency spectrum of strain in x direction calculated at 200mm from the excitation location with 300kHz excitation signal

The amplitude of the second harmonic for the two different excitation frequencies is obtained and plotted as shown in Figure 7-3. It can bee see that the MCPD for 300kHz and 400kHz cases are 200mm and 62.5mm respectively. As compared to the corresponding theoretical value of 220.02mm and 69.51mm, which are consistent with the results presented in [34]. This indicates the proposed FE model provide correct prediction.

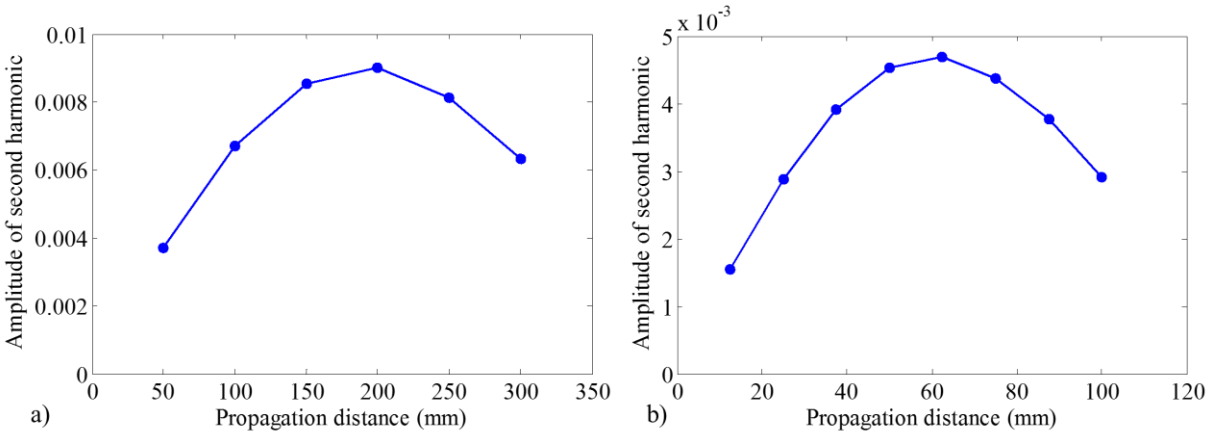

Figure 7-3: Second harmonic amplitude against propagation distance for excitation frequency is a) 300 kHz and b)400 kHz

7.4.2. Second order nonlinear parameter ratio between different materials

The second validation study is carried out through obtaining the slope ratio of the linearly cumulative second order nonlinearity with propagation distances when different materials are used. The excitation frequency is chosen as 100 kHz, as the second harmonic amplitude keeps increasing until the propagation distance reaches 7764.72mm [34]. The number of cycles of the excitation signal remains to be 18. The S_0 Lamb wave is excited on both 6061-T6 and 7075-T651 aluminium plates.

In this study, the relative nonlinear parameter β' is defined as:

$$\beta' = \frac{A_2}{A_1^2} \tag{10}$$

where A_1 and A_2 are the amplitude at the excitation frequency and the second harmonic respectively in frequency-domain. The calculated relative nonlinear parameters (β') for the two plates with different material properties at different propagation distances are shown in Figure 7-4. As shown in Table 7-1, the nonlinear parameters, *l*, *m* and *n*, of 6061-T6 are larger than those of 7075-T651. The larger nonlinear parameters introduce larger values of relative nonlinear parameter and a higher rate of increasing amplitude with propagation distance. The slope of for the curve of 6061-T6 is about 0.00228 (mm^{-1}), while for the curve of 7075-T651 the slope is about 0.00205 (mm^{-1}). As a result, the ratio between the two slopes is around 1.11, compared to the actual value of 1.12 [34]. Based on the two sets of validations, the FE model with VUMAT subroutine coded with the stress constitutive equation obtained from

Murnaghan's strain energy function is able to provide a reliable prediction of the material nonlinearity.

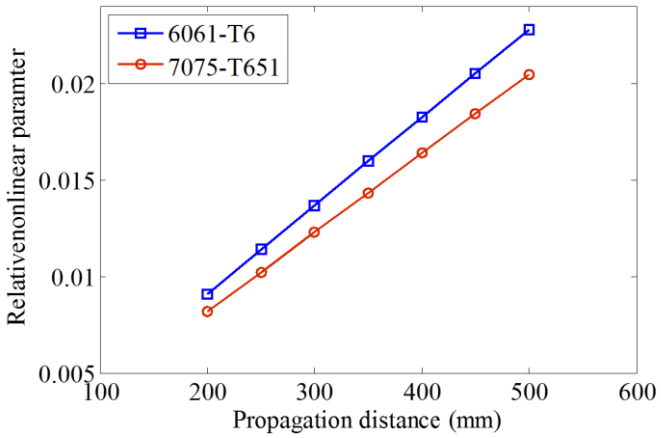

Figure 7-4: Relative nonlinear parameter with propagation distance

7.5. Three-dimensional finite element model of prestressed plate

The 3D FE model used in this study is a 500mm×500mm plate with 2mm thickness. By taking advantage of symmetric nature of the plate, only 1/4 of the actual in-plane dimension of the plate is modelled with the use of symmetric boundaries as shown in Figure 7-5. The material of the plate is 6061-T6 aluminium. The S_0 Lamb wave is excited at the corner of the model by applying 5μm displacement to the nodal points at the circumference of the 1/4 of a circle with a 10mm diameter. The excitation frequency of the Lamb wave is 200kHz and the number of cycles is 8. According to the requirement for the maximum size of the element as discussed in Section 4, the in-plane element size for the 3D mode is 0.4mm and there are 8 elements in the thickness direction, which results in an aspect ratio of 1.6. The elements are 8-noded linear brick with reduced integration (C3D8R).

Stresses are applied at both free boundaries as σ1 and σ2, with $\sigma 2 = \lambda \sigma 1$. The stresses are applied by adding a quasi-static loading with a duration of 0.004sec. After the plate is stressed, Lamb wave is excited, and the propagating wave is measured in five different directions (θ) as illustrated in Figure 7-5. Similar with the second set of the validation study in Section 4.2, the relative nonlinear parameter is obtained and compared for the 3D FE model under different

loading scenarios. In this study, positive stress value means that the stress is applied as tension while negative value means the stress is applied as compression.

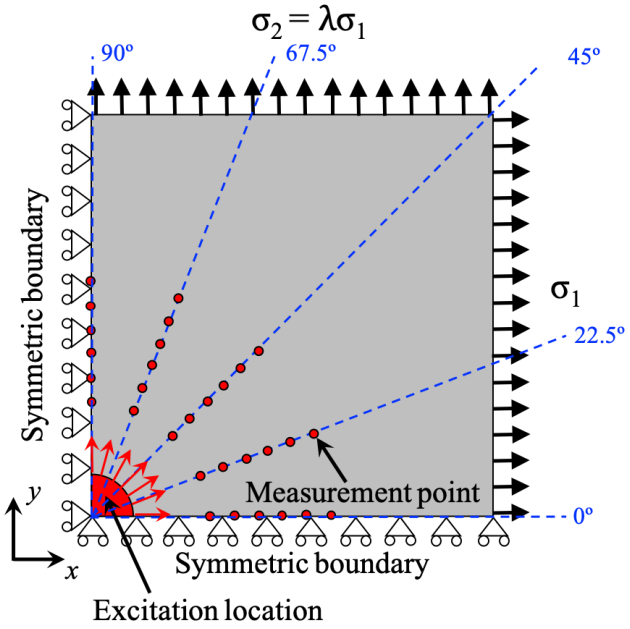

Figure 7-5: Schematic diagram of the 3D FE model in ABAQUS

The out-of-plane strain component in time-domain without considering the boundary reflection is obtained and transformed to frequency-domain by FFT, from which the relative nonlinear parameter is calculated using Equation (10). Figure 7-6 shows the variation of the relative nonlinear parameter β' with the propagation distance increased from 30mm to 105mm away from the excitation location. For different loading ratios at different propagation directions, the value of β' increases linearly with increasing propagation distance. For the stress-free case and the loading case when λ = 1, the slopes (k) of the increasing β' are the same in all propagation directions. In contrast, when λ = -1 or 0, the k value obtained at different propagation directions differs to each other, and the difference of k value is larger when λ = -1 than that when λ = 0. For larger stress magnitude, the increasing slope of the relative nonlinear parameter is larger as shown in Figure 7-7.

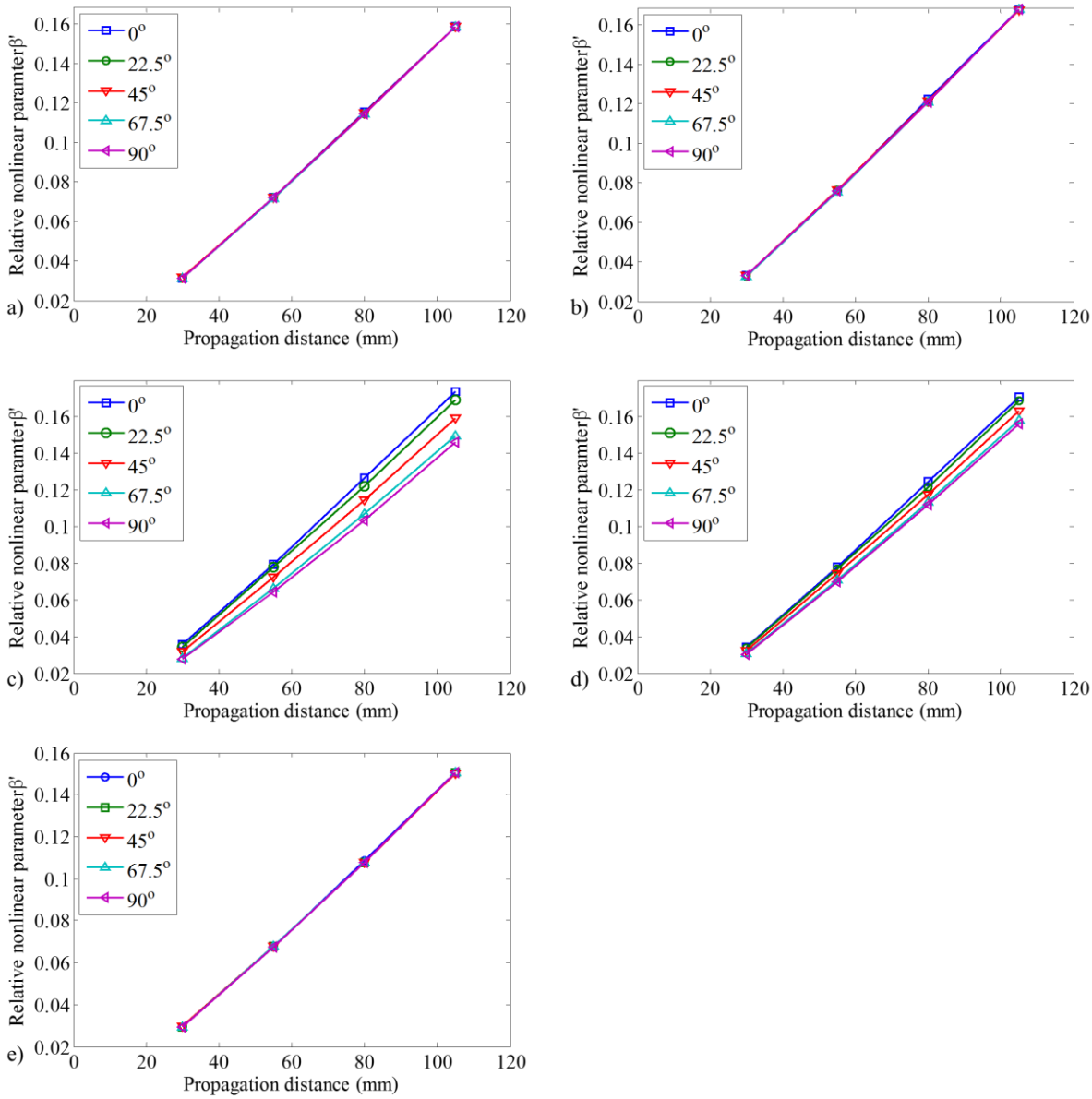

Figure 7-6: Relative nonlinear parameter for cases with a) stress free; b) σ1 = 100MPa, λ = 1; c) σ1 = 100MPa, λ = -1; d) σ1 = 100MPa, λ = 0; and e) σ1 = -100MPa, λ = 1 condition

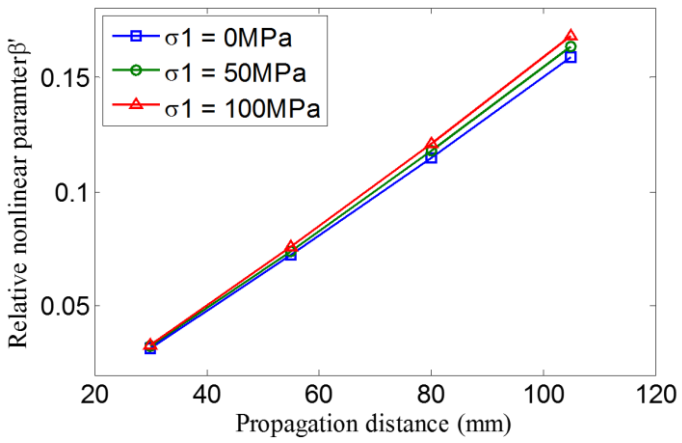

Figure 7-7: Relative nonlinear parameter of different stress magnitudes with propagation distance in the 45^o propagation direction and $\lambda = 1$.

To compare the results of different cases, a normalised slope *k'* is defined by

$$k'(\lambda, \sigma 1) = \frac{k(\lambda,\sigma_1)}{k_{stress\ free}} \tag{11}$$

where $k_{stress\ free}$ is the slope for stress free case and $k(\lambda, \sigma_1)$ is the slope for the plate subjected to stresses with different λ and σ_1 conditions. The results are obtained and demonstrated in Figure 7-8. It is found that when $\theta \approx 22.5^o$, the normalised slope is the same when the magnitude of $\sigma 1$ is the same despite the differences in λ. For the asymmetric loading, i.e., $\lambda = 1$ or 0, the slope of the increment of β' decreases when the propagation angle varies from 0^o to 90^o. Interestingly, it is observed that the average value of the normalised slope for (λ, $\sigma 1$) = (-1, 100MPa) and (λ, $\sigma 1$) = (1, 50MPa) is the same with *k'* for (λ, $\sigma 1$) = (1, 0) and (λ, $\sigma 1$) = (0, 50MPa), respectively. It is noticeable for the two antisymmetric pairs, the stress summation, $\sigma 1 + \sigma 2$, is the same for each pair.

For the biaxial compression case (λ, $\sigma 1$) = (1, -100MPa), the values of *k'* at different propagation directions are the same and are smaller than that of the stress-free condition. In contrast for the two biaxial tension cases, the values are larger than stress free condition, and the difference in *k'* value between stress-free and (λ, $\sigma 1$) = (1, 100MPa) cases is twice as large as the difference between stress-free and (λ, $\sigma 1$) = (1, 50MPa) cases. Moreover, the results show that the variation of *k'* is parallel for (λ, $\sigma 1$) = (0, 100MPa) and (λ, $\sigma 1$) = (0, -100MPa), which have the same stress magnitude though one is in uniaxial tension while the other is in uniaxial compression. The pattern of the relative slope variation indicates that it is possible to estimate the stress ratios and directions on a prestressed plate. However, the slope increases for increased stress is not very distinctive. Considering the measurement errors in experimental tests, it is a challenging task to give reliable estimation of stress magnitude based on the slope of the increment of experimentally measured relative nonlinear parameter.

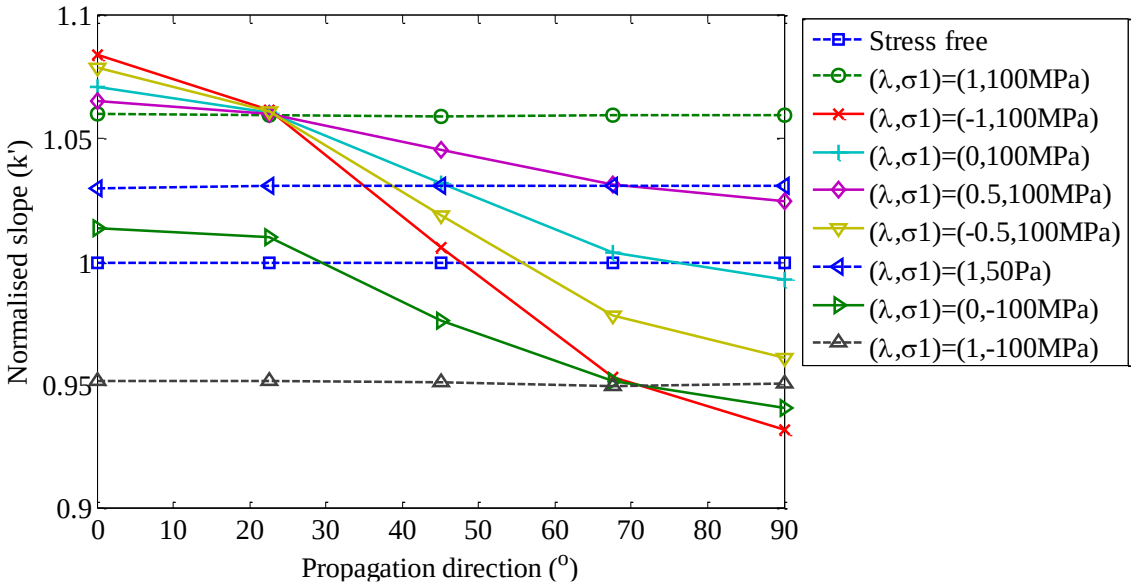

Figure 7-8: Normalised slope of the increasing relative nonlinear parameter with propagation distance for different loading scenarios.

On the other hand, the change of nonlinear parameter under applied stress exerts uncertainty in fatigue damage detection. It was revealed in the study of Pruel *et al*. [35], the maximal increase of normalised nonlinear parameter throughout the fatigue life of the aluminium plate is roughly more than 10%. Referring to Figure 8, the maximal variation of the nonlinear parameter is roughly ±8%, which occurs in the stress case of (λ, σ1) = (1, -100MPa) at 0° and 90° propagation direction. As a result, a benchmark test would be necessary for monitoring fatigue damage on prestressed structural components.

7.6. Detecting fatigue crack on a prestressed plate

As demonstrated in Section 5, the second harmonic could be affected by applied stress on structures. The tensile stress could open an initially closed fatigue crack and change the contact behaviour of the crack surface, as a consequence, the second harmonic generation due to contact nonlinearity could be altered and this adds difficulty in detecting the fatigue crack in the structures. In this section, the same 3D FE model used in Section 5 is employed and a fatigue crack (Figure 7-9) is also created on this 3D FE model. The second harmonic generation under biaxial tension, i.e., (λ, σ1) = (1, 100MPa), is investigated in this section.

A 4 mm long fatigue crack located around 30mm away from the excitation is modelled using seam in ABAQUS and interaction effect between two crack surfaces is modelled by frictional

tangential contact and 'Hard' normal contact, which prevents mutual penetration of these crack surfaces [46]. The measurements are taken at the same locations and wave propagation directions as those used in Section 5. Three 3D FE models are considered, an intact plate, a plate with the fatigue crack without any applied stress, and a plate with the fatigue crack under biaxial tension. The results are compared and shown in Figure 7-10.

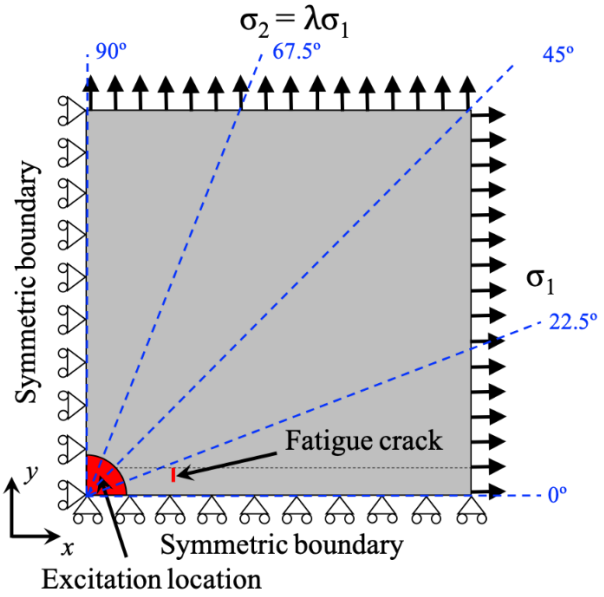

Figure 7-9: Schematic diagram of the 3D FE model with the fatigue crack

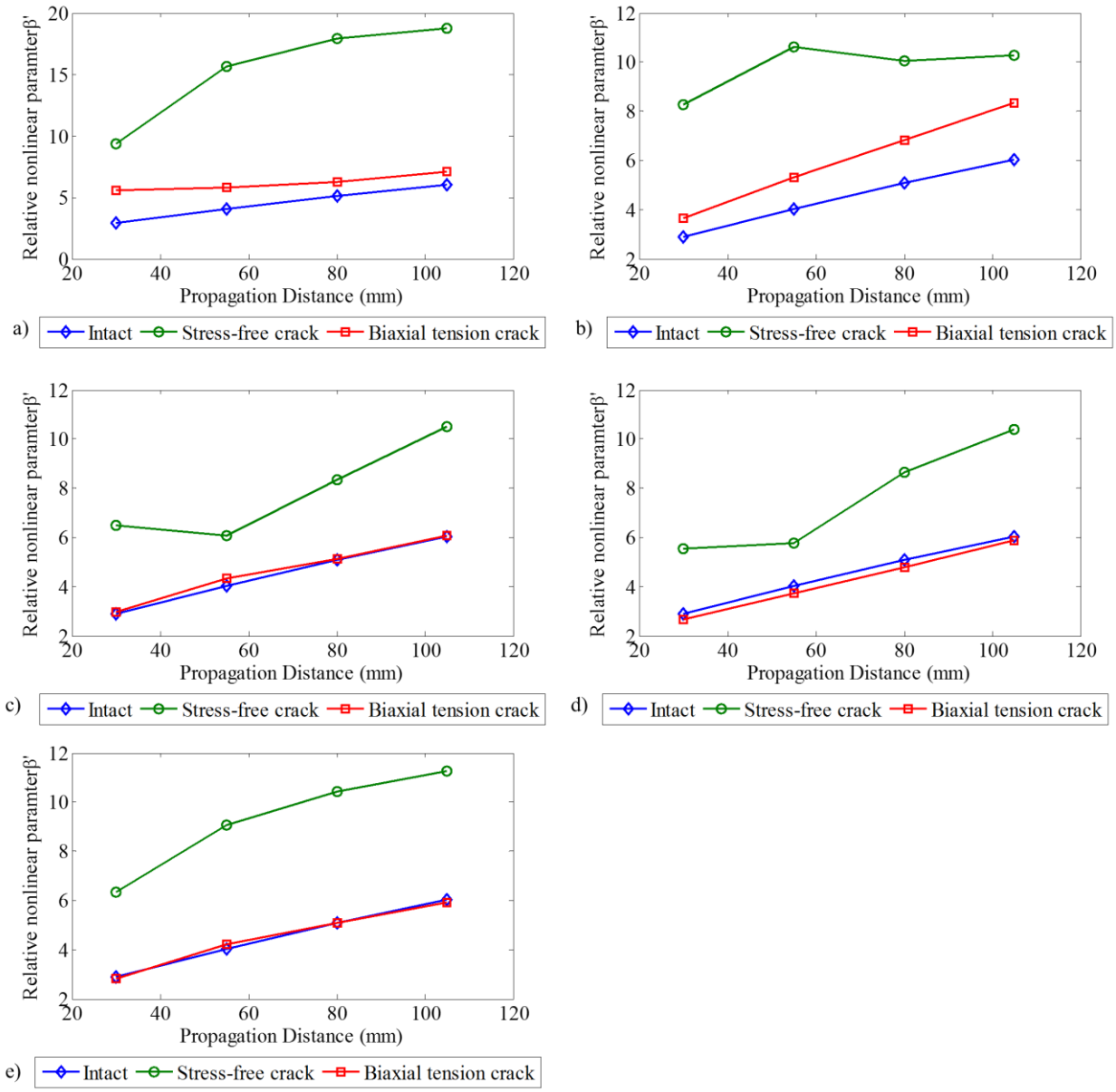

Figure 7-10: Relative nonlinear parameter obtained from the intact plate, unstressed, and stressed plate with the fatigue crack in a) 0°, b) 22.5°, c) 45°, d) 67.5° and e) 90° propagation directions

The results in Figure 10 show that when the fatigue crack is modelled without applying any stresses, the relative nonlinear parameter is obviously higher than that from the intact plate. It indicates that the effect of the contact nonlinearity at the fatigue crack is more dominant in second harmonic generation than the intrinsic material nonlinearity. However, when the biaxial tension is applied, the β' drops to about the same level of that from the intact plate, except for the cases of 0° and 22.5° propagation directions, at which the fatigue crack is close to the measurement points. The phenomenon can be due to the fact that the fatigue crack is opened

by the tensile stress, which dramatically reduces the contact area between the crack surfaces, and thus, it reduces the second harmonic generation due to the contact nonlinearity. This parametric study demonstrates that the second harmonic generation due to the fatigue crack can be overlooked if the plate is under tension and the fatigue crack is opened by tensile stress. However, it should be noted that the 3D FE model does not consider the plastic deformation around the fatigue crack, which will also generate extra second harmonics [35]. Further study can be conducted to confirm the reliability of second harmonic generation technique in detecting fatigue damage on a prestressed plate with the consideration of the plastic deformation effect.

7.7. Conclusions

The study has presented the 3D FE simulation of the stress effect on higher harmonic generation due to material nonlinearity. The second order material nonlinearity has been modelled by VUMAT in ABAQUS using stress constitutive equations formulated by Murnaghan's strain energy function. The nonlinear material model has been first validated using the 2D plate by comparing the results with results in the existing study. There is good agreement between the simulation results calculated by the proposed nonlinear material model and the results in the existing study.

The 3D FE model of the prestressed plate has been modelled and investigation has been carried out on the variation of the relative nonlinear parameter for different stress magnitudes, biaxial stress ratios, propagation distances and propagation directions. It has been found that based on the variation features of relative nonlinear parameter, it is possible to estimate the biaxial stress ratios and stress directions, despite the difficulty in achieving the accurate stress magnitude measurement of the relative nonlinear parameter variation with propagation distance. The results have also illustrated that the applied stress changes the value of β' and the change increases with propagation distance. Finally, the proposed 3D FE model has been used to study the stress effect on both material nonlinearity and damage detection of the plate with the fatigue crack. The results have shown that the second harmonic generation due to the contact nonlinearity can be overlooked if the plate is under tension and the fatigue crack is opened by the tensile stress.

Acknowledgement

This work was supported by the Australian Research Council (ARC) under Grant Numbers DP160102233. The support is greatly appreciated.

References

[1] Pan J, Zhang Z, Wu J, Ramakrishnan KR, Singh HK. A2019 *Compos. B: Eng.* **159** 437-446

[2] Zhang Z, Zhang C, Shankar K, Morozov EV, Singh HK, Ray T. 2017 *Compos. Struct.* **176** 844-859.

[3] Zhang Z, Shankar K, Morozov EV, Tahtali M. 2016 *J. Vib. Control* **22** 496-512

[4] Ng CT, Mohseni H, Lam HF. 2018 *Mech. Syst. Signal. Process.* https://doi.org/10.1016/j.ymssp.2018.08.027

[5] Mohseni H, Ng CT. 2018 *Smart Mater. Struct.* **27** 105038

[6] Hu N, Shimomukai T, Yan C, Fukunage H. 2008 *Compos. Sci. and Tech.* **68**(6) 1548-1554.

[7] Ng CT. 2015 *Int. J. Struct. Stab. Dyn.* **15**(8) 1540010

[8] Rose LR. 2002 *J. Press. Vess. Tech.* **124**(3) 273-282

[9] He S, Ng CT. 2016 *Eng. Struct.* **127** 602-614

[10] Ray P, Srinivasan B, Balasubramaniam K, Rajagopal P. 2018 *Ultrasoncs* **90** 120-124

[11] Aryan P, Kotousov A, Ng CT, Cazzolato B. 2017 *Struct. Control Health. Monit.* **24** e1894

[12] Zhou C, Zhang C, Su Z, Yue X, Xiang J, Li G. 2017 *Struct. Control Health Monit.* **24** e1966

[13] He S, Ng CT. 2017 *Mech. Syst. Signal. Process.* **84** 324-345

[14] Marzani A, Salamone S. 2012 *Mech. Syst. Signal. Process.* **30** 204-217

[15] Aryan P, Kotousov A, Ng CT, Wildy S. 2016 *Smart Mater. Struct.* **25** 035018

[16] Deng M. 1999 *J. Appl. Phy.* **85**(6) 3051-3058

[17] Soleimanpour R, Ng CT. 2017 *Eng. Struct.* **131** 207-219

[18] Klepka A, Staszewski WJ, Maio DD, Scarpa F. 2013 *Smart Mater. Struct.* **22** 084011

[19] Liu P, Sohn H. 2017 *NDT&E Int.* **91** 120-128

[20] Jhang KY. 2009 *Inter. J. Precision Eng. Manu.* **10** 123-135.

[21] Biwa S, Hiraiwa S, Matsumoto E. 2006 *Ultrasonics* **44** e1319-e1322.

[22] Yuan M, Zhang J, Song SJ, Kim HJ. 2015 *Wave Motion* **57** 143-153

[23] Yelve NP, Mitra M, Mujumdar PM. 2017 *Compos Struct* **159**(1) 257-266

[24] Soleimanpour R, Ng CT, Wang CH. 2017 *Struct. Health Monit.* **16**(4) 400-417

[25] Liu X, Bo L, Yang K, Liu Y, Zhao Y, Zhang J, Hu N, Deng M. 2018 *Mech. Syst. Signal. Process.* **109** 58-73

[26] Yang Y, Ng CT, Kotousov A, Sohn H, Lim HJ. 2018 *Mech. Syst. Signal. Process.* **99** 760-773

[27] Shen Y, Wang J, Xu W. 2018 *Smart Mater. Struct.* **27** 105044

[28] Yang Y, Ng CT, Kotousov A. 2018 *Smart Mater. Struct.* **27** 055013

[29] Scarselli G, Ciampa F, Ginzburg D, Meo M. 2015. *SPIE Proc.* **9437** 943706

[30] Mandal DD, Banerjee S 2019 *Mech. Syst. Signal. Process.* **117** 33-51

[31] Amerini F, Meo M. 2011 *Struct. Health Monit* **10** 659-672

[32] Yang Y, Ng CT, Kotousov A. 2018 *Struct. Health Monit* https://doi.org/10.1177/1475921718814399

[33] Chillara VC, Lissenden CJ. 2016 *Optical Eng.* **55** 011002.

[34] Wan X, Tse PW, Xu GH, Tao TF, Zhang Q. 2016 *Smart Mater. Struct.* **25** 045023

[35] Pruell C, Kim JY, Qu J, Jacobs LJ. 2009 *NDT&E Int.* **42** 199-203

[36] Kim JY, Jacobs LJ, Qu J. 2006 *J. Acoust. Soc. Am.* **120**(3) 1266-1273

[37] Hong M, Su Z, Wang Q, Cheng L, Qing X. 2014 *Ultrasonics* **54** 770-778

[38] Sohn H. 2011 *KSCE J. Civil Eng* 2011, **15** 1395-1404

[39] He S, Ng CT. 2017 *Smart Mater. Struct.* **26** 085002

[40] Gandhi N, Michaels JE, Lee SJ. 2012 *J. Acoust. Soc. Am.* **132**(3) 1284-1293

[41] Mohabuth M, Kotousov A, Ng CT. 2016 *Int. J. Nonlin. Mech.* **86** 104-111

[42] Mohabuth M, Kotousov A, Ng CT, Rose LRF. 2018 *Smart Mater. Struct.* **27** 025003

[43] Packo P, Uhl T, Staszewski WJ, Leamy MJ. 2016 *J. Acoust. Soc. Am.* **140**(2) 1319-1331

[44] Pau A, Lanza di Scalea F. 2015 *J. Acoust. Soc. Am.* **137**(3) 1529-1540

[45] Murnaghan FD. 1937 *Am. J. Math.* **59**(2) 235-260

[46] Yang Y, Ng CT, Kotousov A. 2019 *Int. J. Struct. Stab. Dyn.* **19**(1): 1940006

Chapter 8. Conclusions

8.1. Summaries and Significances

This PhD study has investigated the nonlinear phenomena associated with low-frequency GWs and presence of damage, specifically focusing on the SHG. The methodology is based on experimental guided wave techniques, 3D implicit FE method and a theoretical analysis. As one outcome of this thesis, it has found that the 3D FE simulations can be implemented to study various nonlinear features of GW interactions with defects, and thus, these simulations can provide a cost-effective alternative to experimental studies. As mentioned before, this thesis represents a compendium of published and submitted research articles in leading journals in the research area.

In the first two papers (Chapters 2 and 3), the focus is on the investigation of the nonlinear phenomena associated with the presence of fatigue cracks. It is firstly found that the S_0 mode GW, which is dominated by the in-plane displacements, is more sensitive to the fatigue cracks than A_0 mode of GW. Then, the GW set-up parameters, such as incident wave angle, sensor locations respect to the crack, and external loads on the material that would affect second harmonic generation of GW are investigated. It is also validated that the FE model of fatigue crack is able to predict the SHG behaviour. The first two studies (Chapters 2 and 3) provided important physical insights into SHG and can be used in design of a practical damage detection system based on the nonlinear GW.

The literature on detecting loosen bolt using GW is very limited, especially on using the nonlinear GWs. A feasibility study of using SHG for detecting the loosening in bolted joints is a research topic of the third paper (Chapter 4). This study showed that for a loosen bolt, the A_0 mode of GWs is more sensitive than S_0 mode. Although it is shown that the variation of second harmonic amplitude due to the different tightening torque can provide the information about the integrity of the bolted joint, the reliability of the method remains limited for potential practical application as the fluctuation of the results are relatively large.

It is concluded from the research outcomes of the previous studies (Chapters 2 – 4) that different GW modes are sensitive to defects with different contact behaviours. Based on this observation, a 3D FE model aluminium plate repaired with a composite patch weakened by a fatigue crack and delamination is developed. The results show that it is possible, by using different GW modes to detect different types of defects i.e. fatigue cracks and delaminations.

Besides the contact nonlinearity, material nonlinearity also contributes significantly to the generated second harmonic of GW. In the fifth paper (Chapter 6), a VUMAT subroutine is developed based on the Murnaghan's strain energy function to evaluate the effect of the material nonlinearity on the generation of the second harmonic. The FE model with nonlinear material subroutine is validated by comparing with theoretical solutions of the phase velocity change due to stresses and the second order nonlinear parameter variation with the wave propagation distance. The results from the FE model give a very good agreement with the theoretical solutions. The previous studies on acoustoelastic effects of GW were all based on theoretical and experimental approaches. However, compared with the theoretical analyses and experimental tests, the FE-based approach provides a more convenient, flexible, comprehensive and cheaper way to study the acoustoelastic effects in a prestressed waveguides and structures. Meanwhile, this approach also provides an opportunity for a more general material definition in studying the nonlinear GW phenomena and features associated with defects and damage.

Based on the verified material nonlinearity model (subroutine) in Chapter 6, a comprehensive 3D FE model is developed in the sixth paper (Chapter 7) to combine the effects of material nonlinearity, contact nonlinearity and stress applied on second harmonic generation. The reliability of the model with subroutine in SHG of material nonlinearity is firstly validated by comparing with the theoretical results from a previous research. In the first parametric study with the nonlinear material model, the variation of SHG due to applied stresses, propagation directions and distances is investigated. According to the results, it shows that the SHG due to acousto-elastic effects can be used to predict the amplitude and stress ratio of the applied bi-axial stress on the plate. At the same time, the results also indicate that with the increasing propagation distance of waves and amplitude of stresses applied, SHG due to material nonlinearity under loading is comparable to that generated by fatigue damage. Thus, it is important to consider the acousto-elastic effect when developing a practical fatigue damage detection system. In the second parametric study, the model is used to study the effects of applied stress on both material nonlinearity and contact nonlinearity of a plate with a fatigue crack. The results have shown that the second harmonic generation due to the contact nonlinearity can be overlooked if the plate is under tension and the fatigue crack is opened by the tensile stress.

8.2. Recommendation for future researches

In the case of fatigue cracks and bolt loosening, future research can be carried out on the development of in-situ damage detection systems. Some of the problems still remain to be solved. Firstly, all the previous studies on the fatigue crack used only one specimen to reveal some important characteristics of SHG. However, as the SHG depends on the interaction of crack interfaces, and the crack profile, i.e., crack opening and shapes, can be quite different on each specimen, it is worth to investigate the effects due to the difference in the crack profiles in the same material and with the same lengths of the cracks. This could improve the reliability and repeatability of the experimental results. Meanwhile for bolt joints, it would also be of interest to look into the feasibility of using the method to detect bolt loosening in a group of bolts and find out which specific bolted connections are defective. As for the composite patch, new experimental tests can be carried out to confirm the findings from the FE simulations presented in this thesis.

In addition, with the developed nonlinear material subroutine, the study could be extended to different types of structures, such as pipes, for which the analytical solutions for the nonlinear GW are unknown and very difficult (or impossible) to derive. As GWs in a pipe wall is much more dispersive than in a plate, the experimental measurements can also be very challenging without some fundamental understandings of the nonlinear GW features for the pipe geometries. Studies relating to fatigue crack or plastic deformation in pipes can be carried out by considering different modes of GWs.

Finally, the 3D FE model with the fatigue crack could be further improved by taking the plasticity-driven nonlinearity into the consideration. There are always some plastic zones around the tips of a fatigue crack due to a high stress concentration, the presence of these plastic zones may contribute to the generation of second harmonic of GW. This effect would be of a great interest for further investigations.